UNIVERSIDAD DE CHILE
FACULTAD DE CIENCIAS FÍSICAS Y MATEMÁTICAS
DEPARTAMENTO DE FÍSICA

TOPICS IN TWO-DIMENSIONAL FERROMAGNETISM

TESIS PARA OPTAR AL GRADO DE MAGÍSTER EN CIENCIAS, MENCIÓN FÍSICA.

RODRIGO ANDRÉS JAESCHKE UBIERGO

PROFESOR GUÍA:
ÁLVARO SEBASTIÁN NÚÑEZ VÁSQUEZ

MIEMBROS DE LA COMISIÓN:
LUIS E. F. FOÀ TORRES
RODRIGO ENRIQUE ARIAS FEDERICI
SEBASTIÁN EDUARDO ALLENDE PRIETO

SANTIAGO, CHILE
2020

TOPICS IN TWO-DIMENSIONAL FERROMAGNETISM

English

This thesis consists of two parts. In part I, we model the magnetic degrees of freedom in the van der Waals magnet CrI_3. We start from an ab-initio Hamiltonian obtained with LDA calculations. Employing a self-consistent method, we include the local electronic repulsion as a mean-field theory of the Kanamori Hamiltonian on Cr^{+3} ions. Using a Green's functions method, we use the electronic Hamiltonian to calculate the corresponding spin Hamiltonian and the magnonic spectrum. A Heisenberg-Kitaev-Γ model is found to describe the ferromagnetism adequately in CrI_3. Also, we found a nontrivial topological structure in the spin excitations.

Part II includes two projects carried out in the context of micromagnetic simulations. The first one studies the stability of an antiferromagnetic skyrmion in the top layer of a bilayer system. In the second project, we study the equilibrium and dynamics of a ferromagnetic domain wall on the surface of a nanotube. We show that the domain wall's velocity is increased in the presence of a Dzyaloshinskii-Moriya interaction.

Español

Esta tesis consiste de dos partes. En la parte I, se modelan los grados de libertad magnéticos en el imán bidimensional de van der Waals CrI_3. Se comienza desde un cálculo ab initio obtenido, mediante la aproximación de densidad local (LDA). Empleando un método autoconsistente, se incluye la repulsión electrónica local a través de una teoría de campo medio del Hamiltoniano de Kanamori, en los iones Cr^{+3}. Utilizando un método de funciones de Green, se deduce un Hamiltoniano de spin, a partir del modelo electrónico, y se calcula el correspondiente espectro de magnones en torno al estado basal. Se encontró que un modelo de Heisenberg-Kitaev describe de forma aproximada el ferromagnetismo en CrI_3. Además, se observó una estructura topológica no trivial en las excitaciones magnéticas.

La parte II incluye dos proyectos desarrollados en el contexto de simulaciones micromagnéticas. En el primero de estos, se estudió la estabilidad de un Skyrmion antiferromagnético en la capa superior de una bicapa antiferromagnética. En el segundo proyecto, se investigó el equilibrio y la dinámica de una pared de dominio magnética en un nanotubo. Al respecto, se mostró que la velocidad máxima de la pared de dominio puede aumentar en presencia de una interacción de Dzyaloshinskii-Moriya.

A mi madre, Francisca Ubiergo,
por su incondicional apoyo durante todo el proceso.

Acknowledgements

Agradecimientos

Esta tesis fue escrita en inglés, porque me parecía que de esta manera su contenido llegaría a más personas dentro del mundo académico. Sin embargo, decidí escribir esta sección en mi idioma, el español, para que llegue de forma más personal a aquellas personas a las que va dirigida. Estas paginas incluyen todos los proyectos de investigación en los que he estado involucrado hasta la fecha, desde incluso antes de empezar mi magister, como es el caso del proyecto de Skyrmions antiferromagneticos, del capítulo 4, que fue llevado a cabo durante mi pregrado. Este escrito engloba parte importante de mi formación académica, pero tambien de mi formación personal. Si bien disfruté enormemente el transcurso de mi investigación, hubo muchos momentos de frustración, en los que no habría podido seguir adelante, si no fuera por el gigantesco apoyo que tuve a mis espaldas.

Comenzaré agradeciendo a mi madre, Francisca, porque ha sido un pilar de apoyo emocional incondicional durante todo este proceso. Al respecto, quisiera compartir una anécdota. En enero de 2018, cuando el proyecto de Skyrmions antiferromagnéticos estaba casi concluido, yo me fui de vacaciones por un mes, y dejé en mi casa corriendo un programa que demoraría aproximadamente ese mismo tiempo (en ese entonces, mi código estaba muy pobremente optimizado), con la esperanza de volver y tener los gráficos listos para publicar el trabajo. Cuando llevaba 4 días de vacaciones, me di cuenta que se había desconectado mi laptop, el código había parado, y yo no había configurado ninguna vía de acceso remoto, para arreglarlo durante mi viaje (gran lección aprendí ese día). Mi madre, desde siempre muy involucrada en todo lo que yo hacía, fue capaz de poner a correr diez códigos en linux, sin jamás haber visto una terminal en su vida. Todo mediante instrucciones por whatsapp y screenshots. Estuvo cerca de 4 horas, pacientemente apretando las teclas que yo le indicaba, y todos los códigos volvieron a ejecutarse. Cuando volví de mis vacaciones, estaba todo listo para ser publicado. Este es solo un ejemplo, entre muchos otros, que demuestran lo infinitamente involucrada que estuvo en todo lo que yo hacía. Me animó cuando nada funcionaba, y celebró conmigo cuando conseguía solucionar un problema. Es por esto que no puedo dedicar este trabajo a otra persona que no sea a ti, "Paqui". Muchas gracias por todo.

El apoyo e interés de mi hermano, Gerardo Jaeschke Ubiergo, y de mi padre, Gerardo Jaeschke Silva, siempre estuvieron presentes. Elegí una carrera poco convencional, cuya estabilidad laboral puede ser puesta en duda con enorme facilidad, pero siempre sentí que ellos me apoyaron, y se interesaron por lo que amaba hacer. Me pasé muchas onces familiares hablándoles de física, y tratando de aterrizar un poco las aplicaciones de mi trabajo. Ellos, siendo ajenos a mi área, siempre se mostraron muy entusiasmados por mis proyectos. Lo

Figure 1: An accurate description of my last weeks.

Table of Contents

Index of illustrations

Introduction

This thesis goes through different topics in bi-dimensional magnetism. Magnetism has had a leading role in the history of physics and science. From ancient Greece, passing by the classical electrodynamics to the quantum mechanics revolution and the solid-state physics [83], magnetism has accompanied various revolutions of science. Magnetic phenomena have enormous potential from a theoretical point of view. But also, several magnetic behaviors serve as inspiration for new technologies. The topic of this thesis tries to position magnetism in one of the last solid-state physics revolutions: The bidimensional materials.

At the beginning of the XXI century, the solid-state community made enormous efforts to synthesize a bidimensional material experimentally. These efforts materialized in the discovery of graphene [70], a bi-dimensional arrangement of Carbon atoms forming a honeycomb lattice, which have semi-metallic properties that opened new and exciting lines of research, with several applications in the design of electronic devices. More than a decade has passed from graphene's discovery, and nowadays, we know that graphene was just the first of a giant family of bidimensional materials whose chemical, electrical, and optical properties have aroused to great interest inside the scientific community [71, 75, 2, 22].

Recently, magnetism has entered the scene, due to the discovery of bidimensional materials that behave as ferromagnets. Despite the efforts, for a long time, no 2D material was found that have intrinsic magnetic properties. Even, according to the Mermin-Wagner theorem, any 2D magnet, with full rotational symmetry, is unstable due to thermal fluctuations at all temperatures distinct to zero. In 2017, it was reported the discovery of a single-layer CrI_3 [39]. This material is a semiconductor, and a layered-crystal and its 2D layers interact between them by van der Waals forces, such as graphene. Magnetic properties of CrI_3 even persist in the single-layer structure.

In this material, Cr^{+3} ions form a honeycomb lattice of magnets that interact through super exchanges paths between I^- anions. It has been observed that magnetic degrees of freedom in single layer CrI_3 are decoupled of the substrate, as opposed to metallic ferromagnets, in which the substrate is coupled with the magnetic freedom degrees. Two layers of CrI_3 are coupled antiferromagnetically, and three-layer system couple ferromagnetically. All these features serve as motivation to study the origin of ferromagnetism in the single-layer CrI_3. In particular, it is crucial to explain the microscopical origin of the lack of full rotational symmetry in the spin freedom degrees, which leads to a stable ferromagnetic state at finite temperature. This text is divided into two parts. Part I is focused on the understanding of ferromagnetism in the van der Waals magnet CrI_3. Chapter 1 introduces the single-band Hubbard model, which is the natural way to incorporate the local electronic repulsion to any tight-binding model. Then we show its multi-orbital version in the context of transition metals, such as Cr^{+3}. A Hartree-Fock approximation is used to treat the electronic interactions with a mean-field technique. This formalism is then applied to an effective tight-binding model of CrI_3. A metal-Mott-insulator transition is observed when electronic repulsion is increased from zero. We obtain an effective mean-field Hamiltonian of the single-layer CrI_3 ferromagnet.

In chapter 2, we focus on the understanding of the magnetic degrees of freedom of the

material. To do this task, we introduce a generalization of the Green's functions method used in [62], to calculate several magnetic couplings. We incorporate second-order terms in the spin-orbit coupling perturbation, which has been neglected in previous works. From these high order terms, we were able to calculate a spin Hamiltonian, which has the symmetries of a Heisenberg-Kitaev model, plus a contribution of single-ion anisotropy. The spectrum of magnons and all magnetic couplings were calculated as functions of the spin-orbit magnitude. In chapter 3, we assume a simplified version of the Hamiltonian obtained in chapter 2, and we calculate the corresponding magnon's spectrum analytically. Also, we observe that the presence of the Kitaev's term leads to a nontrivial topological structure in the spin excitations.

Part II of this thesis was developed chronologically before that the rest of the text, and it includes two projects carried out in the context of micromagnetic simulations of magnetic textures with Dzyaloshinskii-Moriya interaction. The idea is to numerically solve the Landau–Lifshitz–Gilbert equation to study the temporal evolution of magnetic moments in different geometries.

In chapter 4, we study an antiferromagnetic bilayer system, which supports an atomic-sized skyrmion on the top layer. Skyrmions are pseudo-particle textures of the magnetization field, which posses a nontrivial winding number. Due to their robustness, skyrmions have been proposed as potential information carriers in magnetic racetracks. They can move fast when spin-polarized currents are applied. Furthermore, antiferromagnetic skyrmions (AFM-Sk) also have two advantages over their ferromagnetic counterparts (FM-Sk): (i) AFM-Sk are even faster than FM-Sk. (ii) AFM-Sk moves straightly when spin-polarized currents are applied. We construct a stability diagram showing a vast region in which an AFM-Sk on the top layer is meta-stable. We also characterize the energy barrier that protects the skyrmion of collapsing to the AFM Neel-like state.

In Chapter 5, we study a ferromagnetic domain wall on the surface of a nanotube. We show that by including DMI in the energy functional, the domain wall equilibrium changes, and the system prefers a specific chirality. Also, DMI modifies the dynamics of the domain wall in the presence of an external magnetic field. It has been previously reported that there are two regimes in the DW motion: (i) For low magnetic field, the domain wall reaches a stationary motion, with constant velocity. (ii) For magnetic fields bigger than a critical field, the motion is precessional, and the average velocity decreases when higher fields are applied. We show that, by including DMI, the critical field is increased, and the domain wall can reach greater velocities.

The variety of studies present in this thesis cover a broad range of topics inside bidimensional magnetism. The author's idea was to understand the microscopical origin of magnetic order in the matter. This is the goal of chapters 1 and 2. Once the origin of the magnetic order is clear, and a magnetic ground state is known, it is possible to study the spin wave's spectrum (chapter 3), and also the behavior of a magnetic texture, such as a domain wall, or a skyrmion (chapters 4 and 5).

The van der Waals magnet CrI_3 was a perfect platform to learn about 2D magnetic phenomena and is the central object of study in part I. However, we did not explore magnetic textures in CrI_3, and this is proposed as possible future research. If inversion symmetry is

broken by means of, for example, an electrical field perpendicular to the plane of the sample, a DMI interaction could appears on the spin Hamiltonian. This feature could enable skyrmions to be stable at CrI_3 [55, 56].

This thesis was written in the LaTeX template of Pablo Pizarro [76].

Part I

The origin of ferromagnetism in the van der Waals magnet CrI₃

Chapter 1

Hartree Fock mean field approximation in a multi-orbital Hubbard Model

1.1. Single-band Hubbard Model

In solid-state systems, the repulsion between electrons, and correlation effects are usually incorporated by mean of the Hubbard Hamiltonian:

$$H = H_{TB} + U \sum_i \hat{n}_{i\uparrow} \hat{n}_{i\downarrow} \, , \tag{1.1}$$

where U is called the Hubbard parameter, and $\hat{n}_{i\sigma}$ is the number operator of electrons with spin σ at the site i. H_{TB} is the kinetic term of the Hamiltonian an its spectrum gives origin to the band structure when the electronic repulsion is ignored.

One way to obtain the approximated spectrum of this Hamiltonian is to make use of the mean field approximation, by writing $\hat{n}_{i\sigma} = \langle \hat{n}_{i\sigma} \rangle + \delta \hat{n}_{i\sigma}$, and replacing it in the second term of Hamiltonian (1.1):

$$\begin{aligned} \hat{n}_{i\uparrow} \hat{n}_{i\downarrow} &= (\langle \hat{n}_{i\uparrow} \rangle + \delta \hat{n}_{i\uparrow})(\langle \hat{n}_{i\downarrow} \rangle + \delta \hat{n}_{i\downarrow}) \\ &= \delta \hat{n}_{i\uparrow} \langle \hat{n}_{i\downarrow} \rangle + \delta \hat{n}_{i\downarrow} \langle \hat{n}_{i\uparrow} \rangle + \langle \hat{n}_{i\uparrow} \rangle \langle \hat{n}_{i\downarrow} \rangle + \delta \hat{n}_{i\uparrow} \delta \hat{n}_{i\downarrow} \, . \end{aligned} \tag{1.2}$$

The central idea of mean field approximation is to neglect the high order fluctuations $\delta \hat{n}_{i\uparrow} \delta \hat{n}_{i\downarrow}$. Replacing $\delta \hat{n}_{i\sigma} = \hat{n}_{i\sigma} - \langle \hat{n}_{i\sigma} \rangle$ in equation (1.2) we obtain.

$$\begin{aligned} \hat{n}_{i\uparrow} \hat{n}_{i\downarrow} &\approx (\hat{n}_{i\uparrow} - \langle \hat{n}_{i\uparrow} \rangle) \langle \hat{n}_{i\downarrow} \rangle + (\hat{n}_{i\downarrow} - \langle \hat{n}_{i\downarrow} \rangle) \langle \hat{n}_{i\uparrow} \rangle + \langle \hat{n}_{i\uparrow} \rangle \langle \hat{n}_{i\downarrow} \rangle \\ &= \hat{n}_{i\uparrow} \langle \hat{n}_{i\downarrow} \rangle + \hat{n}_{i\downarrow} \langle \hat{n}_{i\uparrow} \rangle + \langle \hat{n}_{i\uparrow} \rangle \langle \hat{n}_{i\downarrow} \rangle \, . \end{aligned} \tag{1.3}$$

Finally, the mean field Hamiltonian for the single-band hubbard model is:

$$H = H_{TB} + U \sum_i (\hat{n}_{i\uparrow} \langle \hat{n}_{i\downarrow} \rangle + \hat{n}_{i\downarrow} \langle \hat{n}_{i\uparrow} \rangle + \langle \hat{n}_{i\uparrow} \rangle \langle \hat{n}_{i\downarrow} \rangle) \, . \tag{1.4}$$

Mean occupations can be obtained self-consistently, as we will explain in detail in later sections. Starting with an initial ansatz for the occupations $\langle n \rangle_{i\sigma}$, we calculate the band

structure of (1.4), and from this band structure, new average occupations are obtained. This iteration is repeated until the average occupations converge to some value.

1.1.1. Example: one-dimensional chain

As an example, lets considerate an infinite uni-dimensional chain, with site energy ϵ_0 and hopping parameter t:

$$H_{TB} = \sum_{i,\sigma} \epsilon_0 \hat{n}_{i\sigma} - t\hat{c}_{i,\sigma}^\dagger \hat{c}_{i+1,\sigma} + h.c. \ , \tag{1.5}$$

where $\hat{c}_{i,\sigma}^\dagger$, and $\hat{c}_{i,\sigma}$ are the creation and anihilation operators repectively, of an electron located at site i with spin σ. Hamiltonian H_{TB} can be easily diagonalized by introducing Bloch sums of the form

$$\hat{c}_{j,\sigma}^\dagger = \frac{1}{\sqrt{N}} \sum_k e^{ikx_j} \hat{c}_{k,\sigma}^\dagger \ , $$
$$\hat{c}_{j,\sigma} = \frac{1}{\sqrt{N}} \sum_k e^{-ikx_j} \hat{c}_{k,\sigma} \ , \tag{1.6}$$

where N is the number of sites, $x_j = aj$, and k takes values in the first Brillouin zone. After replacement of the Bloch's sums into Hamiltonian (1.5) we get

$$\hat{H}_{TB} = \frac{1}{N} \sum_\sigma \sum_j \sum_{k,k'} e^{iaj(k-k')} \left(\epsilon_0 \hat{c}_{k\sigma}^\dagger \hat{c}_{k'\sigma} - te^{iak} \hat{c}_{k\sigma}^\dagger \hat{c}_{k'\sigma} - te^{-iak} \hat{c}_{k'\sigma}^\dagger \hat{c}_{k\sigma} \right) \ . \tag{1.7}$$

Using the identity $\sum_j e^{iaj(k-k')} = N\delta_{kk'}$, the Hamiltonian is diagonalized:

$$\hat{H}_{TB} = \sum_\sigma \sum_k \left(\epsilon_0 - 2t \cos ak \right) \hat{c}_{k\sigma}^\dagger \hat{c}_{k\sigma} \ . \tag{1.8}$$

Eigenenergies of (1.8), $\epsilon(k) = \epsilon_0 - 2t \cos ak$ give us the band structure, and as we can see in fig 1.3, the spectrum is spin degenerated. Let's suppose that there are N electrons, so we have one electron per site, therefore half of the total states are occupied and the system is metallic.

Now, let us focus on the Hubbard term. We choose a spin polarization axis, and assume that average spin occupations on all sites is the same. After mean field approximation (1.3), Hubbard's Hamiltonian takes the form:

$$\hat{H}_{mf} = U \sum_j \left(\langle \hat{n}_\uparrow \rangle \hat{n}_{j\downarrow} + \langle \hat{n}_\downarrow \rangle \hat{n}_{j\uparrow} - \langle \hat{n}_\uparrow \rangle \langle \hat{n}_\downarrow \rangle \right) \ . \tag{1.9}$$

Note that mean occupations do not depend on site j, and therefore, these coefficients remain identical after passing to momentum space:

$$\hat{H}_{mf} = U \sum_k \left(\langle \hat{n}_\uparrow \rangle \hat{n}_{k\downarrow} + \langle \hat{n}_\downarrow \rangle \hat{n}_{k\uparrow} - \langle \hat{n}_\uparrow \rangle \langle \hat{n}_\downarrow \rangle \right)$$
$$= U \sum_k \sum_{\sigma,\sigma'} \left(\Delta \tau_{\sigma\sigma'}^z - C\delta_{\sigma\sigma'} \right) \hat{c}_{k\sigma}^\dagger \hat{c}_{k\sigma'} \ . $$

Here τ^z is the third pauli matrix. Moreover, we have defined $\Delta = \frac{1}{2}(\langle \hat{n}_\uparrow \rangle - \langle \hat{n}_\downarrow \rangle)$, and

$C = \frac{1}{2}(\langle \hat{n}_\uparrow \rangle + \langle \hat{n}_\downarrow \rangle) + \langle \hat{n}_\uparrow \rangle \langle \hat{n}_\downarrow \rangle$. From last expression it can be seen that the Hubbard model in mean field approximation is analogous to an effective magnetic field, constant on each site. The strenght of this magnetic field is proportional to the Hubbard parameter U, and also it is proportional to the local spin density Δ. The effect of such a spin asymmetry on the band structure is in next panel.
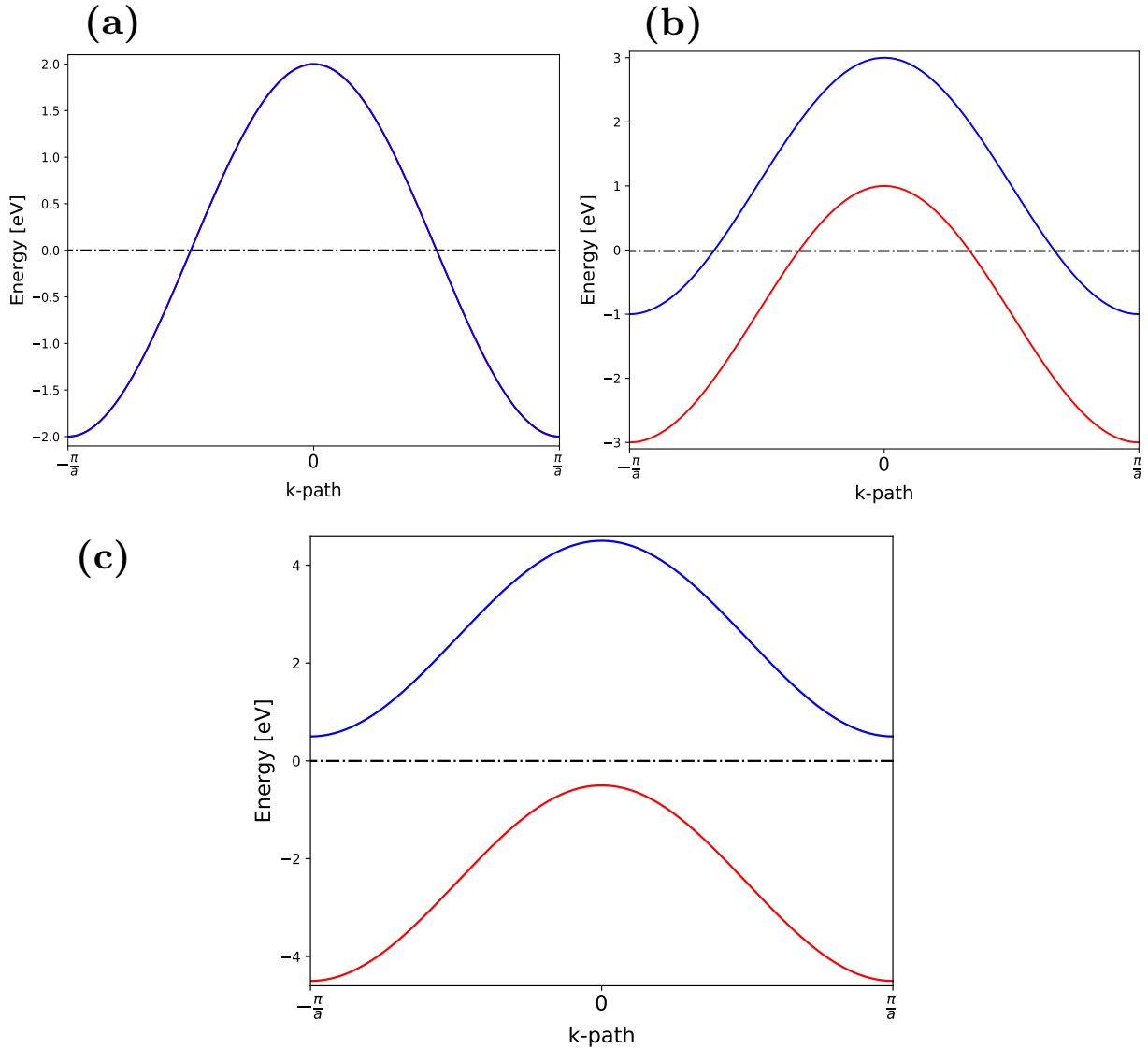
Figure 1.1: Bands of the 1D chain for different values of the Δ: (a)$\Delta = 0$; (b) $\Delta = 1eV$; (c) $\Delta = 2.5eV$. In all cases we have used $\epsilon_0 = 0$ and $y = -1eV$.

As $U\Delta$ increases from zero, spin degeneracy is left out and the system can pass from a nonmagnetic metal, to a fully spin-polarized magnetic insulator. The questions of how to find Δ and how it depends on Hubbard parameter U is postponed to a later section (see sections 3 and 4), and we conclude this example for now.

1.2. Multi-orbital Hubbard model in transition metals

In real materials, electrons lie in different pseudo-atomic orbitals, with eigenfunctions that share the same symmetries of atomic orbitals (solutions of the isolated hydrogenoid atom). These pseudo-atomic orbitals can be constructed by the Löwdin projection procedure [57] to obtain an orthonormalized basis. Here we assume that these orbitals are known, and we write them as $|\phi_{i\alpha\sigma}\rangle$. Where i, α and σ are site, orbital and spin labels respectively. The most general way to express the electronic repulsion (as a two-body operator) is

$$H_{e-e} = \sum_i \sum_{b_1 b_2 b_3 b_4} U_{b_1 b_2 b_3 b_4} \sum_{\sigma,\sigma'} \hat{c}^\dagger_{i,b_1,\sigma} \hat{c}^\dagger_{i,b_2,\sigma'} \hat{c}_{i,b_3,\sigma'} \hat{c}_{i,b_4,\sigma} \ , \tag{1.10}$$

where $U_{\alpha\beta\gamma\delta}$ is the matrix element defined by:

$$U_{b_1 b_2 b_3 b_4} = \frac{1}{2} \int d\mathbf{r}_1 d\mathbf{r}_2 \phi^*_{b_1}(\mathbf{r}_1) \phi^*_{b_2}(\mathbf{r}_2) f(\mathbf{r}_1, \mathbf{r}_2) \phi_{b_3}(\mathbf{r}_2) \phi_{b_4}(\mathbf{r}_1) \ . \tag{1.11}$$

In this expression, $f(\mathbf{r}_1, \mathbf{r}_2)$ plays the role of an effective screened coulomb repulsion. The International Union of Pure and Applied Chemistry (IUPAC) [64] defines a transition metal as an element whose atom has a partially filled d sub-shell, or which can give arise to cations with an incomplete d sub-shell. Using the spherical approximation, the screened coulomb potential is assumed to be $f(\mathbf{r}_1, \mathbf{r}_2) = f(|\mathbf{r}_2 - \mathbf{r}_1|)$. and using the symmetry of d-like pseudo-orbitals, it is possible to reduce (1.10) to the Kanamori model [10]:

$$H_U = U \sum_\alpha \hat{n}_{\alpha\uparrow} \hat{n}_{\alpha\downarrow} + (U' - \frac{J_H}{2}) \sum_{\alpha<\beta} \hat{n}_\alpha \hat{n}_\beta - 2J_H \sum_{\alpha<\beta} \hat{\mathbf{S}}_\alpha \cdot \hat{\mathbf{S}}_\beta + J_H \sum_{\alpha<\beta} \left(\hat{c}^\dagger_{\alpha\uparrow} \hat{c}^\dagger_{\alpha\downarrow} \hat{c}_{\beta\downarrow} \hat{c}_{\beta\uparrow} + h.c. \right) \ . \tag{1.12}$$

We have dropped the site index i for readability, and we only focused on repulsion terms between electrons at the same site. Labels α and β runs over orbitals with same symmetry as d_{xy}, d_{yz}, d_{zx}, $d_{x^2-y^2}$ and d_{z^2}. Here $\hat{n}_\alpha = \hat{n}_{n_\alpha\uparrow} + \hat{n}_{\alpha\downarrow}$ is the total occupation in orbital α. The spin density on each orbital is defined by

$$\hat{\mathbf{S}}_\alpha = \frac{\hbar}{2} \sum_{\sigma\sigma'} \hat{c}^\dagger_{\alpha\sigma} \boldsymbol{\tau}_{\sigma\sigma'} \hat{c}_{\alpha\sigma'} \ ,$$

with $\boldsymbol{\tau}$ the vector which components are Pauli matrices. The Kanamori parameters U, U', J_H are related by $U' = U - 2J_H$. First term of (1.12) is the repulsion between two electrons in the same orbital (with opposite spin because Pauli exclusion principle). The second term of (1.12) is the repulsion between electrons on different orbitals (at the same atomic site). Third term is the Hund coupling that gives origin to the Hund rules, favoring ferromagnetic alignment inside the atom. Last term is the so called "pair-hopping".

1.3. Hartree-Fock approximation of Hubbard Model

Hartree-Fock technique is useful to approximate the ground state of a many-body operator by a single Slater determinant Ψ_0, neglecting all correlation effects. One way to approach the Hartree-Fock approximation of a Hamiltonian written as (1.10) is to use the Wick's theorem

(see appendix A) to rewrite a two-body operator as:

$$
\begin{aligned}
\hat{c}_\alpha^\dagger \hat{c}_\beta^\dagger \hat{c}_\gamma \hat{c}_\delta =&: \hat{c}_\alpha^\dagger \hat{c}_\beta^\dagger \hat{c}_\gamma \hat{c}_\delta : \\
&+ : \hat{c}_\alpha^{\dagger\cdot} \hat{c}_\beta^\dagger \hat{c}_\gamma \hat{c}_\delta : + : \hat{c}_\alpha^{\dagger\cdot} \hat{c}_\beta^\dagger \hat{c}_\gamma^{\cdot} \hat{c}_\delta : + : \hat{c}_\alpha^{\dagger\cdot} \hat{c}_\beta^\dagger \hat{c}_\gamma \hat{c}_\delta : \\
&+ : \hat{c}_\alpha^\dagger \hat{c}_\beta^{\dagger\cdot} \hat{c}_\gamma^{\cdot\cdot} \hat{c}_\delta : + : \hat{c}_\alpha^\dagger \hat{c}_\beta^\dagger \hat{c}_\gamma^{\cdot} \hat{c}_\delta : + : \hat{c}_\alpha^\dagger \hat{c}_\beta^\dagger \hat{c}_\gamma \hat{c}_\delta : \\
&+ : \hat{c}_\alpha^{\dagger\cdot} \hat{c}_\beta^{\dagger\cdot} \hat{c}_\gamma^{\cdot\cdot} \hat{c}_\delta^{\cdot\cdot} : + : \hat{c}_\alpha^{\dagger\cdot} \hat{c}_\beta^{\dagger\cdot\cdot} \hat{c}_\gamma^{\cdot} \hat{c}_\delta^{\cdot\cdot} : + : \hat{c}_\alpha^{\dagger\cdot} \hat{c}_\beta^{\dagger\cdot\cdot} \hat{c}_\gamma^{\cdot\cdot} \hat{c}_\delta^{\cdot} : \, ,
\end{aligned}
\tag{1.13}
$$

where $: \hat{A} :$ is the sequence of annihilation and creation operators $\hat{A}$ which is "normal ordered" with respect to the Fermi ground state. If we take the expectation value in the ground state over the contraction $\hat{c}_\alpha^\dagger \hat{c}_\beta^{\dagger\cdot} = \hat{c}_\alpha^\dagger \hat{c}_\beta^\dagger - : \hat{c}_\alpha^\dagger \hat{c}_\beta^\dagger :$, as $\hat{c}_\alpha^{\dagger\cdot} \hat{c}_\beta^{\dagger\cdot}$ is a number, we get $\hat{c}_\alpha^\dagger \hat{c}_\beta^\dagger = \langle \hat{c}_\alpha^\dagger \hat{c}_\beta^\dagger \rangle = 0$. In analogous way it can be seen that $\hat{c}_\gamma \hat{c}_\delta = 0$. With this in mind, we perform some permutations to get:

$$
\begin{aligned}
\hat{c}_\alpha^\dagger \hat{c}_\beta^\dagger \hat{c}_\gamma \hat{c}_\delta =&\, \langle \hat{c}_\alpha^\dagger \hat{c}_\delta \rangle \langle \hat{c}_\beta^\dagger \hat{c}_\gamma \rangle - \langle \hat{c}_\alpha^\dagger \hat{c}_\gamma \rangle \langle \hat{c}_\beta^\dagger \hat{c}_\delta \rangle \\
&+ \langle \hat{c}_\alpha^\dagger \hat{c}_\delta \rangle : \hat{c}_\beta^\dagger \hat{c}_\gamma : - \langle \hat{c}_\alpha^\dagger \hat{c}_\gamma \rangle : \hat{c}_\beta^\dagger \hat{c}_\delta : \\
&- \langle \hat{c}_\beta^\dagger \hat{c}_\delta \rangle : \hat{c}_\alpha^\dagger \hat{c}_\gamma : + \langle \hat{c}_\beta^\dagger \hat{c}_\gamma \rangle : \hat{c}_\alpha^\dagger \hat{c}_\delta : \\
&+ : \hat{c}_\alpha^\dagger \hat{c}_\beta^\dagger \hat{c}_\gamma \hat{c}_\delta : \, .
\end{aligned}
\tag{1.14}
$$

This expression allows us to separate the non-normal-ordered two-body operator as a sum of a one body contribution, and a genuine two body part (last term). The central idea in the mean-field Hartree-Fock approximation is to interpret $: \hat{c}_\alpha^\dagger \hat{c}_\beta^\dagger \hat{c}_\gamma \hat{c}_\delta :$ as a fluctuational term, and neglect it.

An equivalent way to formulate Hartree-Fock approximation is through a variational principle. A trial wave function $|\Psi_0\rangle$ is constructed to be the ground state of an *effective one body Hamiltonian H_{hf}*. The matrix elements of H_{hf} are obtained, minimizing the energy in the state $|\Psi_0\rangle$:

$$
\delta \langle \Psi_0 | H_{hf} | \Psi_0 \rangle = 0 \, .
\tag{1.15}
$$

We note that the last term of (1.14) has zero expectation value, and also has zero first variation with respect to the Hartree-Fock ground state $|\Psi_0\rangle$.

$$
\delta \langle \Psi_0 | : \hat{c}_\alpha^\dagger \hat{c}_\beta^\dagger \hat{c}_\gamma \hat{c}_\delta : | \Psi_0 \rangle = \langle \delta \Psi_0 | : \hat{c}_\alpha^\dagger \hat{c}_\beta^\dagger \hat{c}_\gamma \hat{c}_\delta : | \Psi_0 \rangle + \langle \Psi_0 | : \hat{c}_\alpha^\dagger \hat{c}_\beta^\dagger \hat{c}_\gamma \hat{c}_\delta : | \delta \Psi_0 \rangle = 0
\tag{1.16}
$$

Last expression is zero because up to first order, variation $|\delta\Psi_0\rangle$ is a state with only one electron-hole pair. This gives another perspective of why should we neglect the last term in (1.14). After the approximation, we replace back the definition of each contraction $: \hat{c}_\alpha^\dagger \hat{c}_\beta :=$ $\hat{c}_\alpha^\dagger \hat{c}_\beta - \langle \hat{c}_\alpha^\dagger \hat{c}_\beta \rangle$ in equation (1.14) and we obtain:

$$
\begin{aligned}
\hat{c}_\alpha^\dagger \hat{c}_\beta^\dagger \hat{c}_\gamma \hat{c}_\delta \approx&\, \langle \hat{c}_\alpha^\dagger \hat{c}_\delta \rangle \hat{c}_\beta^\dagger \hat{c}_\gamma + \langle \hat{c}_\beta^\dagger \hat{c}_\gamma \rangle \hat{c}_\alpha^\dagger \hat{c}_\delta - \langle \hat{c}_\beta^\dagger \hat{c}_\gamma \rangle \langle \hat{c}_\alpha^\dagger \hat{c}_\delta \rangle \\
&- \langle \hat{c}_\alpha^\dagger \hat{c}_\gamma \rangle \hat{c}_\beta^\dagger \hat{c}_\delta - \langle \hat{c}_\beta^\dagger \hat{c}_\delta \rangle \hat{c}_\alpha^\dagger \hat{c}_\gamma + \langle \hat{c}_\beta^\dagger \hat{c}_\delta \rangle \langle \hat{c}_\alpha^\dagger \hat{c}_\gamma \rangle \, .
\end{aligned}
\tag{1.17}
$$

It is usual in literature to identify first line of (1.17) (direct pairing) as the Hartree term, and second line (exchange pairing) as the Fock term. Systematic application of (1.17) over

all terms of Kanamori model (1.12) allow us to exprress a mean field Hubbard model term by term.

1.3.1. Hartree-Fock approximation on different parts of Kanamori Hamiltonian

Now, we define four different terms that contribute to Kanamori Hamiltonian (1.12):

$$
\begin{aligned}
H_1 &= U \sum_\alpha \hat{n}_{\alpha\uparrow} \hat{n}_{\alpha\downarrow} &,\\
H_2 &= (U' - \frac{J_H}{2}) \sum_{\alpha<\beta} \hat{n}_\alpha \hat{n}_\beta &,\\
H_3 &= -2J_H \sum_{\alpha<\beta} \hat{\mathbf{S}}_\alpha \cdot \hat{\mathbf{S}}_\beta &,\\
H_4 &= J_H \sum_{\alpha<\beta} \left(\hat{c}^\dagger_{\alpha\uparrow} \hat{c}^\dagger_{\alpha\downarrow} \hat{c}_{\beta\downarrow} \hat{c}_{\beta\uparrow} + h.c. \right) .
\end{aligned}
\tag{1.18}
$$

In this way, Kanamori's Hamiltonian takes the form $H_{U-J} = H_1 + H_2 + H_3 + H_4$, and we use the mean field Hartree-Fock approximation (1.17) on each term separately. In the case of H_1 equation (1.17) is applied straight forward as:

$$
\begin{aligned}
H_1 =& U \sum_\alpha \hat{n}_{\alpha\uparrow} \hat{n}_{\alpha\downarrow} \\
\approx& U \sum_\alpha (\langle \hat{n}_{\alpha\uparrow} \rangle \hat{n}_{\alpha\downarrow} + \langle \hat{n}_{\alpha\downarrow} \rangle \hat{n}_{\alpha\uparrow} - \langle \hat{n}_{\alpha\uparrow} \rangle \langle \hat{n}_{\alpha\uparrow} \rangle \\
&- \langle \hat{c}^\dagger_{\alpha\uparrow} \hat{c}_{\alpha\downarrow} \rangle \hat{c}^\dagger_{\alpha\downarrow} \hat{c}_{\alpha\uparrow} - \langle \hat{c}^\dagger_{\alpha\downarrow} \hat{c}_{\alpha\uparrow} \rangle \hat{c}^\dagger_{\alpha\uparrow} \hat{c}_{\alpha\downarrow} + \langle \hat{c}^\dagger_{\alpha\uparrow} \hat{c}_{\alpha\downarrow} \rangle \langle \hat{c}^\dagger_{\alpha\downarrow} \hat{c}_{\alpha\uparrow} \rangle) .
\end{aligned}
\tag{1.19}
$$

To deal with H_2, we start expanding the number occupations:

$$
\begin{aligned}
H_2 &= (U' - \frac{J_H}{2}) \sum_{\alpha<\beta} \hat{n}_\alpha \hat{n}_\beta \\
&= (U' - \frac{J_H}{2}) \sum_{\alpha<\beta} (\hat{n}_{\alpha\uparrow} + \hat{n}_{\alpha\downarrow})(\hat{n}_{\beta\uparrow} + \hat{n}_{\beta\downarrow}) \\
&= (U' - \frac{J_H}{2}) \sum_{\alpha<\beta} (\hat{n}_{\alpha\uparrow}\hat{n}_{\beta\uparrow} + \hat{n}_{\alpha\uparrow}\hat{n}_{\beta\downarrow} + \hat{n}_{\alpha\downarrow}\hat{n}_{\beta\uparrow} + \hat{n}_{\alpha\downarrow}\hat{n}_{\beta\downarrow}) .
\end{aligned}
\tag{1.20}
$$

Now, we approximate each term on the sum separately:

$$
\begin{aligned}
\hat{n}_{\alpha\uparrow}\hat{n}_{\beta\uparrow} \approx & \langle \hat{n}_{\alpha\uparrow} \rangle \hat{n}_{\beta\uparrow} + \langle \hat{n}_{\beta\uparrow} \rangle \hat{n}_{\alpha\uparrow} - \langle \hat{n}_{\alpha\uparrow} \rangle \langle \hat{n}_{\beta\uparrow} \rangle \\
& - \langle \hat{c}^\dagger_{\alpha\uparrow} \hat{c}_{\beta\uparrow} \rangle \hat{c}^\dagger_{\beta\uparrow} \hat{c}_{\alpha\uparrow} - \langle \hat{c}^\dagger_{\beta\uparrow} \hat{c}_{\alpha\uparrow} \rangle \hat{c}^\dagger_{\alpha\uparrow} \hat{c}_{\beta\uparrow} + \langle \hat{c}^\dagger_{\alpha\uparrow} \hat{c}_{\beta\uparrow} \rangle \langle \hat{c}^\dagger_{\beta\uparrow} \hat{c}_{\alpha\uparrow} \rangle
\end{aligned}
\tag{1.21}
$$

$$
\begin{aligned}
\hat{n}_{\alpha\uparrow}\hat{n}_{\beta\downarrow} \approx & \langle \hat{n}_{\alpha\uparrow} \rangle \hat{n}_{\beta\downarrow} + \langle \hat{n}_{\beta\downarrow} \rangle \hat{n}_{\alpha\uparrow} - \langle \hat{n}_{\alpha\uparrow} \rangle \langle \hat{n}_{\beta\downarrow} \rangle \\
& - \langle \hat{c}^\dagger_{\alpha\uparrow} \hat{c}_{\beta\downarrow} \rangle \hat{c}^\dagger_{\beta\downarrow} \hat{c}_{\alpha\uparrow} - \langle \hat{c}^\dagger_{\beta\downarrow} \hat{c}_{\alpha\uparrow} \rangle \hat{c}^\dagger_{\alpha\uparrow} \hat{c}_{\beta\downarrow} + \langle \hat{c}^\dagger_{\alpha\uparrow} \hat{c}_{\beta\downarrow} \rangle \langle \hat{c}^\dagger_{\beta\downarrow} \hat{c}_{\alpha\uparrow} \rangle
\end{aligned}
\tag{1.22}
$$

$$
\begin{aligned}
\hat{n}_{\alpha\downarrow}\hat{n}_{\beta\uparrow} \approx & \langle \hat{n}_{\alpha\downarrow} \rangle \hat{n}_{\beta\uparrow} + \langle \hat{n}_{\beta\uparrow} \rangle \hat{n}_{\alpha\downarrow} - \langle \hat{n}_{\alpha\downarrow} \rangle \langle \hat{n}_{\beta\uparrow} \rangle \\
& - \langle \hat{c}^\dagger_{\alpha\downarrow} \hat{c}_{\beta\uparrow} \rangle \hat{c}^\dagger_{\beta\uparrow} \hat{c}_{\alpha\downarrow} - \langle \hat{c}^\dagger_{\beta\uparrow} \hat{c}_{\alpha\downarrow} \rangle \hat{c}^\dagger_{\alpha\downarrow} \hat{c}_{\beta\uparrow} + \langle \hat{c}^\dagger_{\alpha\downarrow} \hat{c}_{\beta\uparrow} \rangle \langle \hat{c}^\dagger_{\beta\uparrow} \hat{c}_{\alpha\downarrow} \rangle
\end{aligned}
\tag{1.23}
$$

$$\hat{n}_{\alpha\downarrow}\hat{n}_{\beta\downarrow} \approx \langle\hat{n}_{\alpha\downarrow}\rangle\,\hat{n}_{\beta\downarrow} + \langle\hat{n}_{\beta\downarrow}\rangle\,\hat{n}_{\alpha\downarrow} - \langle\hat{n}_{\alpha\downarrow}\rangle\langle\hat{n}_{\beta\downarrow}\rangle$$
$$- \langle\hat{c}^{\dagger}_{\alpha\downarrow}\hat{c}_{\beta\downarrow}\rangle\,\hat{c}^{\dagger}_{\beta\downarrow}\hat{c}_{\alpha\downarrow} - \langle\hat{c}^{\dagger}_{\beta\downarrow}\hat{c}_{\alpha\downarrow}\rangle\,\hat{c}^{\dagger}_{\alpha\downarrow}\hat{c}_{\beta\downarrow} + \langle\hat{c}^{\dagger}_{\alpha\downarrow}\hat{c}_{\beta\downarrow}\rangle\langle\hat{c}^{\dagger}_{\beta\downarrow}\hat{c}_{\alpha\downarrow}\rangle \ . \tag{1.24}$$

Puting all together we obtain:

$$H_2 \approx (U' - \frac{J_H}{2})\times$$
$$\sum_{\alpha<\beta}\Big(\langle\hat{n}_{\alpha\uparrow}\rangle\,\hat{n}_{\beta\uparrow} + \langle\hat{n}_{\beta\uparrow}\rangle\,\hat{n}_{\alpha\uparrow} - \langle\hat{n}_{\alpha\uparrow}\rangle\langle\hat{n}_{\beta\uparrow}\rangle - \langle\hat{c}^{\dagger}_{\alpha\uparrow}\hat{c}_{\beta\uparrow}\rangle\,\hat{c}^{\dagger}_{\beta\uparrow}\hat{c}_{\alpha\uparrow} - \langle\hat{c}^{\dagger}_{\beta\uparrow}\hat{c}_{\alpha\uparrow}\rangle\,\hat{c}^{\dagger}_{\alpha\uparrow}\hat{c}_{\beta\uparrow} + \langle\hat{c}^{\dagger}_{\alpha\uparrow}\hat{c}_{\beta\uparrow}\rangle\langle\hat{c}^{\dagger}_{\beta\uparrow}\hat{c}_{\alpha\uparrow}\rangle\Big)$$
$$+ \langle\hat{n}_{\alpha\uparrow}\rangle\,\hat{n}_{\beta\downarrow} + \langle\hat{n}_{\beta\downarrow}\rangle\,\hat{n}_{\alpha\uparrow} - \langle\hat{n}_{\alpha\uparrow}\rangle\langle\hat{n}_{\beta\downarrow}\rangle - \langle\hat{c}^{\dagger}_{\alpha\uparrow}\hat{c}_{\beta\downarrow}\rangle\,\hat{c}^{\dagger}_{\beta\downarrow}\hat{c}_{\alpha\uparrow} - \langle\hat{c}^{\dagger}_{\beta\downarrow}\hat{c}_{\alpha\uparrow}\rangle\,\hat{c}^{\dagger}_{\alpha\uparrow}\hat{c}_{\beta\downarrow} + \langle\hat{c}^{\dagger}_{\alpha\uparrow}\hat{c}_{\beta\downarrow}\rangle\langle\hat{c}^{\dagger}_{\beta\downarrow}\hat{c}_{\alpha\uparrow}\rangle$$
$$+ \langle\hat{n}_{\alpha\downarrow}\rangle\,\hat{n}_{\beta\uparrow} + \langle\hat{n}_{\beta\uparrow}\rangle\,\hat{n}_{\alpha\downarrow} - \langle\hat{n}_{\alpha\downarrow}\rangle\langle\hat{n}_{\beta\uparrow}\rangle - \langle\hat{c}^{\dagger}_{\alpha\downarrow}\hat{c}_{\beta\uparrow}\rangle\,\hat{c}^{\dagger}_{\beta\uparrow}\hat{c}_{\alpha\downarrow} - \langle\hat{c}^{\dagger}_{\beta\uparrow}\hat{c}_{\alpha\downarrow}\rangle\,\hat{c}^{\dagger}_{\alpha\downarrow}\hat{c}_{\beta\uparrow} + \langle\hat{c}^{\dagger}_{\alpha\downarrow}\hat{c}_{\beta\uparrow}\rangle\langle\hat{c}^{\dagger}_{\beta\uparrow}\hat{c}_{\alpha\downarrow}\rangle$$
$$+ \langle\hat{n}_{\alpha\downarrow}\rangle\,\hat{n}_{\beta\downarrow} + \langle\hat{n}_{\beta\downarrow}\rangle\,\hat{n}_{\alpha\downarrow} - \langle\hat{n}_{\alpha\downarrow}\rangle\langle\hat{n}_{\beta\downarrow}\rangle - \langle\hat{c}^{\dagger}_{\alpha\downarrow}\hat{c}_{\beta\downarrow}\rangle\,\hat{c}^{\dagger}_{\beta\downarrow}\hat{c}_{\alpha\downarrow} - \langle\hat{c}^{\dagger}_{\beta\downarrow}\hat{c}_{\alpha\downarrow}\rangle\,\hat{c}^{\dagger}_{\alpha\downarrow}\hat{c}_{\beta\downarrow} + \langle\hat{c}^{\dagger}_{\alpha\downarrow}\hat{c}_{\beta\downarrow}\rangle\langle\hat{c}^{\dagger}_{\beta\downarrow}\hat{c}_{\alpha\downarrow}\rangle\Big) \ . \tag{1.25}$$

Now, we perform the approximation on H_3. First we expand $\hat{\mathbf{S}}_\alpha$ with respect to the fermionic operators:

$$\hat{\mathbf{S}}_\alpha = \frac{1}{2}\sum_{\sigma\sigma'}\hat{c}^{\dagger}_{\alpha\sigma}\hat{\boldsymbol{\tau}}_{\sigma\sigma'}\hat{c}_{\alpha\sigma'} = \frac{1}{2}\sum_{\sigma\sigma'}\begin{pmatrix}\hat{c}^{\dagger}_{\alpha\sigma}\hat{\tau}^x_{\sigma\sigma'}\hat{c}_{\alpha\sigma'}\\ \hat{c}^{\dagger}_{\alpha\sigma}\hat{\tau}^y_{\sigma\sigma'}\hat{c}_{\alpha\sigma'}\\ \hat{c}^{\dagger}_{\alpha\sigma}\hat{\tau}^z_{\sigma\sigma'}\hat{c}_{\alpha\sigma'}\end{pmatrix} = \frac{1}{2}\begin{pmatrix}\hat{c}^{\dagger}_{\alpha\uparrow}\hat{c}_{\alpha\downarrow} + \hat{c}^{\dagger}_{\alpha\downarrow}\hat{c}_{\alpha\uparrow}\\ -i\hat{c}^{\dagger}_{\alpha\uparrow}\hat{c}_{\alpha\downarrow} + i\hat{c}^{\dagger}_{\alpha\downarrow}\hat{c}_{\alpha\uparrow}\\ \hat{n}_{\alpha\uparrow} - \hat{n}_{\alpha\downarrow}\end{pmatrix} \ . \tag{1.26}$$

Using this expression, we calculate the terms in the expansion of $\hat{\mathbf{S}}_\alpha\cdot\hat{\mathbf{S}}_\beta$, and we perform some permutations to obtain normal ordered terms.

$$\hat{S}^x_\alpha\hat{S}^x_\beta = \frac{-1}{4}\Big(\hat{c}^{\dagger}_{\alpha\uparrow}\hat{c}^{\dagger}_{\beta\uparrow}\hat{c}_{\alpha\downarrow}\hat{c}_{\beta\downarrow} + \hat{c}^{\dagger}_{\alpha\uparrow}\hat{c}^{\dagger}_{\beta\downarrow}\hat{c}_{\alpha\downarrow}\hat{c}_{\beta\uparrow} + \hat{c}^{\dagger}_{\alpha\downarrow}\hat{c}^{\dagger}_{\beta\uparrow}\hat{c}_{\alpha\uparrow}\hat{c}_{\beta\downarrow} + \hat{c}^{\dagger}_{\alpha\downarrow}\hat{c}^{\dagger}_{\beta\downarrow}\hat{c}_{\alpha\uparrow}\hat{c}_{\beta\uparrow}\Big) \ , \tag{1.27}$$

$$\hat{S}^y_\alpha\hat{S}^y_\beta = \frac{-1}{4}\Big(\hat{c}^{\dagger}_{\alpha\uparrow}\hat{c}^{\dagger}_{\beta\uparrow}\hat{c}_{\alpha\downarrow}\hat{c}_{\beta\downarrow} + \hat{c}^{\dagger}_{\alpha\uparrow}\hat{c}^{\dagger}_{\beta\downarrow}\hat{c}_{\alpha\downarrow}\hat{c}_{\beta\uparrow} + \hat{c}^{\dagger}_{\alpha\downarrow}\hat{c}^{\dagger}_{\beta\uparrow}\hat{c}_{\alpha\uparrow}\hat{c}_{\beta\downarrow} + \hat{c}^{\dagger}_{\alpha\downarrow}\hat{c}^{\dagger}_{\beta\downarrow}\hat{c}_{\alpha\uparrow}\hat{c}_{\beta\uparrow}\Big) \ , \tag{1.28}$$

$$\hat{S}^z_\alpha\hat{S}^z_\beta = \frac{1}{4}\big(\hat{n}_{\alpha\uparrow}\hat{n}_{\beta\uparrow} - \hat{n}_{\alpha\uparrow}\hat{n}_{\beta\downarrow} - \hat{n}_{\alpha\downarrow}\hat{n}_{\beta\uparrow} + \hat{n}_{\alpha\downarrow}\hat{n}_{\beta\downarrow}\big) \ . \tag{1.29}$$

We replace equations (1.27) to (1.29) in H_3 and after some cancellations, we obtain:

$$H_3 = -2J_H\sum_{\alpha<\beta}\hat{\mathbf{S}}_\alpha\cdot\hat{\mathbf{S}}_\beta$$
$$= -\frac{J_H}{2}\sum_{\alpha<\beta}\big(\hat{n}_{\alpha\uparrow}\hat{n}_{\beta\uparrow} - \hat{n}_{\alpha\uparrow}\hat{n}_{\beta\downarrow} - \hat{n}_{\alpha\downarrow}\hat{n}_{\beta\uparrow} + \hat{n}_{\alpha\downarrow}\hat{n}_{\beta\downarrow}\big)$$
$$+ J_H\sum_{\alpha<\beta}\Big(\hat{c}^{\dagger}_{\alpha\uparrow}\hat{c}^{\dagger}_{\beta\downarrow}\hat{c}_{\alpha\downarrow}\hat{c}_{\beta\uparrow} + \hat{c}^{\dagger}_{\alpha\downarrow}\hat{c}^{\dagger}_{\beta\uparrow}\hat{c}_{\alpha\uparrow}\hat{c}_{\beta\downarrow}\Big) \ . \tag{1.30}$$

Terms of first sum can be approximated using the already calculated expressions. The re-

maining terms in the second sum are approximated as follows:

$$\hat{c}_{\alpha\uparrow}^{\dagger}\hat{c}_{\beta\downarrow}^{\dagger}\hat{c}_{\alpha\downarrow}\hat{c}_{\beta\uparrow} \approx \langle\hat{c}_{\alpha\uparrow}^{\dagger}\hat{c}_{\beta\uparrow}\rangle\,\hat{c}_{\beta\downarrow}^{\dagger}\hat{c}_{\alpha\downarrow} + \langle\hat{c}_{\beta\downarrow}^{\dagger}\hat{c}_{\alpha\downarrow}\rangle\,\hat{c}_{\alpha\uparrow}^{\dagger}\hat{c}_{\beta\uparrow} - \langle\hat{c}_{\alpha\uparrow}^{\dagger}\hat{c}_{\beta\uparrow}\rangle\,\langle\hat{c}_{\beta\downarrow}^{\dagger}\hat{c}_{\alpha\downarrow}\rangle$$
$$- \langle\hat{c}_{\alpha\uparrow}^{\dagger}\hat{c}_{\alpha\downarrow}\rangle\,\hat{c}_{\beta\downarrow}^{\dagger}\hat{c}_{\beta\uparrow} - \langle\hat{c}_{\beta\downarrow}^{\dagger}\hat{c}_{\beta\uparrow}\rangle\,\hat{c}_{\alpha\uparrow}^{\dagger}\hat{c}_{\alpha\downarrow} + \langle\hat{c}_{\alpha\uparrow}^{\dagger}\hat{c}_{\alpha\downarrow}\rangle\,\langle\hat{c}_{\beta\downarrow}^{\dagger}\hat{c}_{\beta\uparrow}\rangle \ ; \tag{1.31}$$

$$\hat{c}_{\alpha\downarrow}^{\dagger}\hat{c}_{\beta\uparrow}^{\dagger}\hat{c}_{\alpha\uparrow}\hat{c}_{\beta\downarrow} \approx \langle\hat{c}_{\alpha\downarrow}^{\dagger}\hat{c}_{\beta\downarrow}\rangle\,\hat{c}_{\beta\uparrow}^{\dagger}\hat{c}_{\alpha\uparrow} + \langle\hat{c}_{\beta\uparrow}^{\dagger}\hat{c}_{\alpha\uparrow}\rangle\,\hat{c}_{\alpha\downarrow}^{\dagger}\hat{c}_{\beta\downarrow} - \langle\hat{c}_{\alpha\downarrow}^{\dagger}\hat{c}_{\beta\downarrow}\rangle\,\langle\hat{c}_{\beta\uparrow}^{\dagger}\hat{c}_{\alpha\uparrow}\rangle$$
$$- \langle\hat{c}_{\alpha\downarrow}^{\dagger}\hat{c}_{\alpha\uparrow}\rangle\,\hat{c}_{\beta\uparrow}^{\dagger}\hat{c}_{\beta\downarrow} - \langle\hat{c}_{\beta\uparrow}^{\dagger}\hat{c}_{\beta\downarrow}\rangle\,\hat{c}_{\alpha\downarrow}^{\dagger}\hat{c}_{\alpha\uparrow} + \langle\hat{c}_{\alpha\alpha}^{\dagger}\hat{c}_{\downarrow\uparrow}\rangle\,\langle\hat{c}_{\beta\uparrow}^{\dagger}\hat{c}_{\beta\downarrow}\rangle \ . \tag{1.32}$$

Replacing on (1.30), we obtain

$$H_3 \approx -\frac{J_H}{2}\sum_{\alpha<\beta} \ (\langle\hat{n}_{\alpha\uparrow}\rangle\,\hat{n}_{\beta\uparrow} + \langle\hat{n}_{\beta\uparrow}\rangle\,\hat{n}_{\alpha\uparrow} - \langle\hat{n}_{\alpha\uparrow}\rangle\,\langle\hat{n}_{\beta\uparrow}\rangle$$

$$- \langle\hat{n}_{\alpha\uparrow}\rangle\,\hat{n}_{\beta\downarrow} - \langle\hat{n}_{\beta\downarrow}\rangle\,\hat{n}_{\alpha\uparrow} + \langle\hat{n}_{\alpha\uparrow}\rangle\,\langle\hat{n}_{\beta\downarrow}\rangle$$
$$- \langle\hat{n}_{\alpha\downarrow}\rangle\,\hat{n}_{\beta\uparrow} - \langle\hat{n}_{\beta\uparrow}\rangle\,\hat{n}_{\alpha\downarrow} + \langle\hat{n}_{\alpha\downarrow}\rangle\,\langle\hat{n}_{\beta\uparrow}\rangle$$
$$+ \langle\hat{n}_{\alpha\downarrow}\rangle\,\hat{n}_{\beta\downarrow} + \langle\hat{n}_{\beta\downarrow}\rangle\,\hat{n}_{\alpha\downarrow} - \langle\hat{n}_{\alpha\downarrow}\rangle\,\langle\hat{n}_{\beta\downarrow}\rangle$$
$$- \langle\hat{c}_{\alpha\uparrow}^{\dagger}\hat{c}_{\beta\uparrow}\rangle\,\hat{c}_{\beta\uparrow}^{\dagger}\hat{c}_{\alpha\uparrow} - \langle\hat{c}_{\beta\uparrow}^{\dagger}\hat{c}_{\alpha\uparrow}\rangle\,\hat{c}_{\alpha\uparrow}^{\dagger}\hat{c}_{\beta\uparrow} + \langle\hat{c}_{\alpha\uparrow}^{\dagger}\hat{c}_{\beta\uparrow}\rangle\,\langle\hat{c}_{\beta\uparrow}^{\dagger}\hat{c}_{\alpha\uparrow}\rangle$$
$$+ \langle\hat{c}_{\alpha\uparrow}^{\dagger}\hat{c}_{\beta\downarrow}\rangle\,\hat{c}_{\beta\downarrow}^{\dagger}\hat{c}_{\alpha\uparrow} + \langle\hat{c}_{\beta\downarrow}^{\dagger}\hat{c}_{\alpha\uparrow}\rangle\,\hat{c}_{\alpha\uparrow}^{\dagger}\hat{c}_{\beta\downarrow} - \langle\hat{c}_{\alpha\uparrow}^{\dagger}\hat{c}_{\beta\downarrow}\rangle\,\langle\hat{c}_{\beta\downarrow}^{\dagger}\hat{c}_{\alpha\uparrow}\rangle$$
$$+ \langle\hat{c}_{\alpha\downarrow}^{\dagger}\hat{c}_{\beta\uparrow}\rangle\,\hat{c}_{\beta\uparrow}^{\dagger}\hat{c}_{\alpha\downarrow} + \langle\hat{c}_{\beta\uparrow}^{\dagger}\hat{c}_{\alpha\downarrow}\rangle\,\hat{c}_{\alpha\downarrow}^{\dagger}\hat{c}_{\beta\uparrow} - \langle\hat{c}_{\alpha\downarrow}^{\dagger}\hat{c}_{\beta\uparrow}\rangle\,\langle\hat{c}_{\beta\uparrow}^{\dagger}\hat{c}_{\alpha\downarrow}\rangle$$
$$- \langle\hat{c}_{\alpha\downarrow}^{\dagger}\hat{c}_{\beta\downarrow}\rangle\,\hat{c}_{\beta\downarrow}^{\dagger}\hat{c}_{\alpha\downarrow} - \langle\hat{c}_{\beta\downarrow}^{\dagger}\hat{c}_{\alpha\downarrow}\rangle\,\hat{c}_{\alpha\downarrow}^{\dagger}\hat{c}_{\beta\downarrow} + \langle\hat{c}_{\alpha\downarrow}^{\dagger}\hat{c}_{\beta\downarrow}\rangle\,\langle\hat{c}_{\beta\downarrow}^{\dagger}\hat{c}_{\alpha\downarrow}\rangle)$$

$$+ J_H\sum_{\alpha<\beta} \ \left(\langle\hat{c}_{\alpha\uparrow}^{\dagger}\hat{c}_{\beta\uparrow}\rangle\,\hat{c}_{\beta\downarrow}^{\dagger}\hat{c}_{\alpha\downarrow} + \langle\hat{c}_{\beta\downarrow}^{\dagger}\hat{c}_{\alpha\downarrow}\rangle\,\hat{c}_{\alpha\uparrow}^{\dagger}\hat{c}_{\beta\uparrow} - \langle\hat{c}_{\alpha\uparrow}^{\dagger}\hat{c}_{\beta\uparrow}\rangle\,\langle\hat{c}_{\beta\downarrow}^{\dagger}\hat{c}_{\alpha\downarrow}\rangle\right. \tag{1.33}$$

$$- \langle\hat{c}_{\alpha\uparrow}^{\dagger}\hat{c}_{\alpha\downarrow}\rangle\,\hat{c}_{\beta\downarrow}^{\dagger}\hat{c}_{\beta\uparrow} - \langle\hat{c}_{\beta\downarrow}^{\dagger}\hat{c}_{\beta\uparrow}\rangle\,\hat{c}_{\alpha\uparrow}^{\dagger}\hat{c}_{\alpha\downarrow} + \langle\hat{c}_{\alpha\uparrow}^{\dagger}\hat{c}_{\alpha\downarrow}\rangle\,\langle\hat{c}_{\beta\downarrow}^{\dagger}\hat{c}_{\beta\uparrow}\rangle$$
$$+ \langle\hat{c}_{\alpha\downarrow}^{\dagger}\hat{c}_{\beta\downarrow}\rangle\,\hat{c}_{\beta\uparrow}^{\dagger}\hat{c}_{\alpha\uparrow} + \langle\hat{c}_{\beta\uparrow}^{\dagger}\hat{c}_{\alpha\uparrow}\rangle\,\hat{c}_{\alpha\downarrow}^{\dagger}\hat{c}_{\beta\downarrow} - \langle\hat{c}_{\alpha\downarrow}^{\dagger}\hat{c}_{\beta\downarrow}\rangle\,\langle\hat{c}_{\beta\uparrow}^{\dagger}\hat{c}_{\alpha\uparrow}\rangle$$
$$\left. - \langle\hat{c}_{\alpha\downarrow}^{\dagger}\hat{c}_{\alpha\uparrow}\rangle\,\hat{c}_{\beta\uparrow}^{\dagger}\hat{c}_{\beta\downarrow} - \langle\hat{c}_{\beta\uparrow}^{\dagger}\hat{c}_{\beta\downarrow}\rangle\,\hat{c}_{\alpha\downarrow}^{\dagger}\hat{c}_{\alpha\uparrow} + \langle\hat{c}_{\alpha\alpha}^{\dagger}\hat{c}_{\downarrow\uparrow}\rangle\,\langle\hat{c}_{\beta\uparrow}^{\dagger}\hat{c}_{\beta\downarrow}\rangle\right) \ .$$

Finally, in H_4 we have to approximate only one term, and the other is the corresponding hermitian conjugate

$$\hat{c}_{\alpha\uparrow}^{\dagger}\hat{c}_{\alpha\downarrow}^{\dagger}\hat{c}_{\beta\downarrow}\hat{c}_{\beta\uparrow} \approx \langle\hat{c}_{\alpha\uparrow}^{\dagger}\hat{c}_{\beta\uparrow}\rangle\,\hat{c}_{\alpha\downarrow}^{\dagger}\hat{c}_{\beta\downarrow} + \langle\hat{c}_{\alpha\downarrow}^{\dagger}\hat{c}_{\beta\downarrow}\rangle\,\hat{c}_{\alpha\uparrow}^{\dagger}\hat{c}_{\beta\uparrow} - \langle\hat{c}_{\alpha\uparrow}^{\dagger}\hat{c}_{\beta\uparrow}\rangle\,\langle\hat{c}_{\alpha\downarrow}^{\dagger}\hat{c}_{\beta\downarrow}\rangle$$
$$- \langle\hat{c}_{\alpha\uparrow}^{\dagger}\hat{c}_{\beta\downarrow}\rangle\,\hat{c}_{\alpha\downarrow}^{\dagger}\hat{c}_{\beta\uparrow} - \langle\hat{c}_{\alpha\downarrow}^{\dagger}\hat{c}_{\beta\uparrow}\rangle\,\hat{c}_{\alpha\uparrow}^{\dagger}\hat{c}_{\beta\downarrow} + \langle\hat{c}_{\alpha\uparrow}^{\dagger}\hat{c}_{\beta\downarrow}\rangle\,\langle\hat{c}_{\alpha\downarrow}^{\dagger}\hat{c}_{\beta\uparrow}\rangle \ . \tag{1.34}$$

And the corresponding hermitian conjugate is

$$\hat{c}_{\beta\uparrow}^{\dagger}\hat{c}_{\beta\downarrow}^{\dagger}\hat{c}_{\alpha\downarrow}\hat{c}_{\alpha\uparrow} \approx \langle\hat{c}_{\beta\uparrow}^{\dagger}\hat{c}_{\alpha\uparrow}\rangle\,\hat{c}_{\beta\downarrow}^{\dagger}\hat{c}_{\alpha\downarrow} + \langle\hat{c}_{\beta\downarrow}^{\dagger}\hat{c}_{\alpha\downarrow}\rangle\,\hat{c}_{\beta\uparrow}^{\dagger}\hat{c}_{\alpha\uparrow} - \langle\hat{c}_{\beta\uparrow}^{\dagger}\hat{c}_{\alpha\uparrow}\rangle\,\langle\hat{c}_{\beta\downarrow}^{\dagger}\hat{c}_{\alpha\downarrow}\rangle$$
$$- \langle\hat{c}_{\beta\uparrow}^{\dagger}\hat{c}_{\alpha\downarrow}\rangle\,\hat{c}_{\beta\downarrow}^{\dagger}\hat{c}_{\alpha\uparrow} - \langle\hat{c}_{\beta\downarrow}^{\dagger}\hat{c}_{\alpha\uparrow}\rangle\,\hat{c}_{\beta\uparrow}^{\dagger}\hat{c}_{\alpha\downarrow} + \langle\hat{c}_{\beta\uparrow}^{\dagger}\hat{c}_{\alpha\downarrow}\rangle\,\langle\hat{c}_{\beta\downarrow}^{\dagger}\hat{c}_{\alpha\uparrow}\rangle \ . \tag{1.35}$$

After this, H_4 takes the form:

$$\begin{aligned}
H_4 \approx J_H \sum_{\alpha<\beta} \Big(& \langle\hat{c}^\dagger_{\alpha\uparrow}\hat{c}_{\beta\uparrow}\rangle \hat{c}^\dagger_{\alpha\downarrow}\hat{c}_{\beta\downarrow} + \langle\hat{c}^\dagger_{\alpha\downarrow}\hat{c}_{\beta\downarrow}\rangle \hat{c}^\dagger_{\alpha\uparrow}\hat{c}_{\beta\uparrow} - \langle\hat{c}^\dagger_{\alpha\uparrow}\hat{c}_{\beta\uparrow}\rangle \langle\hat{c}^\dagger_{\alpha\downarrow}\hat{c}_{\beta\downarrow}\rangle \\
& - \langle\hat{c}^\dagger_{\alpha\uparrow}\hat{c}_{\beta\downarrow}\rangle \hat{c}^\dagger_{\alpha\downarrow}\hat{c}_{\beta\uparrow} - \langle\hat{c}^\dagger_{\alpha\downarrow}\hat{c}_{\beta\uparrow}\rangle \hat{c}^\dagger_{\alpha\uparrow}\hat{c}_{\beta\downarrow} + \langle\hat{c}^\dagger_{\alpha\uparrow}\hat{c}_{\beta\downarrow}\rangle \langle\hat{c}^\dagger_{\alpha\downarrow}\hat{c}_{\beta\uparrow}\rangle \\
& + \langle\hat{c}^\dagger_{\beta\uparrow}\hat{c}_{\alpha\uparrow}\rangle \hat{c}^\dagger_{\beta\downarrow}\hat{c}_{\alpha\downarrow} + \langle\hat{c}^\dagger_{\beta\downarrow}\hat{c}_{\alpha\downarrow}\rangle \hat{c}^\dagger_{\beta\uparrow}\hat{c}_{\alpha\uparrow} - \langle\hat{c}^\dagger_{\beta\uparrow}\hat{c}_{\alpha\uparrow}\rangle \langle\hat{c}^\dagger_{\beta\downarrow}\hat{c}_{\alpha\downarrow}\rangle \\
& - \langle\hat{c}^\dagger_{\beta\uparrow}\hat{c}_{\alpha\downarrow}\rangle \hat{c}^\dagger_{\beta\downarrow}\hat{c}_{\alpha\uparrow} - \langle\hat{c}^\dagger_{\beta\downarrow}\hat{c}_{\alpha\uparrow}\rangle \hat{c}^\dagger_{\beta\uparrow}\hat{c}_{\alpha\downarrow} + \langle\hat{c}^\dagger_{\beta\uparrow}\hat{c}_{\alpha\downarrow}\rangle \langle\hat{c}^\dagger_{\beta\downarrow}\hat{c}_{\alpha\uparrow}\rangle \Big) \; .
\end{aligned} \tag{1.36}$$

We have obtained an approximated one-body Hamiltonian for the Hubbard model, but its matrix elements depends on the different averages $\langle\hat{c}^\dagger_{\alpha\sigma}\hat{c}_{\beta\sigma'}\rangle$. These free parameters are usually obtained by solving the minimization problem (1.15). The way we choose here is slightly different, and consist in determining $\langle\hat{c}^\dagger_{\alpha\sigma}\hat{c}_{\beta\sigma'}\rangle$ by a self-consistent cycle. We explain this methodology in the next section.

1.4. Self-consistent method

As it was mentioned in last section, expectation values $\langle\hat{c}^\dagger_{\alpha\sigma}\hat{c}_{\beta\sigma'}\rangle$ can be determined self-consistently. On the self consistent method, each iteration can be summarized as follows:

i) We start with an input for the expectation values at iteration i. We define the array $M^{(i)}_{\alpha\sigma,\beta\sigma'} = \langle\hat{c}^\dagger_{\alpha\sigma}\hat{c}_{\beta\sigma'}\rangle^{(i)}$ containing all parameters.

ii) We calculate the band structure of the effective Hamiltonian.

iii) From this band structure, new expectation values $M^{(i)'}_{\alpha\sigma,\beta\sigma'} = \langle\hat{c}^\dagger_{\alpha\sigma}\hat{c}_{\beta\sigma'}\rangle^{(i)'}$ (note the prime to distinguish them from those in the first step) can be determined as:

$$\langle\hat{c}^\dagger_\alpha\hat{c}_\beta\rangle = \frac{1}{V_{BZ}} \int_{BZ} d^2\mathbf{k} \sum_{\mu=1}^n C^*_{\alpha\mu}(\mathbf{k})C_{\beta\mu}(\mathbf{k})n_F(\epsilon_\mu(\mathbf{k})) \; , \tag{1.37}$$

where V_{BZ} is the volume (area in this case) of the first Brillouin zone. Moreover, α and β indices runs over orbital an spin basis. $C_{\alpha\mu}$ is the α-component of the eigenvector with the eigenvalue $\epsilon_\mu(\mathbf{k})$. $n_F(\epsilon)$ is the Fermi-Dirac distribution.

iv) Compare the new expectation values, with those used in i). If both differ more than a given tolerance, repeat steps from i), using as input the expectation values obtained in iii).

In order to ensure convergence of the method, it is useful to include a "relaxation factor" α, in such a way that the input of iteration $i+1$ is related with the previous iteration by the recurrence:

$$M^{(i+1)}_{\alpha\sigma,\beta\sigma'} = \alpha M^{(i)'}_{\alpha\sigma,\beta\sigma'} + (1-\alpha)M^{(i)}_{\alpha\sigma,\beta\sigma'} \; . \tag{1.38}$$

The case $\alpha = 1$ recovers the case in which we use the calculated expectation values as the input for the next iteration. In general, it is a good practice to choose α small enough to

ensure the required convergence. In this work we used $\alpha = 0.05$, and the temperature is set to zero in (1.37).

This method has no unique solution. It is sensitive to the initial condition. In particular, the direction of the spin polarization at each atom can modify the final result. In order to find a good approximation for the ground state, it is useful to run the self-consistent method using several spin configurations (ferromagnetic, antiferromagnetic, polarized in several directions) and then compare them to choose the one with minimal energy.

1.5. Hartree-Fock approximation applied to $\mathbf{CrI_3}$ single layer.

Now we are going to apply the formalism explained in the previous sections to the van der Walls magnet CrI_3. Fig. 1.2 shows the atomic structure of the material. The oxidation state of Chromium and Iodine atoms is $+3$ and -1, respectively. Then we have the following electron configuration:

$$Cr^{+3}: \quad [Ar]3d^3 \ ,$$
$$I^{-1}: \quad [Kr]4d^{10}5s^25p^6 \ .$$

As we can see in fig. 1.2, in the unit cell is composed by 2 Cr and 6 I atoms. We are going to focus on the behavior of the outer electrons, so let us consider 5 orbitals of type $3d$ on each Chromium, and 3 orbitals of type $5p$ on each Iodine. We have a basis of $5 \times 2 + 3 \times 6 = 28$ orbitals, and if we consider spin, we finally get a basis of 56 elements in the unit cell. See the appendix B on this chapter to review the explicit form of these orbitals in real space. The system will be occupied with 42 valence electrons.

We thank professor Eric Suarez, to provide the form of H_{TB} in (1.1). Making first a DFT calculation in the software Quantum Espresso, which gives the band structure considering all electrons (not only the outer ones). Then a "Wannerization" procedure [67] allows projecting the Bloch's eigenstates in a basis of maximally localized pseudo atomic orbitals, which also have the constraint of share the same symmetries with the orbitals of Appendix B. In this calculation, we neglected the spin-orbit coupling, and also any local repulsion between electrons on the same site. The effective tight-binding Hamiltonian H_{TB} has the form:

$$H_{TB} = \begin{pmatrix} H_{TB}^0 & 0 \\ 0 & H_{TB}^0 \end{pmatrix} \ . \tag{1.39}$$

Here each diagonal block is the projection of the Hamiltonian in the spin basis $\{|\uparrow\rangle, |\downarrow\rangle\}$. Since both projections are identical, the spectrum is spin degenerated. In figure 1.3 it is shown the band structure. It is important to note that when the Fermi level is calculated assuming $N = 42$ electrons in the unit cell, the system behaves as a conductor. The literature says that single layer CrI_3 is a semiconductor [63], so H_{TB} is not enough to describe the material. Repulsion between electrons on the same site has to be included.
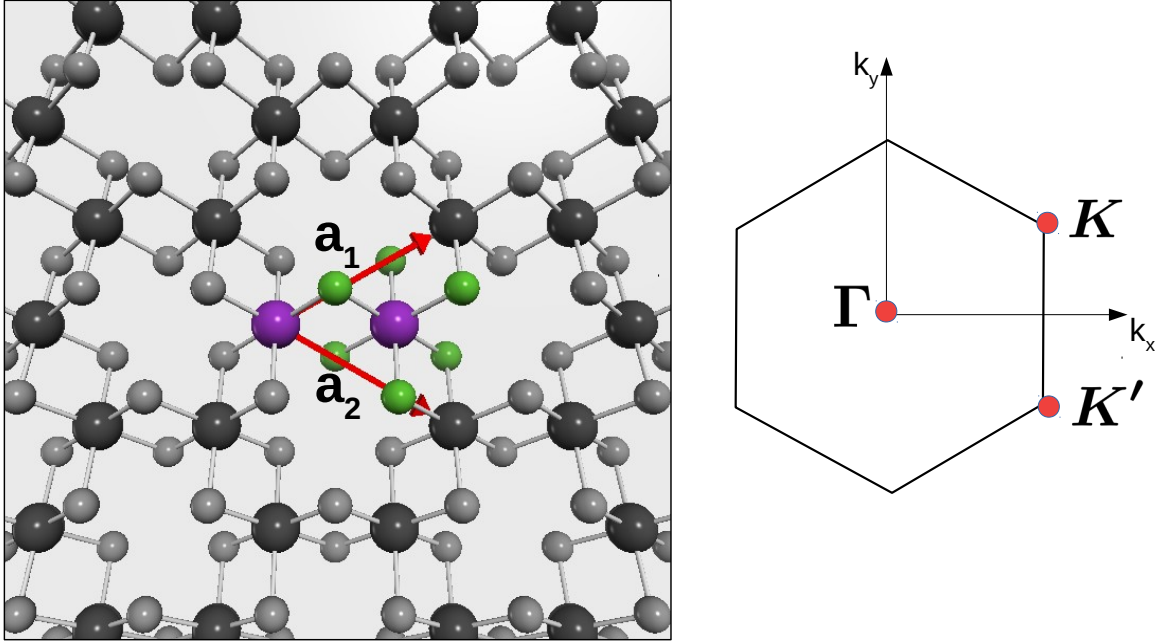
Figure 1.2: (left) Single-layer CrI_3, atoms inside the unit cell are highlighted. Purple spheres represent Cr sites, and the smaller green spheres represent the position of Iodine atoms. Lattice vectors $\mathbf{a_1} = a_0(\sqrt{3}/2, 1/2)$ and $\mathbf{a_2} = a_0(\sqrt{3}/2, -1/2)$ are drawn in red.(right) First Brillouin zone with high symmetry points
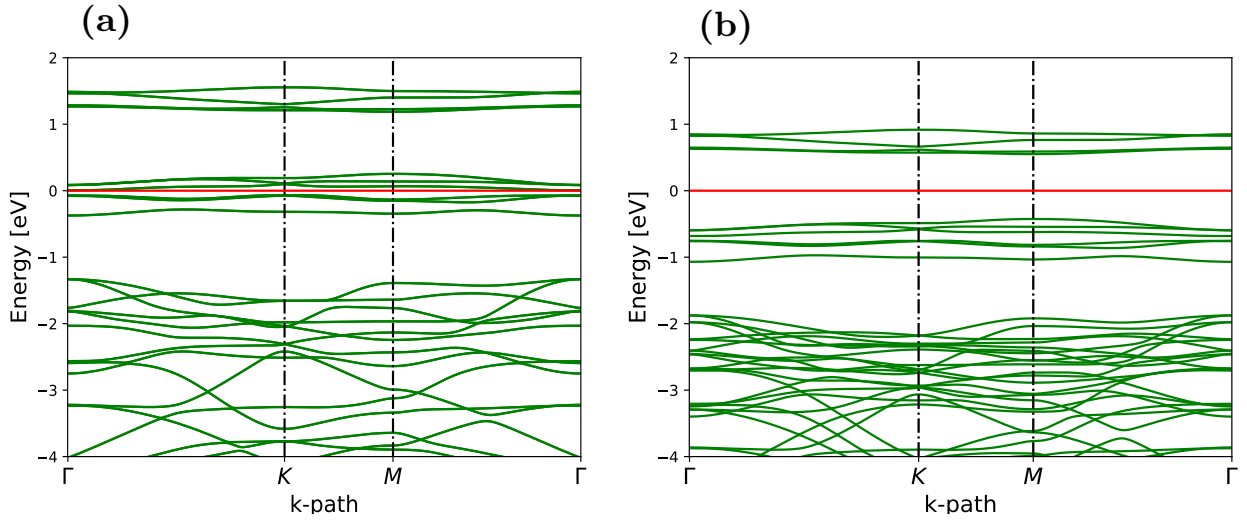
Figure 1.3: (a) Spin-degenerated spectrum of H_{TB}, obtained from LDA calculations. (b) Band structure with $U = 2.5eV$ and $J_H = 0.35U$. The chemical potential is set to zero in both cases.

The reported studies show that each Cr has a magnetic moment of $S = 3/2$, and Iodines are non-magnetic. So we are going to include the repulsion only on $d-$like orbitals of Cr sites, and Kanamori Hamiltonian of eq. (1.12), can be used without changes. The on-site

15

repulsion is parametrized with three parameters: (i) U representing the repulsion between electrons on the same orbital; (ii) U' as the repulsion between electrons on the same site but located in different orbitals; (iii) J_H representing an exchange process that flips spin between electrons of different orbitals.

As it was mentioned previously, these three parameters have the constraint $U' = U - 2J_H$. We consider the cases: (i) $J_H = 0.15U$; (i) $J_H = 0.25U$; (iii) $J_H = 0.35U$.
We calculate the mean-field Hamiltonian, with the formalism of the last section, for different values of U on each case. In figure 1.4 it is shown the magnetic moment in the unit cell when U is increased from zero. A ferromagnetic phase transition is observed for a critical value of U. In figure 1.3 we can see the resultant bands for $U = 2.5$eV and $J_H = 0.35U$. Comparing this band structure with the case $U = 0$, we see that the spin degeneracy is lifted out by the Hubbard repulsion, and the system becomes an insulator. This Metal - Mott insulator transition has been extensively studied and is useful to explain magnetic order in transition metal compounds [87, 25, 11].
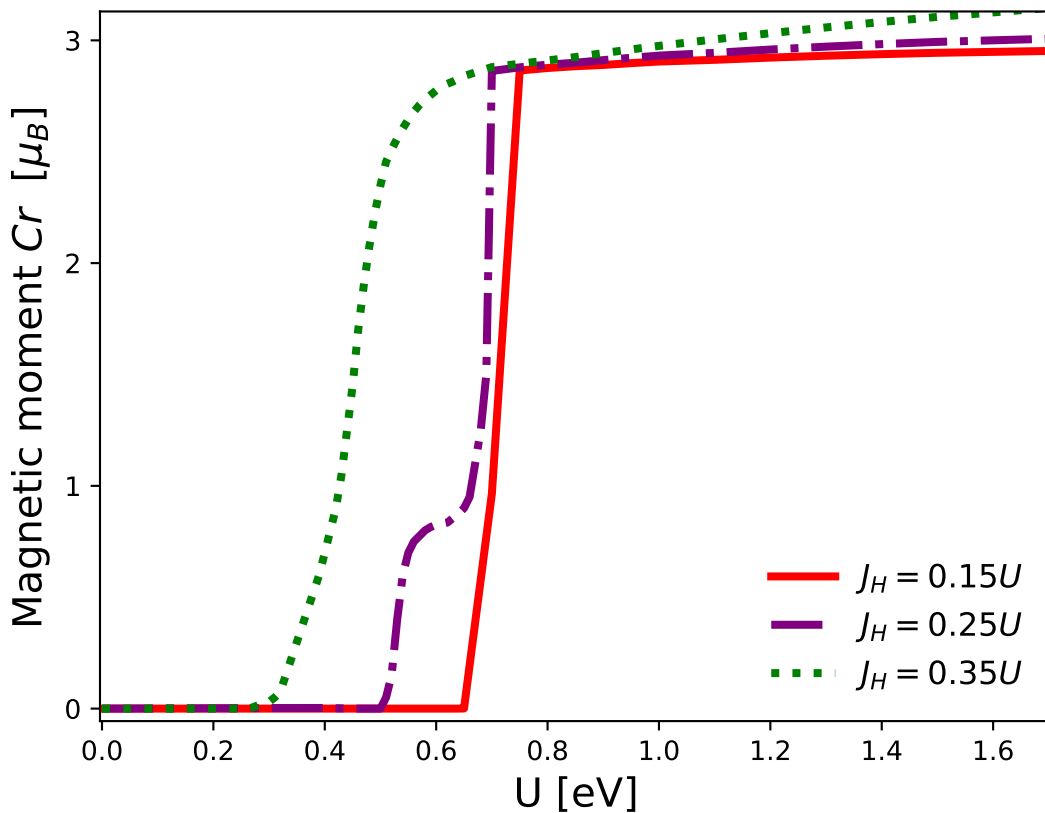
Figure 1.4: Magnetic moment on each Cr site as function of U. Three cases of J/U are shown.

Note that the transition is not as smooth as in the example of the 1D chain. This is in agreement with [58], and it is a behavior that appears when a multi-orbital model is consid-

ered. The transition is smoothed when J_H/U is increased.

The main conclusion of this chapter is that the on-site electronic repulsion cannot be neglected, because it is necessary to describe the ferromagnetism properly in the van der Waals magnet CrI_3. This local repulsion is the reason behind the ferromagnetic transition. However, it is not trivial to choose the correct values for U and J_H, and the quantitative results obtained in the following chapter will always be subject to the choice of U and J_H.

1.6. Appendixes

A. Normal order and Wick' Theorem

Let $A, B, C.., X, Y, Z$ be sequences of annihilation and creation operators of fermions. We define the normal order of $ABC...XYZ$ as:

$$: ABC...XYZ := (-1)^P BXA...CZY \ .$$

Here operators on the right side are sorted in such a way that all creation operators are on the left of annihilation operators. P is the number of permutations needed to reach the normal order. It is important to note that the expectation value of the operator in the vacuum is $\langle 0| : AB...YZ : |0\rangle = 0$, because either an annihilation operator acts on ket $|0\rangle$ or a creation operators acts on bra $\langle 0|$. Now we define the *contraction* of two fermionic operators as:

$$A^{\cdot} B^{\cdot} = AB- : AB : \ . \tag{1.40}$$

Note that the contraction of a pair of operators is just a number. If AB is normal ordered, the contraction is zero. Otherwise, if AB isn't normal ordered, BA is, and $A^{\cdot} B^{\cdot} = AB + BA = \{A, B\}$. The anti-commutator can be zero or one, and we conclude that $A^{\cdot} B^{\cdot}$ is just a number. Now we take the expectation value of (1.40) with respect to the vacuum $|0\rangle$, and because the expectation value of a normal ordered operator is zero, and the expectation value of a number is the number itself, we get:

$$A^{\cdot} B^{\cdot} = \langle 0| AB |0\rangle \ . \tag{1.41}$$

With the previous definitions in mind, consider N fermionic operators $A, B, C.., X, Y, Z$. Wick's theorem can be stated in the next identity:

$$\begin{aligned}
ABC...XYZ = &: ABC...XYZ : \\
&+ : A^{\cdot} B^{\cdot} C...XYZ : + : A^{\cdot} BC^{\cdot}...XYZ : +...+ : ABC...XY^{\cdot} Z^{\cdot} : \\
&+ : A^{\cdot} B^{\cdot} C^{\cdot\cdot}...X^{\cdot\cdot} YZ : +...+ : ABC^{\cdot}...X^{\cdot} Y^{\cdot\cdot} Z^{\cdot\cdot} : \\
&+ ... \\
&+ A^{\cdot} B^{\cdot} C^{\cdot\cdot}...X^{\cdot\cdot} Y^{\cdot\cdot\cdot} Z^{\cdot\cdot\cdot} + ... \ .
\end{aligned} \tag{1.42}$$

First line of the right side on (1.42) is the normal ordered operator, second line include all possible contractions between one pair of operators, and the rest of them are normal ordered. Third line include all possible contractions of two pairs of operators and so on until the last line, where the number of pairs of operators being contracted is the entire part of $\frac{N+1}{2}$. As it was mentioned before , the contraction of two operators is just a number. Therefore all contractions can be placed outside the normal ordered symbol : ... :. There is no need to include the normal order in the last line, because either N is even and all operators are contracted, then the expression is a number, or N is odd and only one operator is not contracted and it becomes unnecessary to include the symbol.

The strategy to compute different terms on the right side of (1.42) is perform all permutations necessary to put every pair of contracted operators next together, calculate the contraction using (1.41) and putting the expectation value out of the : ... : symbol. For example,

$$: \hat{c}_\alpha^\dagger \hat{c}_\beta^\dagger \hat{c}_\gamma \hat{c}_\delta := -\hat{c}_\alpha^\dagger \hat{c}_\gamma : \hat{c}_\beta^\dagger \hat{c}_\delta := -\langle \hat{c}_\alpha^\dagger \hat{c}_\gamma \rangle : \hat{c}_\beta^\dagger \hat{c}_\delta : \ , \tag{1.43}$$

where the minus sign comes from the permutation needed to join contracted operators.

Up to now we have been talking about normal order with respect to to the vacuum $|0\rangle$, which is the Fock state with zero occupations in all energy levels. It is also possible to define a normal ordering with respect to the N-particle state with lowest energy. Let's write this ground state as

$$|\Psi_0\rangle = \prod_{\alpha=1}^N \hat{c}_\alpha^\dagger |0\rangle \ . \tag{1.44}$$

States labeled with α are ordered from lowest to greatest energy. Now we can define a generalized annihilation operator as any operator that annihilate the Fermi sea $|\Psi_0\rangle$. Generalized annihilations operators are those which annihilate an empty state, or those which create a particle on an occupied state. So $\hat{c}_\alpha^\dagger$, with $\alpha \leq N$ is such a way that

$$\hat{c}_{\alpha \leq N}^\dagger |\Psi_0\rangle = 0 \tag{1.45}$$

is a generalized annihilation operator of $|\Psi_0\rangle$, and the same happens with

$$\hat{c}_{\alpha > N} |\Psi_0\rangle = 0 \ . \tag{1.46}$$

In analogous way, we can define generalized creation operators as the Hermitian conjugate of the generalized annihilation operators, and they annihilate the bra $\langle \Psi_0 |$.

We can define the normal order with respect to $|\Psi_0\rangle$ in the same way as (1.6), but letting generalized creation operators on the left of generalized annihilation operators. The same happens with the definition of the contraction (1.40). Finally, the property (1.41) becomes:

$$A^\cdot B^\cdot = \langle \Psi_0 | AB | \Psi_0 \rangle \ . \tag{1.47}$$

B. The explicit form of orbitals in real space

Pseudo atomic orbitals are constructed to have the same symmetries as the angular eigenfunctions of the Hydrogen atom. These angular eigenfunctions turn out to be also the basis functions of the irreducible representations of the full rotation group $SO(3)$. We define the kets $|l, m\rangle$ as the m-th basis function of the irreducible representation l. The angular dependence of these basis functions is:

$$\langle \Omega | |l, m\rangle = Y_l^m(\theta, \phi) = P_l^m(\cos \theta) e^{im\phi} \ . \tag{1.48}$$

Where $|\Omega\rangle = |\theta, \phi\rangle$, θ being the polar angle, and ϕ the azimuthal angle, with respect to some cartesian coordinate system. P_l^m is the associated Legendre polynomial of orders l and m. Orbitals p and d are plotted in fig 1.5.

For each Chromium atom, we have considered 5 orbitals with the symmetries of the spherical harmonics $Y_l^m(\theta, \phi)$, with $l = 2$, and $m = -2, -1, 0, 1, 2$. This five angular basis

functions can be linerarly combined to get a basis of real functions. Real d-like orbitals are listed below:

Name	Combination of Y_l^m	Explicit form
d_{xy}	$\frac{i}{\sqrt{2}}(Y_2^{-2} - Y_2^2)$	$\sqrt{\frac{15}{16\pi}}\sin^2\theta\sin 2\phi$
d_{xz}	$\frac{1}{\sqrt{2}}(Y_2^{-1} - Y_2^1)$	$\sqrt{\frac{15}{4\pi}}\sin\theta\cos\theta\cos\phi$
d_{yz}	$\frac{i}{\sqrt{2}}(Y_2^{-1} + Y_2^1)$	$\sqrt{\frac{15}{4\pi}}\sin\theta\cos\theta\sin\phi$
$d_{x^2-y^2}$	$\frac{1}{\sqrt{2}}(Y_2^{-2} + Y_2^2)$	$\sqrt{\frac{15}{16\pi}}\sin^2\cos 2\phi$
d_{z^2}	Y_2^0	$\sqrt{\frac{15}{16\pi}}(3\cos^2\theta - 1)$

For Iodine atoms, we considered p-like orbitals, which have the form $Y_m^l(\theta, \phi)$, with $l = 1$ and $m = -1, 0, 1$. The linear combinations of these three orbitals that allows to construct real orbitals are listed below:

Name	Combination of Y_l^m	Explicit form
p_x	$\frac{1}{\sqrt{2}}(Y_1^{-1} - Y_1^1)$	$\sqrt{\frac{3}{4\pi}}\sin\theta\cos\phi$
p_y	$\frac{i}{\sqrt{2}}(Y_1^{-1} + Y_1^1)$	$\sqrt{\frac{3}{4\pi}}\sin\theta\sin\phi$
p_z	Y_1^0	$\sqrt{\frac{3}{4\pi}}\cos\theta$
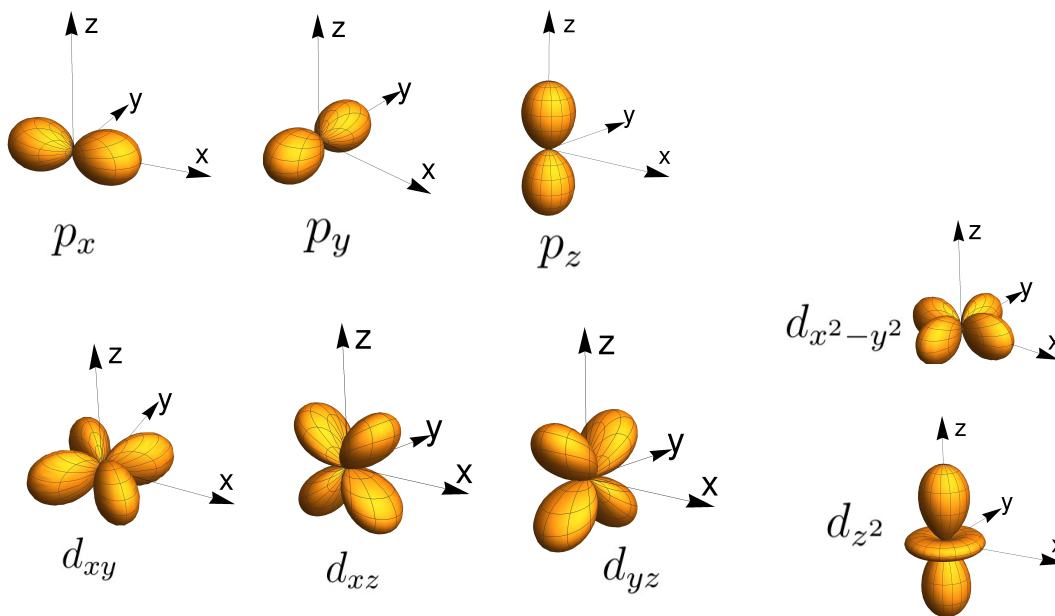
Figure 1.5: p and d orbitals used for I and Cr atoms respectively.

Chapter 2

Anisotropic ferromagnetism from Green's functions method

2.1.   What is this chapter about?

The main idea of this chapter is to calculate magnetic constants of a spin Hamiltonian, starting from the full electronic Hamiltonian of a given material. Using ab initio techniques, we calculated the band structure of a single layer CrI_3. This band structure is projected using the basis of Bloch's waves. After a *Wannerization* procedure [67], it is possible to obtain a one body effective Hamiltonian (i.e., a matrix) expressed in a basis of maximally localized pseudo-atomic orbitals. The technique developed in chapter 1 allows us to include the on-site electronic Coulomb interactions as a Hartree-Fock approximation of the Kanamori Hamiltonian (1.12).

In section 2.2, we start from a spin Hamiltonian, which includes a general exchange and magneto-crystalline anisotropy. Then, we approximate this Hamiltonian up to quadratic order in the transverse spin components. The quadratic Hamiltonian describes approximately the physics of spin excitations, which are known as magnons. The approximated spectrum of magnons is calculated in appendixes A and B, at the end of this chapter. First, we employ the Holstein Primakoff's transformation in the quadratic spin Hamiltonian. Then, we rewrite it as a bosonic Bogoliuvov-de Gennes Hamiltonian, and we use Colpa's algorithm to find the band structure.

In section 2.3, we introduce a generalization of the Green's functions method [62], by including higher-order terms in the spin-orbit coupling. This technique allows us to calculate the specific form of the quadratic Hamiltonian of section 2.2. We incorporate terms up to quadratic order in the spin-orbit coupling.

In section 2.4, we employ the Green's functions formalism to calculate the magnonic spectrum in the single-layer CrI_3, as a function of the spin-orbit coupling of Iodines. In section 2.5, we repeat the calculation by polarizing the spin in an arbitrary direction. In this way, we calculate the full spin-Hamiltonian, which describes the low energy excitations in CrI_3 ferromagnet.

2.2. Spin Hamiltonian

Previous reports show that single layer CrI_3 is ferromagnetic, with a magnetic moment of $3\mu_B$ on each Chromium atom. In a low energy regime, only the magnetic degrees of freedom of electrons become relevant. So we are interested in to map this low energy excitations into a spin Hamiltonian of the form:

$$H_S = -\frac{1}{2} \sum_{\substack{i,j \\ (i \neq j)}} \mathbf{S}_i \cdot \mathcal{J}_{ij} \cdot \mathbf{S}_j - \sum_i \mathbf{S}_i \cdot \mathcal{A}_{ii} \cdot \mathbf{S}_i \ . \tag{2.1}$$

Here, we only considered chromium sites, forming a honeycomb magnetic lattice. First summation runs over nearest neighbours, $\mathcal{J}_{ij}$ is the exchange matrix between sites i and j, with $\mathcal{J}_{ji} = \mathcal{J}_{ij}^T$. This matrix could have symmetric and antisymmetric parts, the latter indicating the lack of inversion symmetry in the crystal, and therefore the presence of a Dzyaloshinskii–Moriya exchange. The symmetric part of $\mathcal{J}_{ij}$ is not necessarily proportional to the identity. Therefore, this model also includes the possibility of anisotropic exchange. The second summation runs over all chromium sites, and matrix $\mathcal{A}_{ii}$ is a generalized anisotropy, representing an easy-plane or easy-axis anisotropy in an arbitrary direction.

Hamiltonian (2.1) is very general, in the sense that including some symmetries, we could map it into a simpler model like the XXZ or the Heisenberg-Kitaev model. Both models have been proposed recently to describe the magnetism in single layer CrI3 adequately. We aim to give some light in distinguishing which model is more appropriate. We are going to focus on the low energy excitations (i.e., spin waves) over the ground state, which is known to be a ferromagnetic configuration with magnetization pointing on $\hat{\mathbf{z}}$ (axis normal to the CrI3 layer). We perturb the ground state and rewrite magnetization as

$$\mathbf{S}_i = \begin{pmatrix} \delta S_i^x \\ \delta S_i^y \\ \sqrt{S^2 - \delta S_i^2} \end{pmatrix} \approx \begin{pmatrix} \delta S_i^x \\ \delta S_i^y \\ S - \frac{1}{2S}\delta S_i^2 \end{pmatrix}, \tag{2.2}$$

where we defined $\delta \mathbf{S}_i = (\delta S_i^x, \delta S_i^y, 0)^T$ and its squared norm as $\delta S_i^2 = (\delta S_i^x)^2 + (\delta S_i^y)^2$. Now we replace (2.2) into the exchange Hamiltonian:

$$\begin{aligned} H_{ex} &= -\frac{1}{2} \sum_{i,j} \mathbf{S}_i \cdot \mathcal{J}_{ij} \cdot \mathbf{S}_j \\ &\approx -\frac{1}{2} \sum_{i,j} ((S - \frac{\delta S_i^2}{2S})\hat{\mathbf{z}} + \delta \mathbf{S}_i) \cdot \mathcal{J}_{ij} \cdot ((S - \frac{\delta S_j^2}{2S})\hat{\mathbf{z}} + \delta \mathbf{S}_j) \\ &\approx -\frac{1}{2} \sum_{i,j} (S - \frac{\delta S_i^2}{2S})\hat{\mathbf{z}} \cdot \mathcal{J}_{ij} \cdot \hat{\mathbf{z}}(S - \frac{\delta S_j^2}{2S}) + S\left(\delta \mathbf{S}_i \cdot \mathcal{J}_{ij} \cdot \hat{\mathbf{z}} + \hat{\mathbf{z}} \cdot \mathcal{J}_{ij} \cdot \delta \mathbf{S}_j\right) + \delta \mathbf{S}_i \cdot \mathcal{J}_{ij} \cdot \delta \mathbf{S}_j \ . \end{aligned} \tag{2.3}$$

On the third line, we neglect δS_i^2 and δS_j^2 of the second sum, because they appear multiplied by a linear term in δS. Now we work each term separately, first we note that $\hat{\mathbf{z}} \cdot \mathcal{J}_{ij} \cdot \hat{\mathbf{z}} = \mathcal{J}_{ij}^{zz}$, and we expand the first term of (2.3):

$$-\frac{1}{2}\sum_{i,j}(S-\frac{\delta S_i^2}{2S})\hat{\mathbf{z}}\cdot\mathcal{J}_{ij}\cdot\hat{\mathbf{z}}(S-\frac{\delta S_j^2}{2S}) \approx -\frac{1}{2}\sum_{i,j}\left(S^2\mathcal{J}_{ij}^{zz}-\mathcal{J}_{ij}^{zz}\frac{\delta S_i^2}{2}-\mathcal{J}_{ij}^{zz}\frac{\delta S_j^2}{2}\right)$$

$$= H_{ex}^0 + \frac{1}{2}\sum_i\left(\sum_{j\neq i}\mathcal{J}_{ij}^{zz}\right)\delta S_i^2\ .$$

We have defined the exchange energy of the ground state as $H_{ex}^0 = -\frac{S^2}{2}\sum_{i,j}\mathcal{J}_{ij}^{zz}$, and the remaining terms have grouped in a nearest neighbors sum of each site. The second sum of (2.3) can be written in the same way:

$$-\frac{1}{2}\sum_{i,j}S\left(\delta\mathbf{S}_i\cdot\mathcal{J}_{ij}\cdot\hat{\mathbf{z}}+\hat{\mathbf{z}}\cdot\mathcal{J}_{ij}\cdot\delta\mathbf{S}_j\right) = -\frac{1}{2}\sum_{i,j}S\hat{\mathbf{z}}\cdot\left(\mathcal{J}_{ij}+\mathcal{J}_{ji}^T\right)\cdot\delta\mathbf{S}_i$$

$$= -\sum_i\left(\sum_{j\neq i}S\hat{\mathbf{z}}\cdot\mathcal{J}_{ij}\right)\cdot\delta\mathbf{S}_i\ .$$

Finally, the exchange Hamiltonian takes the form:

$$H_{ex} = H_{ex}^0 + \frac{1}{2}\sum_i\left(\sum_{j\neq i}\mathcal{J}_{ij}^{zz}\right)\delta S_i^2 - \sum_i\left(S\sum_{j\neq i}\hat{\mathbf{z}}\cdot\mathcal{J}_{ij}\right)\cdot\delta\mathbf{S}_i - \frac{1}{2}\sum_{i,j}\delta\mathbf{S}_i\cdot\mathcal{J}_{ij}\cdot\delta\mathbf{S}_j\ . \qquad (2.4)$$

Analogously, we can replace the perturbed magnetization in the anisotropy term:

$$\begin{aligned}H_A &= \sum_i\mathbf{S}_i\cdot\mathcal{A}_{ii}\cdot\mathbf{S}_j\\ &= H_A^0 + \sum_i\mathcal{A}_{ii}^{zz}\delta S_i^2 - 2S\sum_i\hat{\mathbf{z}}\cdot\mathcal{A}_{ii}\cdot\delta\mathbf{S}_i - \sum_i\delta\mathbf{S}_i\cdot\mathcal{A}_{ii}\cdot\delta\mathbf{S}_j\ .\end{aligned} \qquad (2.5)$$

Here, we have defined the anisotropy energy of the ground state as $H_A^0 = -S^2\sum_i\mathcal{A}_{ii}^{zz}$. Now the Hamiltonian can be written as $H_S \approx H_{ex}^0+H_A^0+\Delta H_S$, with ΔH_S being the total variation of the energy, up to second order in the perturbation.

$$\Delta H_S = -\sum_i\mathbf{h}_i\cdot\delta\mathbf{S}_i - \sum_i\delta\mathbf{S}_i\cdot\mathcal{A}'_{ii}\cdot\delta\mathbf{S}_i - \frac{1}{2}\sum_{i,j}\delta\mathbf{S}_i\cdot\mathcal{J}_{ij}\cdot\delta\mathbf{S}_j\ , \qquad (2.6)$$

where $\mathbf{h}_i$ and $\mathcal{A}'_{ii}$ are respectively an effective field and an effective anisotropy defined as:

$$\mathbf{h}_i = 2S\hat{\mathbf{z}}\cdot\mathcal{A}_{ii} + \sum_{j\neq i}S\hat{\mathbf{z}}\cdot\mathcal{J}_{ij}\ , \qquad (2.7)$$

$$\mathcal{A}'_{ii} = \mathcal{A}_{ii} - \left(\mathcal{A}_{ii}^{zz}+\frac{1}{2}\sum_{j\neq i}\mathcal{J}_{ij}^{zz}\right)1_{2\times 2}\ . \qquad (2.8)$$

Note that in the variation (2.6), $\delta\mathbf{S}_i$ is defined as a bidimensional vector. Therefore in the third summation only participates the components $\mathcal{J}_{ij}^{xx}$, $\mathcal{J}_{ij}^{yy}$, $\mathcal{J}_{ij}^{xy}$ and $\mathcal{J}_{ij}^{yx}$. The same happens with the effective field in (2.7). We simply ignore the third component and define

$\mathbf{h}_i = (h_i^x, h_i^y)$. Also, in (2.8) we used only the x and y components of $\mathcal{A}_{ii}$. The eigenstates of this Hamiltonian are particle-like excitations of the magnetization field, wich are called magnons. The magnonic spectrum can be calculated performing a Holstein Primakoff's transformation, which allows to rewrite (2.6) as a bosonic Bogoliuvov de-Gennes (BdG) Hamiltonian. The procedure to obtain the BdG Hamiltonian, and the the corresponding eigenvalues, is described in appendixes A and B of this chapter. In the next section we will focus on how to obtain a quadratic Hamiltonian like (2.6), from an electronic Hamiltonian.

2.3. Green's functions method

The goal of this section is to find a variation of an effective tight-binding Hamiltonian when we rotate the magnetization. We do this in order to map this variation to the spin Hamiltonian of (2.6). To achieve this, we use the Andersen's local force theorem [82], which states that the total energy variation δE under small perturbation from the ground state coincides with the sum of the one-particle energy changes for the occupied states at the fixed ground state potential [62]. By using the local force theorem, the first-order perturbation of the charge and spin densities takes the form:

$$\delta E = \int_{-\infty}^{E_F} d\epsilon \, \epsilon \, \delta n(\epsilon) = E_F \delta z - \int_{-\infty}^{E_F} d\epsilon \, \delta N(\epsilon) = - \int_{-\infty}^{E_F} d\epsilon \, \delta N(\epsilon) \ . \tag{2.9}$$

Here we have $n(\epsilon) = dN/d\epsilon$ as the density of electrons states (DOS). $N(\epsilon)$ is the integrated DOS, and E_F is the Fermi energy. The perturbation consists of a rotation of the magnetization, so the electron's number does not change and $\delta z = 0$. The density of states can be expressed using the Green's function as:

$$n(\epsilon) = -\frac{1}{\pi} Im Tr \left(G^+(\epsilon) \right) \ . \tag{2.10}$$

The Green's function is defined using the Hamiltonian H as $G^+(\epsilon) = (\epsilon + i0^+ - H)^{-1}$. From now on, we omit the $+$ superscript. It is understood that we need to include the $+i0^+$, in order to avoid the poles. With this, the integrated DOS takes the form:

$$\begin{aligned} N(\epsilon) &= -\frac{1}{\pi} Im \int_{-\infty}^{\epsilon} d\epsilon' Tr \left(\epsilon' - H \right)^{-1} \\ &= -\frac{1}{\pi} Im Tr \left(\ln(\epsilon - H) \right) + C \ . \end{aligned} \tag{2.11}$$

Now we write the Hamiltonian as $H = H_0 + \delta H + \delta^2 H$, separating explicitly the first and second order corrections. With this we can calculate $\delta N(\epsilon)$.

$$N(\epsilon) = -\frac{1}{\pi} ImTr\left(ln(\epsilon - H_0 - \delta H - \delta^2 H)\right)$$

$$= -\frac{1}{\pi} Im \sum_n \ln\left(\epsilon - \epsilon_n^0 - \delta\epsilon_n - \delta^2\epsilon_n\right)$$

$$= -\frac{1}{\pi} Im \left(Tr\ln(\epsilon - H_0) - \sum_n \ln\left(1 - \frac{\delta\epsilon_n + \delta^2\epsilon_n}{\epsilon - \epsilon_n^0}\right)\right) \tag{2.12}$$

$$\approx -\frac{1}{\pi} Im \left(Tr\ln(\epsilon - H_0) - \sum_n \frac{\delta\epsilon_n}{\epsilon - \epsilon_n^0} + \frac{\delta^2\epsilon_n}{\epsilon - \epsilon_n^0} + \frac{(\delta\epsilon)^2}{(\epsilon - \epsilon_n^0)^2}\right)$$

$$= N_0(\epsilon) + \frac{1}{\pi} ImTr\left(\delta HG + \delta^2 HG + \delta HG\delta HG\right) .$$

Here $G(\epsilon) = (\epsilon - H_0)^{-1}$ is the Green's function of the unperturbed system. Finally, we replace δN in (2.9) (first and second-order variations), obtaining a closed expression for the energy change.

$$\Delta E = -\frac{1}{\pi} \int_{-\infty}^{E_F} d\epsilon Im\{Tr(\delta HG(\epsilon) + \delta^2 HG(\epsilon) + \delta HG(\epsilon)\delta HG(\epsilon))\} . \tag{2.13}$$

We have not mentioned the specific form of the perturbation yet. The idea is to rotate the magnetization a small angle $\delta\phi_i$ around the axis $\delta\vec{\phi}_i/\delta\phi_i$, on each site i. The resultant transformation is block-diagonal, with one block per pseudo-atomic orbital. On each orbital on a site i, the rotation acts as:

$$U_i = \exp\left(\frac{i}{2}\delta\vec{\phi}_i \cdot \vec{\sigma}\right) . \tag{2.14}$$

We start neglecting spin-orbit coupling and assuming a collinear magnetic configuration. The Hamiltonian can be expressed on the basis of localized pseudo-atomic orbitals, using $|i, l, m, \sigma\rangle$ as the ket representing the site i, with angular momentum quantum numbers l and m and spin quantum number σ. For simplicity, we drop the orbital indices l and m, and keep only the site and spin quantum numbers. The matrix elements of the unperturbed Hamiltonian spin-diagonal:

$$H_{ij} = \begin{pmatrix} H_{ij}^\uparrow & 0 \\ 0 & H_{ij}^\downarrow \end{pmatrix} . \tag{2.15}$$

It is useful to rewrite the matrix elements of H_{ij} using Pauli matrices

$$H_{ij} = H_{ij}^0 \hat{\sigma}_0 + \frac{\Delta_{ij}}{2}\hat{\sigma}_z , \tag{2.16}$$

with $H_{ij}^0 = (H_{ij}^\uparrow + H_{ij}^\downarrow)/2$ and $\Delta_{ij} = (H_{ij}^\uparrow - H_{ij}^\downarrow)$. We used $\hat{\sigma}_0$ to denote the identity in SU(2).

The transformed Hamiltonian is:

$$
\begin{aligned}
H'_{ii} &= U_i^\dagger H_{ii} U_i \\
&= \exp\left(-\frac{i}{2}\delta\vec{\phi}_i \cdot \vec{\sigma}\right) H_{ii} \exp\left(\frac{i}{2}\delta\vec{\phi}_i \cdot \vec{\sigma}\right) \\
&\approx H_{ii} + \frac{i}{2}[\delta\vec{\phi}_i \cdot \vec{\sigma}, H_{ii}] - \frac{1}{8}[\delta\vec{\phi}_i \cdot \vec{\sigma}[\delta\vec{\phi}_i \cdot \vec{\sigma}, H_{ii}]] \ .
\end{aligned}
\tag{2.17}
$$

In the last line, we used the Baker-Campbell-Hausdorff formula, keeping terms up to second order in the angles $\delta\phi_i$. Now we calculate the first-order correction of the Hamiltonian. We omit in this step the index of site i, and it should be understood that the transformation applies for each site (and orbital) separately:

$$
\begin{aligned}
\delta H &= -\frac{i}{2}[\delta\vec{\phi} \cdot \vec{\sigma}, H] \\
&= -\frac{i}{2}\left(H^0[\delta\vec{\phi} \cdot \vec{\sigma}, \sigma_0] + \frac{\Delta}{2}[\delta\vec{\phi} \cdot \vec{\sigma}, \sigma_z]\right) \\
&= -\frac{i\Delta}{4}\left(\delta\phi^x[\sigma_x, \sigma_z] + \delta\phi^y[\sigma_y, \sigma_z]\right) \\
&= -\frac{\Delta}{2}\delta\phi^x \sigma_y + \frac{\Delta}{2}\phi^y \sigma_x \ .
\end{aligned}
\tag{2.18}
$$

In the same way, we calculate the second-order variation of the Hamiltonian:

$$
\begin{aligned}
\delta^2 H &= -\frac{1}{8}[\delta\vec{\phi} \cdot \vec{\sigma}, [\delta\vec{\phi} \cdot \vec{\sigma}, H]] \\
&= -\frac{1}{8}\left(-i\Delta\delta\phi^x[\delta\vec{\phi} \cdot \vec{\sigma}, \sigma_y] + i\Delta\delta\phi^y[\delta\vec{\phi} \cdot \vec{\sigma}, \sigma_x]\right) \\
&= -\frac{\Delta}{4}|\delta\vec{\phi}|^2 \sigma_z \ .
\end{aligned}
\tag{2.19}
$$

Here we set to zero the z-component of $\delta\vec{\phi}$ because we are considering the ground state polarized in $\hat{\mathbf{z}}$ and a z-rotation does not change the energy. We want to map the energy variations to a spin Hamiltonian, so it is going to be useful to express δH, and $\delta^2 H$ in terms of S_x and S_y in such a way $\delta\mathbf{S} = (S_x, S_y)$ is the magnetization field around the ground state. For the material we are interested in, each Chromium site has a magnetic moment $S = 3/2$, so the angle $\delta\phi$ is related to $\delta\mathbf{S}$ by:

$$
\begin{aligned}
\delta\phi_x &= -S_y/S \ , \\
\delta\phi_y &= S_x/S \ .
\end{aligned}
\tag{2.20}
$$

Defining $\psi = S_x + iS_y$, variations δH and $\delta^2 H$ can be written as:

$$
\delta H_{ii} = \frac{\Delta_i}{2S}\begin{pmatrix} 0 & \psi_i^* \\ \psi_i & 0 \end{pmatrix}
\tag{2.21}
$$

and

$$
\delta^2 H = -|\psi|^2 \frac{\Delta_i}{2S^2}\sigma_z \ .
\tag{2.22}
$$

Now we take into account the spin-orbit coupling. The only difference is that in equation

(2.13), we have to replace $G \to \tilde{G}$ and to include the spin-orbit coupling as a perturbation.

$$\tilde{G} = G + GH^{SO}G + GH^{SO}GH^{SO}G \ , \tag{2.23}$$

with $H_k^{SO} = \lambda_k \mathbf{L} \cdot \mathbf{S}$. Note that H^{SO} is diagonal in the site index k, but it mixes the pseudo-atomic orbitals on each site. We are neglecting any hopping that comes from the spin-orbit coupling. Now we write the energy variation as

$$\Delta E = \delta E + \delta^2 E \ . \tag{2.24}$$

The first and second-order variations can be expressed in turn as a sum of different contributions depending on the order of spin-orbit parameter λ_k:

$$\delta E = \delta E_0 + \delta E_\lambda + \delta E_{\lambda^2} \ , \tag{2.25}$$

$$\delta^2 E = \delta^2 E_0 + \delta^2 E_\lambda + \delta^2 E_{\lambda^2} \ . \tag{2.26}$$

Each energy term takes the form:

$$\delta E_0 = \frac{-1}{\pi} \int_{-\infty}^{E_F} d\epsilon Tr\{\delta H G\} \ , \tag{2.27}$$

$$\delta E_\lambda = \frac{-1}{\pi} \int_{-\infty}^{E_F} d\epsilon Tr\{\delta H G^{(1)}\} \ , \tag{2.28}$$

$$\delta E_{\lambda^2} = \frac{-1}{\pi} \int_{-\infty}^{E_F} d\epsilon Tr\{\delta H G^{(2)}\} \ , \tag{2.29}$$

$$\delta^2 E_0 = \frac{-1}{\pi} \int_{-\infty}^{E_F} d\epsilon Tr\{\delta^2 H G + \delta H G \delta H G\} \ , \tag{2.30}$$

$$\delta^2 E_\lambda = \frac{-1}{\pi} \int_{-\infty}^{E_F} d\epsilon Tr\{\delta^2 H G^{(1)} + \delta H G \delta H G^{(1)} + \delta H G^{(1)} \delta H G\} \ , \tag{2.31}$$

$$\delta^2 E_{\lambda^2} = \frac{-1}{\pi} \int_{-\infty}^{E_F} d\epsilon Tr\{\delta^2 H G^{(2)} + \delta H G \delta H G^{(2)} + \delta H G^{(1)} \delta H G^{(1)} + \delta H G^{(2)} \delta H G\} \ . \tag{2.32}$$

Where we have defined the corrections of the Green's function of first and second order in the spin-orbit coupling as $G^{(1)} = GH^{SO}G$ and $G^{(2)} = GH^{SO}GH^{SO}G$. In order to calculate the traces in spin, it is going to be useful to define the spin components of H^{SO}:

$$H_k^{SO} = \begin{pmatrix} h_k^{\uparrow\uparrow} & h_k^{\uparrow\downarrow} \\ h_k^{\downarrow\uparrow} & h_k^{\downarrow\downarrow} \end{pmatrix} \ , \tag{2.33}$$

where each element $h_k^{\sigma\sigma'}$ is a matrix in the orbital basis at site k.

It is easy to see that $\delta E_0 = 0$ because δH and G are spin-anti-diagonal and spin-diagonal, respectively, so the product has null trace. This doesn't happen for δE_λ and δE_{λ^2}. If we use Tr_L to represent the trace in orbital basis, and then we write the summation explicitly in the site and spin indices, we get:

$$\delta E_\lambda = -\frac{1}{\pi} \sum_{ij} \sum_{\sigma,\sigma'} Im \int_{-\infty}^{E_F} d\epsilon Tr_L \left(\delta H_{ii}^\sigma G_{ij}^\sigma H_{j,\sigma\sigma'}^{SO} G_{ji}^\sigma \right)$$

$$= -\frac{1}{2\pi S} \sum_{ij} Im \int_{-\infty}^{E_F} d\epsilon Tr_L \{ \psi_i^* \Delta_i G_{ij}^\downarrow h_j^{\downarrow\uparrow} G_{ji}^\uparrow + \psi_i \Delta_i G_{ij}^\uparrow h_j^{\uparrow\downarrow} G_{ji}^\downarrow \} \ .$$

(2.34)

The integrand has the structure $\psi^* a + \psi b$ with a and b complex numbers. We use the following identity:

$$Im \left(\psi_i^* a + \psi_i b \right) = S_i^x Im(b+a) + S_i^y Re(b-a) \ .$$

(2.35)

With this δE_λ takes the form:

$$\delta E_\lambda = -\sum_i h_i^{x(1)} S_i^x + h_i^{y(1)} S_i^y$$

$$= -\sum_i \mathbf{h}_i^{(1)} \cdot \delta \mathbf{S}_i \ .$$

(2.36)

Where we have defined the components of $\mathbf{h}_i^{(1)}$ as:

$$h_i^{x(1)} = \frac{1}{2\pi S} \sum_j Im \int_{-\infty}^{E_F} d\epsilon Tr_l \{ \Delta_i (G_{ij}^\uparrow h_j^{\uparrow\downarrow} G_{ji}^\downarrow + G_{ij}^\downarrow h_j^{\downarrow\uparrow} G_{ji}^\uparrow) \} \ ,$$

$$h_i^{y(1)} = \frac{1}{2\pi S} \sum_j Re \int_{-\infty}^{E_F} d\epsilon Tr_l \{ \Delta_i (G_{ij}^\uparrow h_j^{\uparrow\downarrow} G_{ji}^\downarrow - G_{ij}^\downarrow h_j^{\downarrow\uparrow} G_{ji}^\uparrow) \} \ .$$

(2.37)

A similar procedure allows us to calculate δE_{λ^2}.

$$\delta E_{\lambda^2} = -\sum_i \mathbf{h}_i^{(2)} \cdot \delta \mathbf{S} \ ,$$

(2.38)

with

$$h_i^{x(2)} = \frac{1}{2\pi S} Im \int_{-\infty}^{E_F} d\epsilon Tr_L \{ \Delta_i (G_{ii}^{(2)\uparrow\downarrow} + G_{ii}^{(2)\downarrow\uparrow}) \} \ ,$$

$$h_i^{y(2)} = \frac{1}{2\pi S} Re \int_{-\infty}^{E_F} d\epsilon Tr_L \{ \Delta_i (G_{ii}^{(2)\uparrow\downarrow} - G_{ii}^{(2)\downarrow\uparrow}) \} \ .$$

(2.39)

Here we have not expanded the explicit form of $G^{(2)}$ in order of keep clear the notation. Now we calculate the contributions of $\delta^2 E$. The spin-orbit independent term $\delta^2 E_0$ has two parts. The first one is:

$$\frac{-1}{\pi} Im \int_{-\infty}^{E_F} d\epsilon Tr \{ \delta^2 H G \} = \frac{1}{2\pi S^2} Im \sum_i \int_{-\infty}^{E_F} d\epsilon |\psi_i|^2 Tr_L \{ \Delta_i (G_{ii}^\uparrow - G_{ii}^\downarrow) \} \ .$$

(2.40)

Because G_{ii} is diagonal in spin basis, the identity $G_{ii}^\uparrow - G_{ii}^\downarrow = (G^\uparrow \Delta G^\downarrow)_{ii} = \sum_j G_{ij}^\uparrow \Delta_j G_{ji}^\downarrow$ is satisfied. With this the previous term takes the form:

$$\frac{-1}{\pi} Im \int_{-\infty}^{E_F} d\epsilon Tr\{\delta^2 HG\} = \frac{1}{2\pi S^2} \sum_{ij} Im \int_{-\infty}^{E_F} d\epsilon |\psi_i|^2 Tr_L\{\Delta_i G_{ij}^{\uparrow} \Delta_j G_{ji}^{\downarrow}\} \ . \tag{2.41}$$

The second part of $\delta^2 E_0$ is

$$\frac{-1}{\pi} Im \int_{-\infty}^{E_F} d\epsilon Tr\{\delta HG\delta HG\} = \frac{-1}{4\pi S^2} \sum_{ij} Im \int_{-\infty}^{E_F} d\epsilon Tr_L\{\psi_i^* \psi_j \Delta_i G_{ij}^{\downarrow} \Delta_j G_{ji}^{\uparrow} + \psi_i \psi_j^* \Delta_i G_{ij}^{\uparrow} \Delta_j G_{ji}^{\downarrow}\} \ . \tag{2.42}$$

We use the following identity

$$Im\{\psi_i^* \psi_j a + \psi_i \psi_j^* b\} = \delta\mathbf{S}_i \cdot \delta\mathbf{S}_j Im\{a + b\} + (\delta\mathbf{S}_i \times \delta\mathbf{S}_j)_z Re\{a - b\} \ , \tag{2.43}$$

to obtain

$$\frac{-1}{\pi} Im \int_{-\infty}^{E_F} d\epsilon Tr\{\delta HG\delta HG\} = \frac{-1}{2\pi S^2} \sum_{ij} Im \int_{-\infty}^{E_F} d\epsilon \delta\mathbf{S}_i \cdot \delta\mathbf{S}_j Tr_L\{\Delta_i G_{ij}^{\downarrow} \Delta_j G_{ji}^{\uparrow}\} \ . \tag{2.44}$$

The second term of identity (2.43) doesn't appear because the symmetric sum in i, j. Both parts of $\delta^2 E_0$ can be added together to form an isotropic exchange:

$$\delta^2 E_0 = \frac{1}{4} \sum_{ij} J_{ij}^0 |\delta\mathbf{S}_i - \delta\mathbf{S}_j|^2 \ . \tag{2.45}$$

Where we have defined the exchange constant as

$$J_{ij}^0 = \frac{1}{\pi S^2} Im \int_{-\infty}^{E_F} d\epsilon Tr_L\{\Delta_i G_{ij}^{\downarrow} \Delta_j G_{ji}^{\uparrow}\} \ . \tag{2.46}$$

The terms δE_λ and $\delta^2 E_0$ are present in the work of Mazurenko [62]. The rest of the energy variations, considering terms of higher order in the spin orbit coupling were neglected in that formalism, and they correspond to our extension of that work. The terms present in $\delta^2 E_\lambda$ and $\delta^2 E_{\lambda^2}$ has one of the following structures:

(i) $E_{onsite}^{(n)} = \frac{-1}{\pi} Im \int_{-\infty}^{E_F} d\epsilon Tr\{\delta^2 HG^{(n)}\}$.

(ii) $E_{intersite}^{(n1,n2)} = \frac{-1}{\pi} Im \int_{-\infty}^{E_F} d\epsilon Tr\{\delta HG^{(n1)}\delta HG^{(n2)}\}$.

On-site contributions can be calculated as before, expanding the sum in the site and spin indices we get

$$E_{onsite}^{(n)} = \frac{1}{2\pi S^2} \sum_{i} Im \int_{-\infty}^{E_F} d\epsilon |\psi_i|^2 Tr_L\{\Delta_i (G_{ii}^{(n)\uparrow\uparrow} - G_{ii}^{(n)\downarrow\downarrow})\}$$
$$= \sum_{i} K_i^{(n)} |\delta\mathbf{S}_i|^2 \ . \tag{2.47}$$

Where the on-site constant $K_i^{(n)}$ was defined as

$$K_i^n = \frac{1}{2\pi S^2} Im \int_{-\infty}^{E_F} d\epsilon Tr_L \{\Delta_i (G_{ii}^{(n)\uparrow\uparrow} - G_{ii}^{(n)\downarrow\downarrow})\} \ . \tag{2.48}$$

Now we calculate the generic $E_{intersite}^{(n_1,n_2)}$ term, expanding the trace it takes the form

$$E_{intersite}^{(n1,n2)} = \frac{-1}{4\pi S^2} \sum_{ij} Im \int_{-\infty}^{E_F} d\epsilon Tr_L \{\psi_i \psi_j \Delta_i G_{ij}^{(n_1)\uparrow\downarrow} \Delta_j G_{ji}^{(n_2)\uparrow\downarrow} + \psi_i^* \psi_j^* \Delta_i G_{ij}^{(n_1)\downarrow\uparrow} \Delta_j G_{ji}^{(n2)\downarrow\uparrow}$$
$$+ \psi_i^* \psi_j \Delta_i G_{ij}^{(n1)\downarrow\downarrow} \Delta_j G_{ji}^{(n_2)\uparrow\uparrow} + \psi_i \psi_j^* \Delta_i G_{ij}^{(n_1)\uparrow\uparrow} \Delta_j G_{ji}^{(n2)\downarrow\downarrow}\} \ . \tag{2.49}$$

The third and fourth terms can be reordered using (2.43). For the first and second terms, we use the following identity:

$$Im\{\psi_i \psi_j a + \psi_i^* \psi_j^* b\} = \delta\mathbf{S}_i \sigma_z \delta\mathbf{S}_j Im\{a+b\} + \delta\mathbf{S}_i \sigma_x \delta\mathbf{S}_j Re\{a-b\} \ . \tag{2.50}$$

Where σ_z and σ_x are pauli matrices, and $\delta\mathbf{S}_{i,j}$ were used as two dimensional vectors. Using identities (2.43) and (2.50) the inter-site contribution can be written as

$$E_{intersite}^{(n_1,n_2)} = \frac{-1}{2} \sum_{ij} \delta\mathbf{S}_i \cdot \begin{pmatrix} J_{ij}^{(n_1,n_2)} + \alpha_{ij}^{(n_1,n_2)} & \beta_{ij}^{(n_1,n_2)} + d_{ij}^{(n_1,n_2)} \\ \beta_{ij}^{(n_1,n_2)} - d_{ij}^{(n_1,n_2)} & J_{ij}^{(n_1,n_2)} - \alpha_{ij}^{(n_1,n_2)} \end{pmatrix} \cdot \delta\mathbf{S}_j \ . \tag{2.51}$$

Where we have defined the following quantities:

$$J_{ij}^{(n_1,n_2)} = \frac{1}{2\pi S^2} Im \int_{-\infty}^{E_F} d\epsilon Tr_L \{\Delta_i G_{ij}^{(n1)\downarrow\downarrow} \Delta_j G_{ji}^{(n_2)\uparrow\uparrow} + \Delta_i G_{ij}^{(n_1)\uparrow\uparrow} \Delta_j G_{ji}^{(n_2)\downarrow\downarrow}\} \ ,$$

$$d_{ij}^{(n_1,n_2)} = \frac{1}{2\pi S^2} Re \int_{-\infty}^{E_F} d\epsilon Tr_L \{\Delta_i G_{ij}^{(n1)\downarrow\downarrow} \Delta_j G_{ji}^{(n_2)\uparrow\uparrow} - \Delta_i G_{ij}^{(n_1)\uparrow\uparrow} \Delta_j G_{ji}^{(n_2)\downarrow\downarrow}\} \ ,$$

$$\alpha_{ij}^{(n_1,n_2)} = \frac{1}{2\pi S^2} Im \int_{-\infty}^{E_F} d\epsilon Tr_L \{\Delta_i G_{ij}^{(n_1)\uparrow\downarrow} \Delta_j G_{ji}^{(n_2)\uparrow\downarrow} + \Delta_i G_{ij}^{(n_1)\downarrow\uparrow} \Delta_j G_{ji}^{(n2)\downarrow\uparrow}\} \ ,$$

$$\beta_{ij}^{(n_1,n_2)} = \frac{1}{2\pi S^2} Re \int_{-\infty}^{E_F} d\epsilon Tr_L \{\Delta_i G_{ij}^{(n_1)\uparrow\downarrow} \Delta_j G_{ji}^{(n_2)\uparrow\downarrow} - \Delta_i G_{ij}^{(n_1)\downarrow\uparrow} \Delta_j G_{ji}^{(n2)\downarrow\uparrow}\} \ . \tag{2.52}$$

Now we are ready to calculate $\delta^2 E_\lambda$ and $\delta^2 E_{\lambda^2}$, the linear term in the spin-orbit coupling has the form

$$\delta^2 E_\lambda = E_{onsite}^{(1)} + E_{intersite}^{(0,1)} + E_{intersite}^{(1,0)} \ . \tag{2.53}$$

The quadratic term is

$$\delta^2 E_{\lambda^2} = E_{onsite}^{(2)} + E_{intersite}^{(0,2)} + E_{intersite}^{(2,0)} + E_{intersite}^{(1,1)} \ . \tag{2.54}$$

Note that $\alpha_{ij}^{(0,1)} = \alpha_{ij}^{(1,0)} = \alpha_{ij}^{(0,2)} = \alpha_{ij}^{(2,0)} = \beta_{ij}^{(1,0)} = \beta_{ij}^{(0,1)} = \beta_{ij}^{(0,2)} = \beta_{ij}^{(2,0)} = 0$, because $G_{ij}^{(0)} = G_{ij}$ is diagonal in spin basis. Therefore, up to linear order in the spin-orbit coupling, only appears a correction to the isotropic Heisenberg exchange, and possibly an anti-symmetric exchange d_{ij}. However, when quadratic terms in spin orbit coupling are included, anomalous terms that breaks the $x - y$ isotropy and mix x and y spin-components can be

present.

Let's define $\alpha_{ij} = \alpha_{ij}^{(1,1)}$, and $\beta_{ij} = \beta_{ij}^{(1,1)}$ because these are the only non zero contributions with that structure. Also we define the following linear terms in the spin-orbit coupling:

$$J_{ij}^{(1)} = J_{ij}^{(0,1)} + J_{ij}^{(1,0)} \ ,$$
$$d_{ij}^{(1)} = d_{ij}^{(0,1)} + d_{ij}^{(1,0)} \ . \tag{2.55}$$

and in analogous way, the quadratic terms in spin orbit coupling can be grouped as

$$J_{ij}^{(2)} = J_{ij}^{(0,2)} + J_{ij}^{(2,0)} + J_{ij}^{(1,1)} \ ,$$
$$d_{ij}^{(2)} = d_{ij}^{(0,2)} + d_{ij}^{(2,0)} + d_{ij}^{(1,1)} \ . \tag{2.56}$$

We finally write the isotropic exchange, the anti-symmetric exchange, and the on-site constant as

$$J_{ij} = J_{ij}^{(0)} + J_{ij}^{(1)} + J_{ij}^{(2)} \ ,$$
$$d_{ij} = d_{ij}^{(1)} + d_{ij}^{(2)} \ ,$$
$$K_i = K_i^{(1)} + K_i^{(2)} \ ,$$
$$\mathbf{h}_i = \mathbf{h}_i^{(1)} + \mathbf{h}_i^{(2)} \ . \tag{2.57}$$

2.4.   From electrons to magnons in CrI$_3$

In the last section, we started from an effective electronic Hamiltonian, and from it, we obtained the energy variation of a ground state's perturbation, by rotating the magnetization on each site an arbitrary small-angle $\delta\phi_i$. We perform this analysis, including the effects of the spin-orbit coupling, up to quadratic order. In the material CrI_3 as has been mentioned before, the Chromium sites are the magnetic ones, so the energy variations δH_{ii} and $\delta^2 H_{ii}$ only has non zero contributions on chromium sites.

In order to calculate the corrections to the original Green's function, we need an explicit form for the spin-orbit Hamiltonian H^{SO}. For simplicity, we include the spin-orbit coupling only in Iodine atoms. It has been widely argued that the spin-orbit of ligands plays a central role in the description of this material [49], and for this reason, we neglect SOC in the magnetic chromium atoms.

As was mentioned in chapter 1, we use three p-like orbitals on each Iodine atom. From Appendix B. of chapter 1, this orbitals can be written in terms of eigenstates of L_z and $\mathbf{L}^2$ as:

$$|p_x\rangle = \frac{1}{\sqrt{2}}(|1, -1\rangle - |1, 1\rangle) ,$$

$$|p_y\rangle = \frac{1}{\sqrt{2}}(|1, -1\rangle + |1, 1\rangle) , \qquad (2.58)$$

$$|p_z\rangle = |1, 0\rangle .$$

Where $|l, m\rangle$ are the angular eigenfuncions of the hydrogen-like atom with total angular momentum $\mathbf{L}^2 = \hbar^2 l(l + 1)$ and z-component $L_z = \hbar m$. By projecting $H_k^{SO} = \lambda \boldsymbol{\sigma} \cdot \mathbf{L}$ in this basis, each Iodine block takes the form:

$$H_k^{SO} = \lambda \begin{pmatrix} 0 & -i\sigma_z & i\sigma_y \\ i\sigma_z & 0 & -i\sigma_x \\ -i\sigma_y & i\sigma_x & 0 \end{pmatrix} . \qquad (2.59)$$

This matrix is the represented in the basis $\{|p_x\rangle, |p_y\rangle, |p_z\rangle\}$, and each element is a 2×2 matrix representing the spin basis. With this $G^{(1)}$ is:

$$G_{ij}^{(1)} = \sum_k G_{ij} H_k^{SO} G_{kj} . \qquad (2.60)$$

The sum in k runs every Iodine atom in the system. For practical purposes, we only need to include a few unit cells around the link (i, j) to ensure the required convergence. The second-order correction is:

$$G_{ij}^{(2)} = \sum_{kk'} G_{ik} H_k^{SO} G_{kk'} H_{k'}^{SO} G_{k'j} . \qquad (2.61)$$

As before, the sums over k and k' only visit the Iodine's sites. $G_{ij}^{(1)}$ is the sum over all processes in which the electron hops from the chromium i, to an Iodine atom, and then to the chromium j. The second-order Green's function $G_{ij}^{(2)}$ represents all the processes in which two Iodine's sites are visited before the electron returns to a Chromium atom.

The energy variation calculated in the last section can be written as:

$$\Delta E = -\sum_i \mathbf{h}_i \cdot \delta \mathbf{S}_i - \sum_i \delta \mathbf{S}_i \cdot \mathcal{A}'_{ii} \cdot \delta \mathbf{S}_i - \frac{1}{2} \sum_{ij(i \neq j)} \delta \mathbf{S}_i \cdot \mathcal{J}_{ij} \cdot \delta \mathbf{S}_j . \qquad (2.62)$$

With $\mathbf{h}_i = \mathbf{h}_i^{(1)} + \mathbf{h}_i^{(2)}$ (see eqs. (2.37) and (2.39)). The exchange matrix has the form:

$$\mathcal{J}_{ij} = J_{ij}\sigma_0 - id_{ij}\sigma_y + \alpha_{ij}\sigma_z + \beta_{ij}\sigma_y$$
$$= \begin{pmatrix} J_{ij} + \alpha_{ij} & \beta_{ij} + d_{ij} \\ \beta_{ij} - d_{ij} & J_{ij} - \alpha_{ij} \end{pmatrix} . \qquad (2.63)$$

And the on-site matrix is:

$$\mathcal{A}'_{ii} = -(K_i + \frac{1}{2}J_{ii}^{(0)} + \frac{1}{2}H_W^i)\sigma_0 + \frac{1}{2}\mathcal{J}_{ii} . \qquad (2.64)$$

Here $H_W^i = \sum_{j,(j \neq i)} J_{ij}^{(0)}$ is the Weiss field associated with the isotropic exchange on the site

i. The magnetic constants used here are those defined in (2.57). When we calculate these constants on CrI_3, we found that several of them are zero. For example, due to the center of inversion in the middle of the Cr - Cr link, the exchange matrix should be symmetric. This is confirmed and we get $d_{ij} = 0$ for every link (i, j). Also, we calculate that $\mathbf{h}_i$ is zero in both Cr sites, supporting the fact that the ground state is the z-polarized ferromagnetic state.

The rest of the magnetic couplings of $\mathcal{J}_{ij}$ are relevant only in nearest neighbors (NN) and next-nearest neighbors (NNN). However, for the NNN we found that, for reasonable values of the spin-orbit coupling, only $J_{ij}^{(0)}$ and $J_{ij}^{(2)}$ are non-negligible, and for fixed λ both constants are equal on all NNN-links, this happens because the NNN-neighbours of a given site are connected by a three-fold rotation $R_z(\frac{2\pi}{3})$ or a mirror symmetry Π_{uz}, Π_{vz}, and both symmetries are present in the crystal. For the NN-links, we have the same values of $J^{(0)}$ and $J^{(2)}$, but three different values for α and β, one for each link.
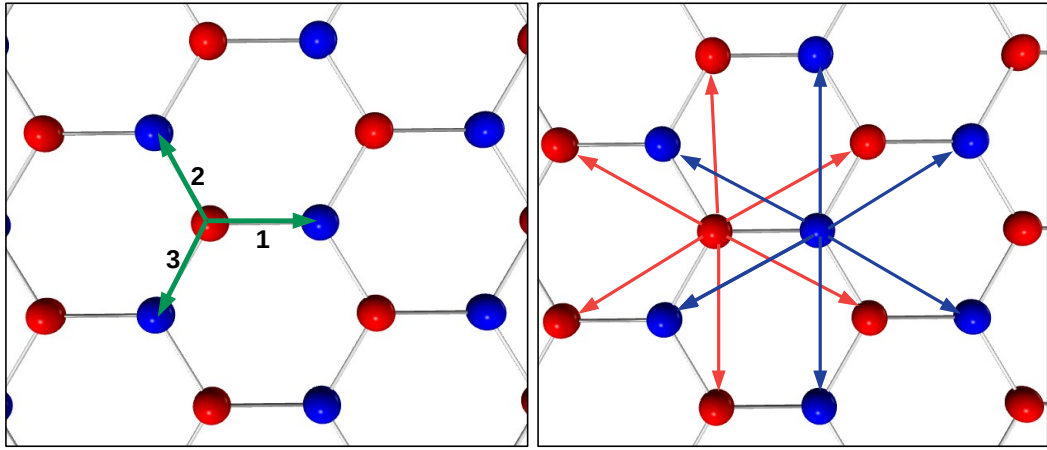
Figure 2.1: Bipartite honeycomb lattice of magnetic Cr sites. A lattice is drawn in red, and B lattice is drawn in blue. **(Left)** Nearest neighbours links enumerated from 1 to 3 are represented as green arrows. **(Right)** Next nearest neighbours links, AA and BB links are represented by red and blue arrows respectively.

Moreover, the on-site matrix $\mathcal{A}'$ is equal on both Cr-sites, and it is diagonal. So it could be written in the simpler form:

$$\mathcal{A}' = -(K^{(2)} + \frac{1}{2}H_W - \frac{1}{2}J_{00}^{(2)})\sigma_0 . \tag{2.65}$$

In order to obtain the effective Hamiltonian without SOC, we use the Kanamori Hamiltonian in the Hartree-Fock approximation, as was explained in chapter 1. Choosing $U = 2.5eV$ and $J_H = 0.4U$, for the intra-orbital electronic repulsion, and the intra-atomic exchange, respectively. We obtain the magnetic couplings mentioned previously. Isotropic exchange couplings for NN and NNN are shown in fig 2.2. This exchange should be understood as the mean value between $\mathcal{J}_{xx}$ and $\mathcal{J}_{yy}$, and as we will see in the next section, one part of $J_{ij}^{(2)}$ is going to modify the Heisenberg exchange constant, and some part will contribute to an

anisotropic exchange. Fig 2.3 shows α_{ij} and β_{ij} as function of the spin-orbit coupling, for the three NN-links,m enumerated as shown in fig 2.1. Some relations in these coefficients are observed. For example $\alpha_2 = \alpha_3$, $\beta_1 = 0$ and $\beta_2 = -\beta_3$. These terms are responsible for generating an anisotropic exchange between the nearest neighbors. In the next section, it will become clear why these relations are consistent with a specific form of the anisotropic exchange, which is forced by the symmetries of the crystal. Finally, in fig 2.4 are shown the coefficients that contributes to the on-site matrix $\mathcal{A}'$ in eq. (2.65).
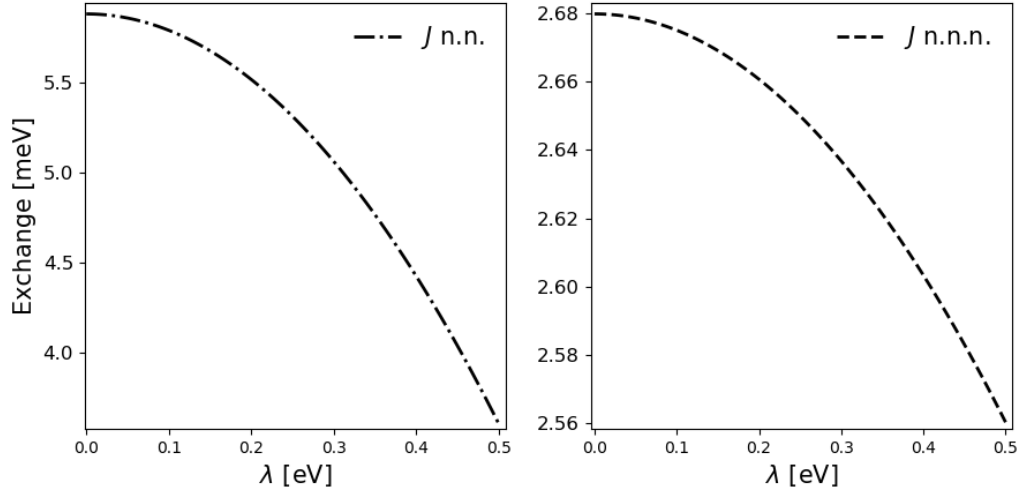
Figure 2.2: Exchange constants defined as $J = J^{(0)} + J^{(2)}$ for different links, as functiopn of the spin orbit coupling λ. **(Left)** Exchange between nearest neighbours $J = 5.88 \text{ meV} - 9.1 \times 10^{-3}\lambda^2/\text{eV}$. **(Right)** Exchange between next nearest neigbbours, defined as $J = 2.68 meV - 4.8 \times 10^{-4}\lambda^2/\text{eV}$.
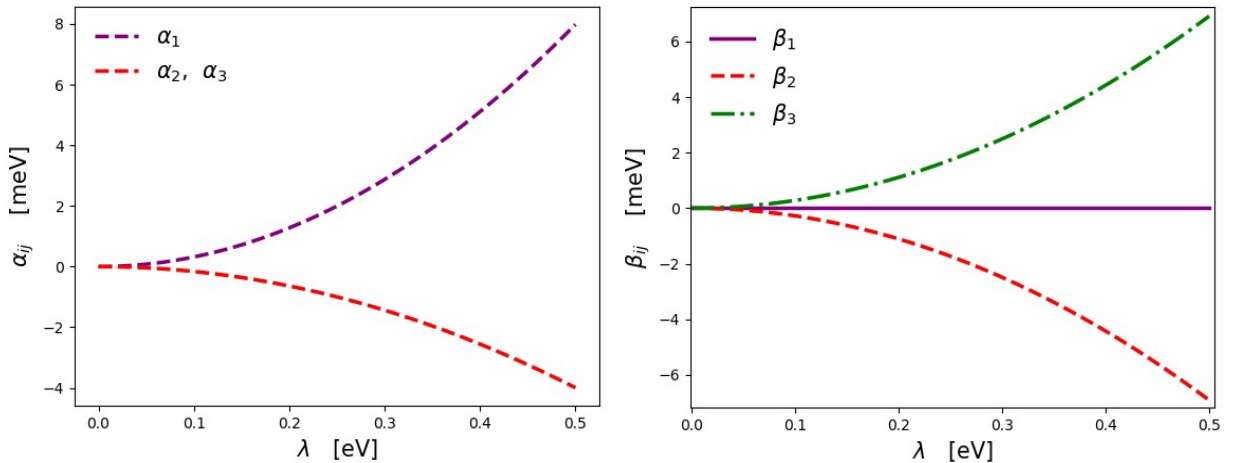
Figure 2.3: Couplings α_{ij} **(left)**, and β_{ij} **(right)** for the nearest neighbours, as function of the spin orbit coupling. Links are enumerated as shown in fig 2.1. $\alpha_1 = 0.032\lambda^2/eV$, $\alpha_2 = \alpha_3 = -0.016\lambda^2/eV$, $\beta_1 = 0$, $\beta_3 = -\beta_2 = 0.028\lambda^2/eV$.
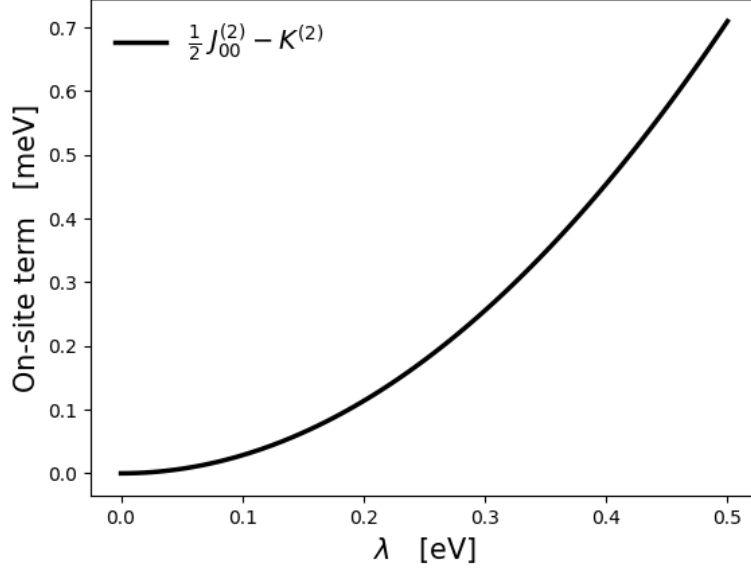
Figure 2.4: On-site terms of eq. (2.65), as function of the spin orbit coupling. The curve is parametrized by $2.8 \times 10^{-3} \lambda^2 / \text{eV}$

Within the formalism developed in appendixes A and B of this chapter, the spectrum of the magnons can be calculated. In fig 2.5 it is shown the magnonic spectrum with and without spin-orbit coupling. Note that when we turn on the spin-orbit coupling in the Iodine sites, a gap is opened for infinite wavelength ($\mathbf{\Gamma}$ point), and also the degeneration at $\mathbf{K}$ and $\mathbf{K'}$ points are lifted out. The gap at $\mathbf{\Gamma}$ point is particularly significant because it is the reason for the stable ferromagnetism in the bi-dimensional magnet CrI_3. According to the Mermin-Wagner theorem [65], there is no magnetic order for finite temperature in two dimensions, if $SU(2)$ symmetry is preserved. The gap at $\mathbf{\Gamma}$ is a consequence of that symmetry is broken, and the origin of this gap is particularly important in order to understand CrI_3 magnetism, and others bi-dimensional magnets.
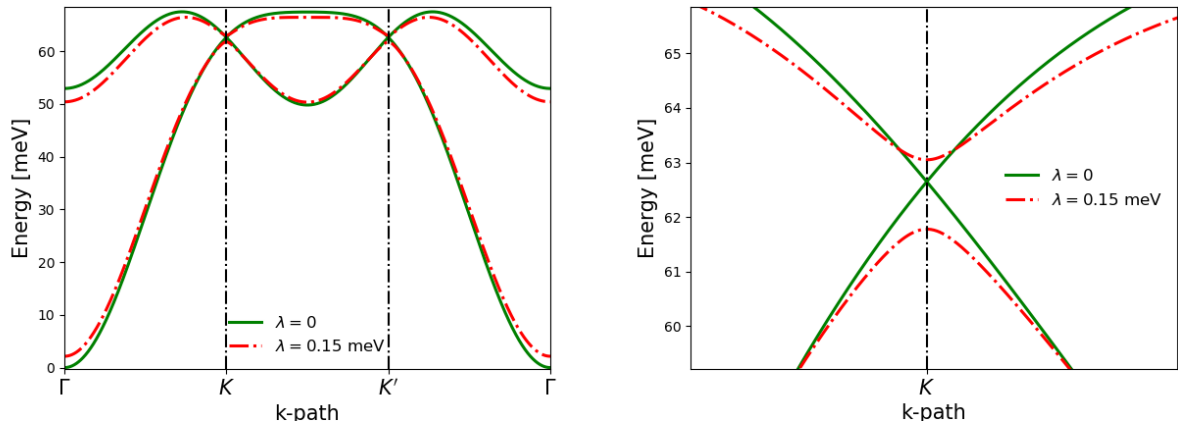
Figure 2.5: (a) Magnon's bands for $\lambda = 0$ (green) and $\lambda = 0.15 eV$ (red). (b) Energies in the vicinity of $\mathbf{K}$ point.

2.5. Spin Hamiltonian for the CrI₃ ferromagnet

The technique developed in the last section is easy to generalize to a uniform spin texture polarized in an arbitrary axis $\hat{\mathbf{n}}$. The collinear Hamiltonian obtained by the Hartree Fock approximation is independent of the spin polarization, and the spin-orbit coupling is introduced as a perturbation in the collinear Green's function. Once we choose a coordinate system $\{x', y', z'\}$, and polarize the magnetization in z'-direction, the technique described in the last section allows to us to obtain the quadratic form of H in terms of $\delta S_{x'}$ and $\delta S_{y'}$. We only have to make the replacement $H_{SO} \to R^\dagger H_{SO} R$, with R being the SU(2) spin-rotation connecting both coordinate systems. Given a $\{x', y', z'\}$ basis, we can permute the axes employing a (111) three-fold rotation, and so get all the 2×2 blocks of the exchange matrix.

(a)

(b)
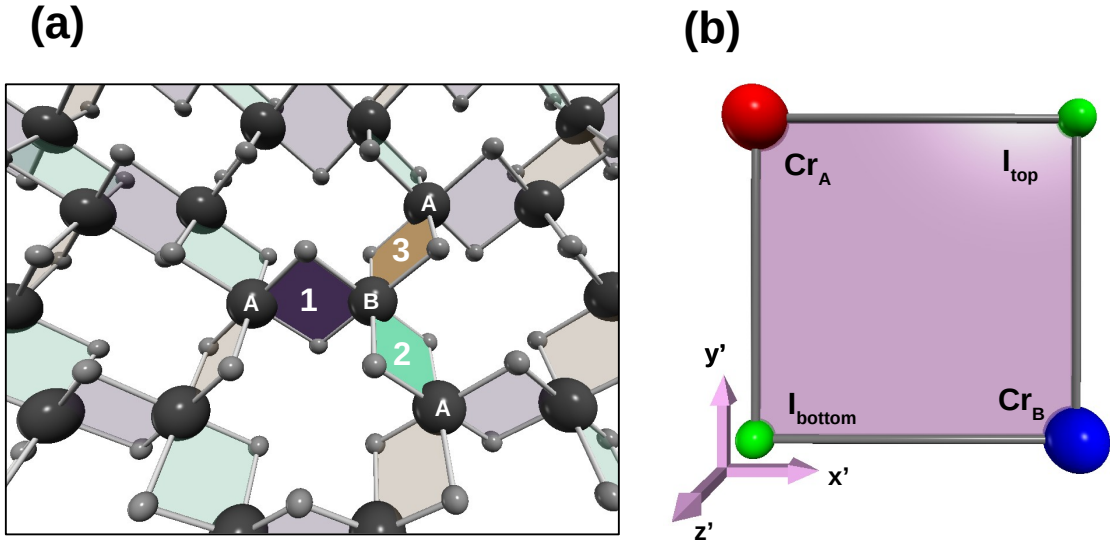
Figure 2.6: **(a)** Top view of the CrI_3 layer, with different plaquettes Cr_2I_2 highlighted in color. Three kind of NN-links are enumerated from 1 to 3, just as in fig. 2.1. **b** Plaquette 1 in the coordinate system $\{x', y', z'\}$. Each plaquette is composed by two Cr sites (A (red) and B (blue)), and two Iodines (green) I_{top} and I_{bottom}. Axis z' is normal to the plaquette. Plaquettes 2 and 3 can be obtained by a (111) three fold rotation, or equivalently by permuting the axes x', y', z'.

For each NN-link, we chose the basis with z' pointing normal to the Cr_2I_2 plaquette, and x', y' oriented with the $Cr - I$ links, as shown in fig. 2.6. In this basis $\{x', y', z'\}$ the exchange matrix has the form:

$$\mathcal{J}_1 = \begin{pmatrix} J & -\Gamma & \Gamma \\ -\Gamma & J & \Gamma \\ \Gamma & \Gamma & J+K \end{pmatrix} . \tag{2.66}$$

With $J = 5.88$ meV $+ 1.18 \times 10^{-2}\lambda^2/$eV, $K = -6.06 \times 10^{-2}\lambda^2/$eV and $\Gamma = 8.9 \times 10^{-3}\lambda^2/$eV. Exchange matrices of the other two links $\mathcal{J}_2$ and $\mathcal{J}_3$ have the same form when oriented in the basis $\{y', z', x'\}$ and $\{z', x', y'\}$ respectively, choosing the third component of the basis as the spin polarization axis. In a recent article [45], a similar formalism is applied to CrI_3

neglecting the spin-orbit coupling. The authors found that the isotropic exchange has two contributions. The first one is the antiferromagnetic direct exchange between occupied e_g orbitals. There is also another ferromagnetic contribution that gives arise from the superexchange paths $Cr - I - Cr$ in the Cr_2I_2 plaquette of the link. The total Heisenberg exchange is ferromagnetic and isotropic, but when the spin-orbit coupling is turned on, it appears an an-isotropic exchange from these $Cr - I - Cr$ paths, which prefers the axis normal to the plaquette. The last is the origin of the K term in the exchange matrix. As we will see later, this link dependent anisotropy of the exchange is consistent with the Kitaev model, and in the next chapter, we will prove that the gap at $\boldsymbol{K}$ point of the magnon's spectrum is generated by this non-zero Kitaev constant K (see fig 2.5).

An interesting fact is that Γ is originated from the distortion of the octahedral environment of each Cr site. We support this claim developing a naive tight-binding model, which includes only site energies, nearest neighbors hoppings $(Cr - I)$, and the crystal field on each atom. Each NN-hopping matrix depends on two Slater-Koster parameters $V_{pd\sigma}$ and $V_{pod\pi}$, and the relative positions of the atoms. When we perform the Green's functions method on the tight-binding model with the ideal atomic positions (when the local cubic symmetry is preserved), we obtain $\Gamma = 0$, and it becomes non-zero when the actual atomic positions are used instead.
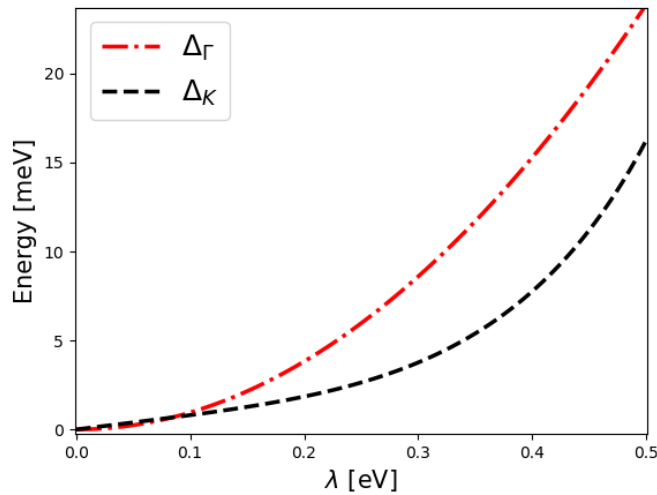
Figure 2.7: Energy gaps at $\boldsymbol{\Gamma}$ point (Δ_Γ) and $\boldsymbol{K}$ point (Δ_K) as function of the spin orbit coupling λ.

As a final comment with respect to the exchange matrices, we have to say that each plaquette contributes to approximately the 80% of the constants K and Γ, as should be expected. With this, we mean that super-exchange paths that connects two Cr sites, through I atoms, plays a central role in the magnetic couplings. The other 20% comes from higher-order paths. We observed this by decomposing α_{ij} and β_{ij} as a sum of all possible paths, and integrating different processes separately.

To distinguish between the single-ion anisotropy and the on-site contribution of the ex-

change, we remember the form of the on-site matrix from (2.8):

$$\mathcal{A}'_{ii} = \mathcal{A}_{ii} - (\mathcal{A}^{zz}_{ii} + \frac{1}{2} \sum_{j \in nn(i)} \mathcal{J}^{zz}_{ij}) \sigma_0 . \tag{2.67}$$

The on-site matrix was founded to be diagonal, so $\mathcal{A}^{xx} = \mathcal{A}^{yy} = \mathcal{A}^{xy} = \mathcal{A}^{yx} = 0$. Defining $A_0 = \mathcal{A}^{zz}_{ii}$ as the single ion anisotropy, we can compare it with (2.65), obtaining:

$$A_0 = K_0^{(2)} - \frac{1}{2} J_{00}^{(2)} - \frac{K}{2} - \Gamma = 1.86 \times 10^{-2} \lambda^2 / \text{eV} . \tag{2.68}$$

Finally, the spin-$\frac{3}{2}$ Hamiltonian takes the form:

$$H = - \sum_{\langle i,j \rangle} \mathbf{S}_i \mathcal{J}_{ij} \mathbf{S}_j - J_{nnn} \sum_{\langle\langle i,j \rangle\rangle} \mathbf{S}_i \cdot \mathbf{S}_j - A_0 \sum_i (S_i^z)^2 . \tag{2.69}$$

The first term of this Hamiltonian is the Heisenberg-Kitaev-Γ model (HKΓ), with matrices $\mathcal{J}_{ij} \in \{\mathcal{J}_1, \mathcal{J}_2, \mathcal{J}_3\}$. The second term is an isotropic next nearest neighbor's exchange, and the last term is the single-ion anisotropy. Magnetic constants involved in (2.69) are shown in fig. 2.8 as function of the spin-orbit coupling. We conclude that the magnetic degrees of freedom in CrI_3 are well described not by the XXZ model, proposed in [49], but by the Hamiltonian (2.69). The main difference between both models is that HKΓ model has non zero components $\mathcal{J}_{xy}$ in the crystal basis $\{x, y, z\}$, behavior that is absent in the XXZ model. These terms are calculated from the coefficients α_{ij} and β_{ij}; both defined in the last section. The ground state of (2.69) is the $\hat{\mathbf{z}}$-polarized ferromagnetic state, and its spectrum was already calculated in the last section (see fig 2.5). Gaps at $\mathbf{\Gamma}$ and $\mathbf{K}$ points are plotted as function of the spin-orbit coupling in fig 2.7.

The existence of bidimensional magnets, whose spin freedom degrees are well described within a modified Kitaev's model, opens promising opportunities for studying and controlling the quantum-spin-liquid (QSL) phase [85, 5]. QSLs are topological states of matter which exhibit remarkable features. For example, QSLs have been proposed as potential candidates to protect quantum information from decoherence.

The spin Hamiltonian is consistent with the symmetries of the crystal, but it is important no note that the values of the constants depend not only on the spin-orbit parameter but also on of the on-site potential Δ_i, which in turn depend on the Kanamori parameters U and J_H. A different choice for these Hubbard parameters could lead to different values of J, K, Γ, and A_0, but the same symmetries have to be preserved. Similar results, has been obtained recently by ab-initio methods [92] and by experimental ferromagnetic resonance [52]. Both works propose different magnitudes for the Kitaev's constant, so an exact value for the magnetic couplings in the CrI_3 ferromagnet is not clear enough yet. However, the technique developed in this chapter opens a novel way to characterize the angle-dependence of the exchange in bi-dimensional materials or bi-dimensional hetero-structures in which the spin-orbit coupling is small with respect to the on-site potential (fixed by U and J_H). Therefore it can be treated as a perturbation. The last is the case of Mott insulators, in which ligands are heavy atoms, and therefore its spin-orbit coupling plays an important role. By improving the techniques to obtain the effective tight-binding Hamiltonian H_{TB}, more precise

results can be obtained.

In the next chapter, we propose a simplified version of (2.69), in which the next nearest neighbors hoppings are neglected, and Γ is assumed to be zero. We will use a classical perspective, and using the linearized Landau Lifchitz equation. We will obtain analytical expressions for the magnon's spectrum. The presence of the Kitaev parameter is going to be particularly important because it will lead to a non-trivial topological structure for the magnons.
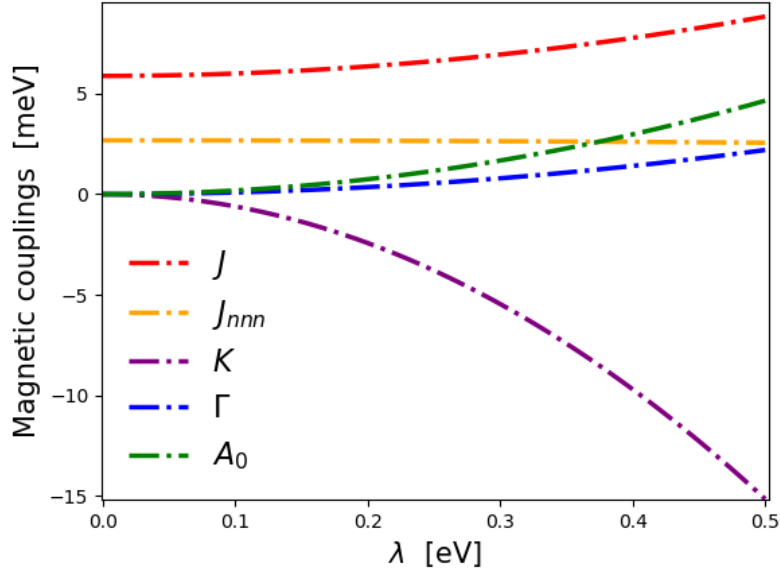

Figure 2.8: Several magnetic couplings of eq. (2.69) as function of λ.

2.6. Appendixes

A. Magnonic spectrum

In this section, we calculate the spectrum of spin waves associated a the quadratic Hamiltonian, such as the one present in eq. (2.6). This Hamiltonian represents the energy of a magnetic texture, which is slightly perturbed from the ground state. An expansion like this one could be obtained from a specific model, or a full electron calculation, as we will see in the next section. Let us write the quadratic Hamiltonian as:

$$ H = -\sum_i \mathbf{h}_i \cdot \delta \mathbf{S}_i - \sum_i \delta \mathbf{S}_i \cdot \mathcal{A}'_{ii} \cdot \delta \mathbf{S}_i - \frac{1}{2} \sum_{\langle i,j \rangle} \delta \mathbf{S}_i \cdot \mathcal{J}_{1,ij} \cdot \delta \mathbf{S}_j - \frac{1}{2} \sum_{\langle\langle i,j \rangle\rangle} \delta \mathbf{S}_i \cdot \mathcal{J}_{2,ij} \cdot \delta \mathbf{S}_j \ , \quad (2.70) $$

with $\delta \mathbf{S_i} = (S_i^x, S_i^y)^T$. Note that in last equation $\mathcal{A}'_{ii}$, $\mathcal{J}_{1,ij}$ and $\mathcal{J}_{2,ij}$ are matrices of dimensions 2×2. This Hamiltonian includes exchange between nearest neighbors and next nearest neighbors. Now we incorporate the specific geometry that we are concerned with. Magnetic sites form a honeycomb lattice, so we consider two sublattices labeled by $\{a, b\}$. We use $S_\alpha(\mathbf{r})$ to name the spin at the site $\alpha \in \{a, b\}$ in the unit cell located at $\mathbf{r}$. The Cartesian's components of the lattice vectors are:

$$ \mathbf{a_1} = a_0 \left(\frac{\sqrt{3}}{2}, \frac{1}{2}, 0 \right) \ , $$
$$ \mathbf{a_2} = a_0 \left(\frac{\sqrt{3}}{2}, -\frac{1}{2}, 0 \right) \ . \quad (2.71) $$

Here a_0 is the lattice constant. The nearest neighbour's distance is $d_{ab} = a_0/\sqrt{3}$. Considering exchange between nearest and next nearest neighbours only, the Hamiltonian can be written as:

$$ H = H_h + H_A + H_{J1} + H_{J2} \ . \quad (2.72) $$

Where we have defined the different contributions as:

$$ H_h = -\sum_{\mathbf{r}} \sum_{\alpha \in \{a,b\}} \mathbf{h}_\alpha \cdot \delta \mathbf{S}_\alpha(\mathbf{r}) \ , \quad (2.73) $$

$$ H_A = -\sum_{\mathbf{r}} \sum_{\alpha \in \{a,b\}} \delta \mathbf{S}_\alpha(\mathbf{r}) \cdot \mathcal{A}'_\alpha \cdot \delta \mathbf{S}_\alpha(\mathbf{r}) \ , \quad (2.74) $$

$$ H_{J1} = -\sum_{\mathbf{r}} \delta \mathbf{S}_a(\mathbf{r}) \cdot \sum_p \mathcal{J}_{1p} \cdot \delta \mathbf{S}_b(\mathbf{r} + \mathbf{r}_p) \ , \quad (2.75) $$

$$ H_{J2} = -\frac{1}{2} \sum_{\mathbf{r}} \sum_{\alpha \in \{a,b\}} \delta \mathbf{S}_\alpha \cdot \sum_q \mathcal{J}_{2q} \cdot \delta \mathbf{S}_\alpha(\mathbf{r} + \mathbf{r}_q) \ . \quad (2.76) $$

Let us pay attention to the exchange contributions. Index $p \in \{1, 2, 3\}$ labels the nearest neighbours links from site a to site b. Vectors $\mathbf{r}_p$ are the lattices vectors corresponding to these links (so the position of the site inside the unit cell is ignored). On the other hand, $q \in \{1, 2, 3, 4, 5, 6\}$ labels the links between next-nearest neighbors, and vectors $\mathbf{r}_q$ correspond

to the lattices vectors associated with these links. Note hat nearest-neighbor links always join a site a with a site b, while the next nearest neighbor links are of type $a - a$ or $b - b$. In fig 2.9 different links to nearest neighbours and next-nearest neighbours are enumerated.
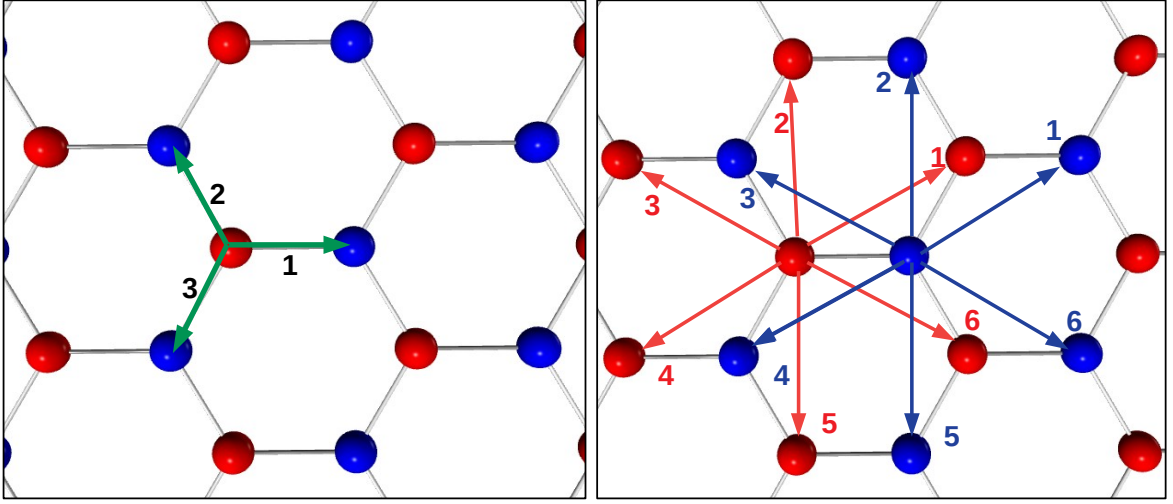
Figure 2.9: Links of Honeycomb lattice. Sub-lattices A and B are represented by red and blue spheres respectively. **(Left)** Links to nearest neighbours are shown as green arrows. **(Right)** Links to next nearest neighbours are drawn with red (AA-links) and blue (BB-links) arrows.

Writing the lattice vectors associated with each link vector as $\mathbf{r}_{p,q} = n_1 \mathbf{a_1} + n_2 \mathbf{a_2}$, nearest and next nearest neighbour's links can be written as:

Nearest neighbours		
$\mathbf{r}_p$	n_1	n_2
$\mathbf{r}_1$	0	0
$\mathbf{r}_2$	0	−1
$\mathbf{r}_3$	−1	0

Next nearest neighbours		
$\mathbf{r}_q$	n_1	n_2
$\mathbf{r}_1$	1	0
$\mathbf{r}_2$	1	−1
$\mathbf{r}_3$	0	−1
$\mathbf{r}_4$	−1	0
$\mathbf{r}_5$	−1	1
$\mathbf{r}_6$	0	1

Now we use the Holstein Primakoff's transformation, to express the spin Hamiltonian in

terms of bosonic operators:

$$
\begin{aligned}
S_\alpha^x(\mathbf{r}) &= \sqrt{\frac{S}{2}}\left(\alpha_\mathbf{r}^\dagger + \alpha_\mathbf{r}\right) , \\
S_\alpha^y(\mathbf{r}) &= i\sqrt{\frac{S}{2}}\left(\alpha_\mathbf{r}^\dagger - \alpha_\mathbf{r}\right) , \\
S_\alpha^z(\mathbf{r}) &= S - \alpha_\mathbf{r}^\dagger\alpha_\mathbf{r} .
\end{aligned}
\tag{2.77}
$$

With $\alpha \in \{a, b\}$ being the annihilation operator of bosons on the respective sub-lattice. Now we replace on each contribution of the Hamiltonian, and conserving terms up to quadratic order in bosonic operators we get

$$
H_h = -\sqrt{\frac{S}{2}}\sum_\mathbf{r}\sum_{\alpha\in\{a,b\}}\tilde{h}_\alpha\alpha_\mathbf{r}^\dagger + \tilde{h}_\alpha^*\alpha_\mathbf{r} ,
\tag{2.78}
$$

with $\tilde{h}_\alpha = h_\alpha^x + ih_\alpha^y$. This term only appears if $\hat{\mathbf{z}}$ isn't the ground state. On XXZ and Heisenberg-Kitaev models, this term is identically zero. We will verify this from the electronic Hamiltonian in next section. The on-site quadratic contribution takes the form:

$$
H_A = -\sum_\mathbf{r}\sum_{\alpha\in\{a,b\}}2SA_\alpha^0\alpha_\mathbf{r}^\dagger\alpha_\mathbf{r} + S(\Delta A_\alpha - iA_\alpha^{xy})\alpha_\mathbf{r}^2 + S(\Delta A_\alpha + iA_\alpha^{xy})\alpha_\mathbf{r}^{\dagger 2} .
\tag{2.79}
$$

Where $\mathcal{A}'$ has been parametrized as:

$$
\mathcal{A}'_\alpha = \begin{pmatrix} A_\alpha^0 + \Delta A_\alpha & A_\alpha^{xy} \\ A_\alpha^{xy} & A_\alpha^0 - \Delta A_\alpha \end{pmatrix} .
\tag{2.80}
$$

The exchange between nearest neighbours is:

$$
H_{J1} = -\sum_\mathbf{r}\sum_p a_\mathbf{r}^\dagger b_{\mathbf{r}+\mathbf{r_p}}S(J_p^0 - id_p) + a_\mathbf{r}b_{\mathbf{r}+\mathbf{r_p}}S(\Delta J_p + iJ_p^{xy}) + h.c. .
\tag{2.81}
$$

Finally, we can write the next nearest neighbor exchange as:

$$
H_{J2} = -\frac{1}{2}\sum_\mathbf{r}\sum_{\alpha\in\{a,b\}}\sum_q S(J_q^0 - id_q)\alpha_\mathbf{r}^\dagger\alpha_{\mathbf{r}+\mathbf{r_q}} + S(\Delta J_q - iJ_q^{xy})\alpha_\mathbf{r}\alpha_{\mathbf{r}+\mathbf{r_q}} + h.c. .
\tag{2.82}
$$

All exchange matrices $\mathcal{J}_p$ and $\mathcal{J}_q$ have been parametrized as:

$$
\mathcal{J} = \begin{pmatrix} J^0 + \Delta J & J^{xy} + d \\ J^{xy} - d & J^0 - \Delta J \end{pmatrix} .
\tag{2.83}
$$

Note that we have included the possibility of an antisymmetric exchange depending on the parameter d. For example, a Dzyaloshinskii-Moriya interaction that could appears if the inversion symmetry is broken.

The next step is to take advantage of lattice's periodicity and to express each operator as a Bloch's sum.

$$\alpha_{\mathbf{r}} = \frac{1}{\sqrt{N}} \sum_{\mathbf{k}} e^{i\mathbf{k}\cdot\mathbf{r}} \alpha_{\mathbf{k}} ,$$

$$\alpha_{\mathbf{r}}^{\dagger} = \frac{1}{\sqrt{N}} \sum_{\mathbf{k}} e^{-i\mathbf{k}\cdot\mathbf{r}} \alpha_{\mathbf{k}}^{\dagger} . \tag{2.84}$$

Where N is the number of unit cells. Now, we replace the Bloch's sums on H_A, H_{J_1} and H_{J2}. After exchanging $\mathbf{r}$ and $\mathbf{k}$ summations, we use the Poisson's identity: $\sum_{\mathbf{r}} e^{i\mathbf{r}\cdot\mathbf{k}} = N\delta_{\mathbf{k},0}$, obtaining the following expressions:

$$H_A = -\sum_{\mathbf{k}} \sum_{\alpha \in \{a,b\}} -2SA_\alpha^0 \alpha_{\mathbf{k}}^{\dagger}\alpha_{\mathbf{k}} + S(\Delta A_\alpha - iA_\alpha^{xy})\alpha_{\mathbf{k}}\alpha_{-\mathbf{k}} + S(\Delta A_\alpha + iA_\alpha^{xy})\alpha_{\mathbf{k}}^{\dagger}\alpha_{-\mathbf{k}}^{\dagger} , \tag{2.85}$$

$$H_{J1} = -\sum_{\mathbf{k}} \sum_{p} Se^{-i\mathbf{k}\cdot\mathbf{r}_{\mathbf{p}}}(J_p^0 + id_p)b_{\mathbf{k}}^{\dagger}a_{\mathbf{k}} + e^{-i\mathbf{k}\cdot\mathbf{r}_{\mathbf{p}}}S(\Delta J_p - iJ_p^{xy})a_{\mathbf{k}}b_{-\mathbf{k}} + h.c. , \tag{2.86}$$

$$H_{J2} = \frac{-1}{2} \sum_{\mathbf{k}} \sum_{\alpha \in \{a,b\}} \sum_{q} e^{i\mathbf{k}\cdot\mathbf{r}_{\mathbf{q}}}\alpha_{\mathbf{k}}^{\dagger}\alpha_{\mathbf{k}} + e^{-i\mathbf{k}\cdot\mathbf{r}_{\mathbf{q}}}S(\Delta J_q - iJ_q^{xy})\alpha_{\mathbf{k}}\alpha_{\mathbf{k}}\alpha_{-\mathbf{k}} + h.c. \dots \tag{2.87}$$

Now the goal is to rewrite this bosonic Hamiltonian as a quadratic for in the vector operator $\boldsymbol{\alpha_k} = (\alpha_{\mathbf{k}} \ \beta_{\mathbf{k}} \ \alpha_{-\mathbf{k}}^{\dagger} \ \beta_{-\mathbf{k}}^{\dagger})$ as:

$$H = \frac{1}{2} \sum_{\mathbf{k}} \boldsymbol{\alpha_k^{\dagger}} \cdot H_{\mathbf{k}} \cdot \boldsymbol{\alpha_k} . \tag{2.88}$$

Where the 4×4 block $H_{\mathbf{k}}$ takes the form:

$$H_{\mathbf{k}} = \begin{pmatrix} T_{\mathbf{k}} & U_{\mathbf{k}} \\ U_{-\mathbf{k}}^* & T_{-\mathbf{k}}^* \end{pmatrix} . \tag{2.89}$$

Matrices $T_{\mathbf{k}}$ and $U_{\mathbf{k}}$ are defined as follows:

$$T_{\mathbf{k}} = -S \begin{pmatrix} 2A_a^0 + t_{a\mathbf{k}}^{(2)} & t_{\mathbf{k}}^{(1)*} \\ t_{\mathbf{k}}^{(1)} & 2A_b^0 + t_{b\mathbf{k}}^{(2)} \end{pmatrix} , \tag{2.90}$$

$$U_{\mathbf{k}} = -S \begin{pmatrix} 2(\Delta A_a + iA_a^{xy}) + u_{a\mathbf{k}}^{(2)} & u_{\mathbf{k}}^{(1)} \\ u_{-\mathbf{k}}^{(1)} & 2(\Delta A_b + iA_b^{xy}) + u_{b\mathbf{k}}^{(2)} \end{pmatrix} . \tag{2.91}$$

The functions $t_{\mathbf{k}}^{(1)}$, $t_{\alpha\mathbf{k}}^{(2)}$, $u_{\mathbf{k}}^{(1)}$ and $u_{\alpha\mathbf{k}}^{(2)}$, depend on the magnetic constants and link vectors as:

$$
\begin{aligned}
t_{\mathbf{k}}^{(1)} &= \sum_p e^{-i\mathbf{k}\cdot\mathbf{r_p}}(J_p^0 + id_p) \, , \\
t_{\alpha\mathbf{k}}^{(2)} &= \sum_q Re\{e^{-i\mathbf{k}\cdot\mathbf{r_q}}(J_{\alpha q}^0 + id_{\alpha q})\} \, , \\
u_{\mathbf{k}}^{(1)} &= \sum_p a^{i\mathbf{k}\cdot\mathbf{r_p}}(\Delta J_p + iJ_p^{xy}) \, , \\
u_{\alpha\mathbf{k}}^{(2)} &= \sum_q \cos(\mathbf{k}\cdot\mathbf{r_q})(\Delta J_{\alpha q} + iJ_{\alpha q}^{xy}) \, .
\end{aligned}
\tag{2.92}
$$

This form to express the magnonic Hamiltonian is known as the Bogoliuvov de-Gennes (BdG) Hamiltonian for bosons.

B. Diagonalization of the BdG Hamiltonian

The Bogoliuvov-de Gennes Hamiltonian $H_{\mathbf{k}}$ is diagonalized by a paraunitary matrix, instead of a unitary matrix [80]:

$$
W_{\mathbf{k}}^{\dagger} H_{\mathbf{k}} W_{\mathbf{k}} =
\begin{pmatrix}
\varepsilon_1(\mathbf{k}) & 0 & 0 & 0 \\
0 & \varepsilon_2(\mathbf{k}) & 0 & 0 \\
0 & 0 & \varepsilon_1(-\mathbf{k}) & 0 \\
0 & 0 & 0 & \varepsilon_2(-\mathbf{k})
\end{pmatrix} .
\tag{2.93}
$$

This paraunitary matrix satisfies:

$$
\begin{aligned}
W_{\mathbf{k}}^{\dagger} \boldsymbol{\sigma_3} W_{\mathbf{k}} &= \boldsymbol{\sigma_3} \, , \\
W_{\mathbf{k}} \boldsymbol{\sigma_3} W_{\mathbf{k}}^{\dagger} &= \boldsymbol{\sigma_3} \, .
\end{aligned}
\tag{2.94}
$$

Where $\boldsymbol{\sigma_3}$ is the 4×4 para-identity matrix. The idea is to find the positive eigenvalues of $\boldsymbol{\sigma_3} H_{\mathbf{k}}$. After we find the specific form of the quadratic spin Hamiltonian, on section 2.4 we'll use this technique to find the eigenvalues of the magnonic lattice. If one wants to find the eigenvectors (We are going to need them in chapter 3), we have to perform a the Colpa's algorithm [16], which consist in performing a Cholesky's decomposition of the BdG Hamiltonian as $H_{\mathbf{k}} = K_{\mathbf{k}}^{\dagger} K_{\mathbf{k}}$, with K a upper-triangular matrix. Then we define the matrix

$$
M_{\mathbf{k}} = K_{\mathbf{k}} \boldsymbol{\sigma_3} K_{\mathbf{k}}^{\dagger}
\tag{2.95}
$$

and we obtain the matrix $U_{\mathbf{k}}$ which diagonalizes $M_{\mathbf{k}}$. Finally, the paraunitary matrix that diagonalizes $H_{\mathbf{k}}$ can be written as:

$$
W_{\mathbf{k}} = K_{\mathbf{k}}^{-1} M_{\mathbf{k}}
\begin{pmatrix}
\sqrt{\varepsilon_1(\mathbf{k})} & 0 & 0 & 0 \\
0 & \sqrt{\varepsilon_2(\mathbf{k})} & 0 & 0 \\
0 & 0 & \sqrt{\varepsilon_1(-\mathbf{k})} & 0 \\
0 & 0 & 0 & \sqrt{\varepsilon_2(-\mathbf{k})}
\end{pmatrix} .
\tag{2.96}
$$

The fact that $H_{\mathbf{k}}$ is positive definite, guarantees the existence of the Cholesky's decomposition, and also the inverse $K_{\mathbf{k}}^{-1}$. Note that $H_{\mathbf{k}}$ could be not-positive definite, if $\hat{\mathbf{z}}$ is not the correct ground state. In that hypothetical case, one can say that a spin excitation around the $\hat{\mathbf{z}}$-polarized texture is unstable, and magnons have to be found as excitations around a different quantization axis.

Chapter 3

Spin waves in Heisenberg-Kitaev model

This chapter includes some calculations present in [1], with some variations in the content. This work was carried out by Esteban Aguilera, Nicolas Vidal, Alvaro Nuñez, Luis Foà, and the author of this thesis.

3.1.   Microscopical model

Recently, it has been proposed that magnetic degrees of freedom in the CrI_3 ferromagnet can be modeled using the Heisenberg-Kitaev model [92, 52]. This fact is also supported by our calculations in the last chapter, in which starting from an electronic Hamiltonian, we calculated all magnetic couplings utilizing a Green's functions method. We simplified the resulting Hamiltonian (2.69) in this chapter, in order to obtain analytical expressions for some fundamental spin constants. We neglect the next nearest neighbors hopping, and also set Γ to zero. Chromium sites form a magnetic honeycomb lattice, with a magnetic moment $S = 3/2$. The Hamiltonian consists of the usual isotropic Heisenberg exchange, plus an anisotropic contribution that come from the Kitaev model. The micromagnetic Hamiltonian takes the form:

$$H = -\sum_{<i,j>} \left(J\mathbf{S}_i \cdot \mathbf{S}_j + K S_i^\gamma S_j^\gamma \right) - \sum_i A(S_i^z)^2 \ . \tag{3.1}$$

Here, the first summation runs over nearest neighbours, and we define $S_i^\gamma \equiv \mathbf{S}_i \cdot \hat{\gamma}$, as the component of the magnetic moment in the $\hat{\gamma}$ direction. These directions depends on the link, so $\hat{\gamma}$ should be understood in (3.1) as an abbreviation of $\hat{\gamma}_{ij}$. J and K are the Heisenberg and Kitaev constants respectively. We also include an easy-axis anisotropy of magitud A.

We are considering nearest neighbours in a honeycomb lattice, so we have three kinds of links on each unit cell. On 3.1 -a, the three links $\hat{\mathbf{l}}_a$ with their respective $\hat{\gamma}_a$ directions are shown. Note that each $\hat{\gamma}_a$ points normal to the Cr_2I_2 plaquette that contains the link $\hat{\mathbf{l}}_a$. The explicit form of $\hat{\gamma}_a$ vectors in the basis xyz is shown below:

$$\hat{\gamma}_1 = \left(0, \frac{-\sqrt{2}}{\sqrt{3}}, \frac{1}{\sqrt{3}}\right) \ ,$$

$$\hat{\gamma}_2 = \left(\frac{1}{\sqrt{2}}, \frac{1}{\sqrt{6}}, \frac{1}{\sqrt{3}}\right) \ , \tag{3.2}$$

$$\hat{\gamma}_3 = \left(\frac{-1}{\sqrt{2}}, \frac{1}{\sqrt{6}}, \frac{1}{\sqrt{3}}\right) \ .$$
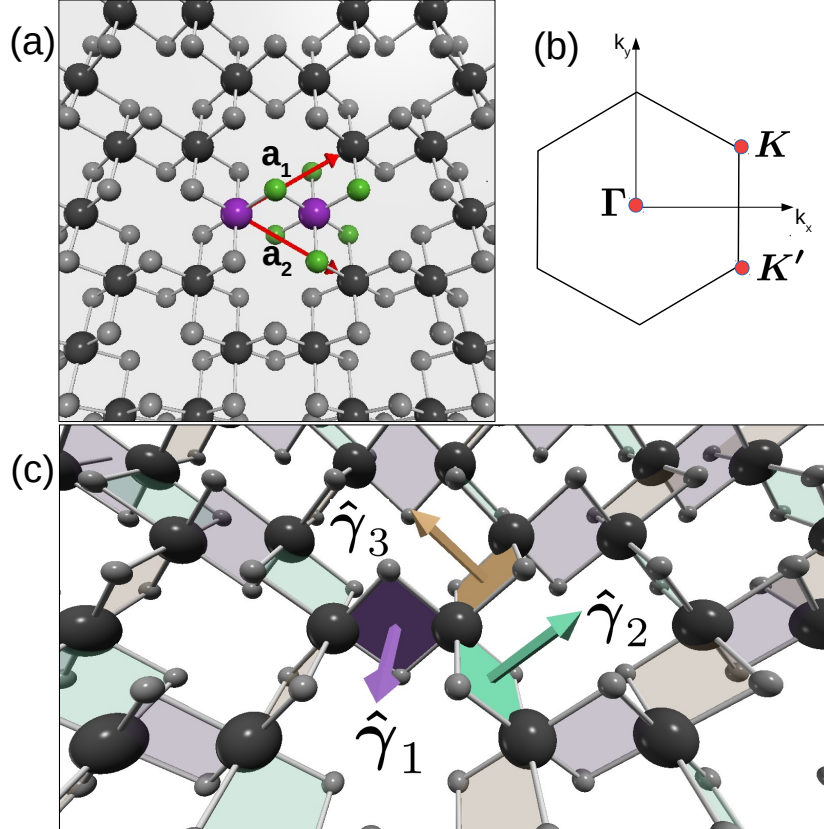
Figure 3.1: (a) Top view of CrI_3 monolayer. The atoms in the unit cell are highlighted in color, big purple spheres represent Chromium sites, and small green spheres represent Iodine sites. Lattices vectors $\mathbf{a_1} = a_0(\frac{\sqrt{3}}{2}, \frac{1}{2}, 0)$ and $\mathbf{a_2} = a_0(\frac{\sqrt{3}}{2}, -\frac{1}{2}, 0)$ were drawn with red arrows, a_0 is the lattice constant. (b) First Brillouin zone, with special symmetry points $\mathbf{\Gamma}$, $\mathbf{K}$ and $\mathbf{K'}$.(c) A view of the CrI_3 monolayer in perspective, with the plaquettes Cr_2I_2 colored according to their normal vectors $\hat{\gamma}_1, \hat{\gamma}_2$ and $\hat{\gamma}_3$. Three plaquettes in the unit cell are highlighted, and normal vectors form an orthonormal basis.

Note that $\{\hat{\gamma}_a\}$ vectors form an orthonormal basis oriented as shown in fig 3.1. Heisenberg and Kitaev's contributions to exchange can be put together using a matrix exchange $\mathcal{J}_{ij}$.

$$-\sum_{<i,j>} \left(J\mathbf{S}_i \cdot \mathbf{S}_j + KS_i^\gamma S_j^\gamma\right) = -\sum_{<i,j>} \mathbf{S}_i \cdot \mathcal{J}_{ij} \cdot \mathbf{S}_j \ . \tag{3.3}$$

Where $\mathcal{J}_{ij}$ can take, depending on the link, one of three different forms $\mathcal{J}_1$, $\mathcal{J}_2$ or $\mathcal{J}_3$. The matrix elements of $\mathcal{J}_a$ takes the form:

$$\mathcal{J}_a^{\mu\nu} = J\delta^{\mu\nu} + K\gamma_a^\mu\gamma_a^\nu. \tag{3.4}$$

Note that $\mathcal{J}_a$ remains invariant under the transformation $\hat{\boldsymbol{\gamma}}_a \to -\hat{\boldsymbol{\gamma}}_a$. So we only have to care about the direction and not the sense of $\hat{\boldsymbol{\gamma}}_a$ vectors.

3.2. Linearized equations of motion

Now, we will take into account the geometry of the lattice explicitly. A honeycomb lattice consists of a triangular Bravais lattice plus a basis of two sites A and B. We define $\mathbf{S}_A(\mathbf{r})$ and $\mathbf{S}_B(\mathbf{r})$ as the magnetic moments of the sublattices A and B at the unit cell $\mathbf{r}$. After the introduction of the exchange matrices $\mathcal{J}_a$ in the previous section, the Hamiltonian (3.1) can be written as:

$$H = -\sum_{\mathbf{r}} \mathbf{S}_A(\mathbf{r}) \cdot \left(\sum_{a=1}^{3} \mathcal{J}_a \cdot \mathbf{S}_B(\mathbf{r} - \boldsymbol{\delta}_a) \right) - \sum_{\mathbf{r}} A(S_A^z(\mathbf{r})^2 + S_B^z(\mathbf{r})^2) \ . \tag{3.5}$$

Here, δ_a are lattice vectors that connects the two unit cells involved in the link. Explicitly we have $\boldsymbol{\delta}_1 = 0$, $\boldsymbol{\delta}_2 = \mathbf{a}_2$ and $\boldsymbol{\delta}_1 = \mathbf{a}_1$. Vectors $\mathbf{a}_1$ and $\mathbf{a}_2$ are the basis vectors of the triangular latice, with components:

$$\begin{aligned} \mathbf{a}_1 =& \ a_0 \left(\frac{\sqrt{3}}{2}\hat{\mathbf{x}} + \frac{1}{2}\hat{\mathbf{y}} \right) \ , \\ \mathbf{a}_2 =& \ a_0 \left(\frac{\sqrt{3}}{2}\hat{\mathbf{x}} - \frac{1}{2}\hat{\mathbf{y}} \right) \ . \end{aligned} \tag{3.6}$$

Here, a_0 is the lattices constant of the Bravais lattice, which is related to the nearest neighbours distance between chromium sites by $d_{Cr-Cr} = \frac{a_0}{\sqrt{3}}$.

Classically, when damping is neglected, the dynamics of the magnetization is governed by the Landau-Lifchitz equation:

$$\frac{d\mathbf{S}_\alpha(\mathbf{r})}{dt} = \mathbf{S}_\alpha(\mathbf{r}) \times \frac{\delta H}{\delta \mathbf{S}_\alpha(\mathbf{r})} \ , \tag{3.7}$$

with $\alpha \in \{A, B\}$ the sub-lattice index. Here, we have redefined the time-scale, absorbing the gyroscopic constant, in such a way frequency has units of energy. The functional derivative can be calculated straight forward from (3.5), obtaining

$$\frac{\delta H}{\delta \mathbf{S}_A(\mathbf{r})} = -\sum_{a=1}^{3} \mathcal{J}_a \cdot \mathbf{S}_B(\mathbf{r} - \boldsymbol{\delta}_a) - 2AS_A^z(\mathbf{r})\hat{\mathbf{z}} \ , \tag{3.8}$$

$$\frac{\delta H}{\delta \mathbf{S}_B(\mathbf{r})} = -\sum_{a=1}^{3} \mathcal{J}_a \cdot \mathbf{S}_A(\mathbf{r} - \boldsymbol{\delta}_a) - 2AS_B^z(\mathbf{r})\hat{\mathbf{z}} \ . \tag{3.9}$$

We are only concerned about small perturbations around the ground state, which we assume to have all magnetic moments pointing on $\hat{\mathbf{z}}$. Magnetic moments can be written up to linear

order in S_x and S_y:

$$\mathbf{S}_\alpha(\mathbf{r}) \approx \begin{pmatrix} S_\alpha^x(\mathbf{r}) \\ S_\alpha^y(\mathbf{r}) \\ S \end{pmatrix} \tag{3.10}$$

and then we replace in equation (3.5) by components, for each sub-lattice. Let's start with lattice A, x component of (3.5) is

$$\frac{dS_A^x(\mathbf{r})}{dt} = -S_A^y(\mathbf{r}) \sum_{a=1}^{3} \mathcal{J}_a^{zl} S_B^l(\mathbf{r} - \boldsymbol{\delta}_a) + S \sum_{a=1}^{3} \mathcal{J}_a^{yl} S_B^l(\mathbf{r} - \boldsymbol{\delta}_a) - 2ASS_A^y(\mathbf{r})$$

$$\approx -S_A^y(\mathbf{r})S\left(\sum_{a=1}^{3} \mathcal{J}_a^{zz} + 2A\right) + \sum_{a=1}^{3} S\left(\mathcal{J}_a^{yx} S_B^x(\mathbf{r} - \boldsymbol{\delta}_a) + \mathcal{J}_a^{yy} S_B^y(\mathbf{r} - \boldsymbol{\delta}_a)\right) + \sum_{a=1}^{3} S\mathcal{J}_a^{yz} . \tag{3.11}$$

In a similar way, y-component of (3.5) for lattice A takes the form

$$\frac{dS_A^y(\mathbf{r})}{dt} = -S \sum_{a=1}^{3} \mathcal{J}_a^{xl} S_B^l(\mathbf{r} - \boldsymbol{\delta}_a) + S_A^x(\mathbf{r}) \sum_{a=1}^{3} \mathcal{J}_a^{zl} S_B^l(\mathbf{r} - \boldsymbol{\delta}_a) + 2ASS_A^x(\mathbf{r})$$

$$\approx S_A^x(\mathbf{r})S(\sum_{a=1}^{3} \mathcal{J}_a^{zz} + 2A) - S \sum_{a=1}^{3} \left(\mathcal{J}_a^{xx} S_B^x(\mathbf{r} - \boldsymbol{\delta}_a) + \mathcal{J}_a^{xy} S_B^y(\mathbf{t} - \boldsymbol{\delta}_a)\right) - S \sum_{a=1}^{3} \mathcal{J}_a^{xz} . \tag{3.12}$$

In the last two equations, we used Einstein notation in repeated indices. It is going to be useful to calculate the matrix elements of the sum of all matrices $\mathcal{J}_a$:

$$\left[\sum_{a=1}^{3} \mathcal{J}_a\right]^{\mu\nu} = 3J\delta^{\mu\nu} + K \sum_{a=1}^{3} \gamma_a^\mu \gamma_a^\nu . \tag{3.13}$$

Provided the completeness of the orthonormal basis $\{\hat{\boldsymbol{\gamma}}_a\}$, the sum of the three dyads in the last expression is proportional to the identity matrix, and we get

$$\left[\sum_{a=1}^{3} \mathcal{J}_a\right]^{\mu\nu} = (3J + K)\delta^{\mu\nu} . \tag{3.14}$$

Using this, it is simple to note that

$$\sum_{a=1}^{3} \mathcal{J}_a^{xz} = \sum_{a=1}^{3} \mathcal{J}_a^{yz} = 0. \tag{3.15}$$

Now we define $\psi_\alpha(\mathbf{r}) \equiv S_\alpha^x(\mathbf{r}) + iS_\alpha^y(\mathbf{r})$. Note that $\psi_\alpha(\mathbf{r})$ and $\psi_\alpha^*(\mathbf{r})$ are the classical analogues to the spin ladder operators $\hat{S}^+$ and $\hat{S}^-$. Now we combine the x and y components of the linearized equation of motion, by calculating $\frac{d\psi_\alpha}{dt}$ from (3.11) and (3.12).

$$i\frac{d\psi_A(\mathbf{r})}{dt} = -\psi_A(\mathbf{r})(3J + K + 2A)S + \sum_{a=1}^{3} \psi_B(\mathbf{r} - \boldsymbol{\delta}_a)\frac{S(\mathcal{J}_a^{xx} + \mathcal{J}_a^{yy})}{2} \tag{3.16}$$

$$+ \sum_{a=1}^{3} \psi_B^*(\mathbf{r} - \boldsymbol{\delta_a})\frac{S(\mathcal{J}_a^{xx} - \mathcal{J}_a^{yy} + i(\mathcal{J}_a^{xy} + \mathcal{J}_a^{yx}))}{2} \ . \tag{3.17}$$

In analogous way, we can calculate the equation of motion for $\psi_B(\mathbf{r})$:

$$i\frac{d\psi_B(\mathbf{r})}{dt} = -\psi_B(\mathbf{r})(3J + K + 2A)S + \sum_{a=1}^{3} \psi_A(\mathbf{r} - \boldsymbol{\delta}_a)\frac{S(\mathcal{J}_a^{xx} + \mathcal{J}_a^{yy})}{2} \tag{3.18}$$

$$+ \sum_{a=1}^{3} \psi_A^*(\mathbf{r} - \boldsymbol{\delta_a})\frac{S(\mathcal{J}_a^{xx} - \mathcal{J}_a^{yy} + i(\mathcal{J}_a^{xy} + \mathcal{J}_a^{yx}))}{2} \ . \tag{3.19}$$

We define the following quantities:

$$\begin{aligned}
C &\equiv S(3J + K + 2A) \ , \\
\alpha_a &\equiv -S\frac{\mathcal{J}_a^{xx} + \mathcal{J}_a^{yy}}{2} \ , \\
\beta_r^a &\equiv -S\frac{\mathcal{J}_a^{xx} + \mathcal{J}_a^{yy}}{2} \ , \\
\beta_i^a &\equiv -S\mathcal{J}_a^{xy} \ , \\
\beta_a &\equiv \beta_r^a + i\beta_r^a \ .
\end{aligned} \tag{3.20}$$

Equations of motion can now be wrote as

$$i\frac{d\psi_A(\mathbf{r})}{dt} = -C\psi_A(\mathbf{r}) - \sum_{a=1}^{3} \alpha_a\psi_B(\mathbf{r} - \boldsymbol{\delta}_a) - \sum_{a=1}^{3} \beta_a\psi_B^*(\mathbf{r} - \boldsymbol{\delta}_a) \ , \tag{3.21}$$

$$i\frac{d\psi_B(\mathbf{r})}{dt} = -C\psi_B(\mathbf{r}) - \sum_{a=1}^{3} \alpha_a\psi_A(\mathbf{r} - \boldsymbol{\delta}_a) - \sum_{a=1}^{3} \beta_a\psi_A^*(\mathbf{r} - \boldsymbol{\delta}_a) \ . \tag{3.22}$$

Since our system is periodic, we make use of Bloch's theorem, and by writing each wave function as a superposition of Bloch waves in the first Brillouin Zone (1BZ).

$$\psi_\alpha(\mathbf{r}) = \frac{1}{\sqrt{N}} \sum_{\mathbf{k}} e^{-i\mathbf{k}\cdot\mathbf{r}} \psi_{\alpha\mathbf{k}} \ , \tag{3.23}$$

with N being the number of units cells in the system. We replace the Bloch's sum in the equations of motion, and after some manipulation we get:

$$i\frac{d\psi_{A\mathbf{k}}}{dt} = -C\psi_{A\mathbf{k}} - \left(\sum_{a=1}^{3} \alpha_a e^{i\mathbf{k}\cdot\boldsymbol{\delta}_a}\right)\psi_{B\mathbf{k}} - \left(\sum_{a=1}^{3} \beta_a e^{i\mathbf{k}\cdot\boldsymbol{\delta}_a}\right)\psi_{B-\mathbf{k}}^* \ , \tag{3.24}$$

$$i\frac{d\psi_{B\mathbf{k}}}{dt} = -C\psi_{B\mathbf{k}} - \left(\sum_{a=1}^{3}\alpha_a e^{i\mathbf{k}\cdot\boldsymbol{\delta}_a}\right)\psi_{A\mathbf{k}} - \left(\sum_{a=1}^{3}\beta_a e^{i\mathbf{k}\cdot\boldsymbol{\delta}_a}\right)\psi_{A-\mathbf{k}}^* . \tag{3.25}$$

Defining

$$\alpha_{\mathbf{k}} = \sum_{a=1}^{3}\alpha_a e^{i\mathbf{k}\cdot\boldsymbol{\delta}_a} \tag{3.26}$$

and

$$\beta_{\mathbf{k}} = \sum_{a=1}^{3}\beta_a e^{i\mathbf{k}\cdot\boldsymbol{\delta}_a} , \tag{3.27}$$

the equations of motion takes the simpler form:

$$i\frac{d\psi_{A\mathbf{k}}}{dt} = -C\psi_{A\mathbf{k}} - \alpha_{\mathbf{k}}\psi_{B\mathbf{k}} - \beta_{\mathbf{k}}\psi_{B-\mathbf{k}}^* \tag{3.28}$$

$$i\frac{d\psi_{B\mathbf{k}}}{dt} = -C\psi_{B\mathbf{k}} - \alpha_{\mathbf{k}}\psi_{A\mathbf{k}} - \beta_{\mathbf{k}}\psi_{A-\mathbf{k}}^* . \tag{3.29}$$

Note that the frequency matrix is not block-diagonal in $\mathbf{k}$-basis. It mixes $\mathbf{k}$ and $-\mathbf{k}$ wave vectors. This feature appears because of the presence of the anomalous term proportional to β, which in turn, is proportional to the Kitaev's constant K, as we can see in definitions (3.27) and (3.20). To solve these differential equations as an eigenvalue problem, we need to diagonalize a 4×4 matrix that mixes $\psi_{\mathbf{k}}$ with $\psi_{-\mathbf{k}}^*$. We conjugate and change $\mathbf{k}$ to $-\mathbf{k}$ in (3.28) and (3.29) to obtain:

$$i\frac{d\psi_{A-\mathbf{k}}^*}{dt} = C\psi_{A-\mathbf{k}}^* + \alpha_{-\mathbf{k}}^*\psi_{B-\mathbf{k}}^* + \beta_{-\mathbf{k}}^*\psi_{B\mathbf{k}} , \tag{3.30}$$

$$i\frac{d\psi_{B-\mathbf{k}}^*}{dt} = C\psi_{B-\mathbf{k}}^* + \alpha_{-\mathbf{k}}^*\psi_{A-\mathbf{k}}^* + \beta_{-\mathbf{k}}^*\psi_{A\mathbf{k}} . \tag{3.31}$$

Now we put together equations (3.28), (3.29), (3.30) and (3.31) in matricial form:

$$i\frac{d}{dt}\boldsymbol{\Psi}_{\boldsymbol{k}} = -\hat{\Omega}_{\mathbf{k}}\boldsymbol{\Psi}_{\boldsymbol{k}} , \tag{3.32}$$

where we have defined $\boldsymbol{\Psi}_{\boldsymbol{k}}$ as

$$\boldsymbol{\Psi}_{\boldsymbol{k}} = \begin{pmatrix} \psi_{A\mathbf{k}} \\ \psi_{B\mathbf{k}} \\ \psi_{A-\mathbf{k}}^* \\ \psi_{B-\mathbf{k}}^* \end{pmatrix} . \tag{3.33}$$

The elements of the frequency matrix $\hat{\Omega}_{\mathbf{k}}$ are given by

$$
\hat{\Omega}_{\mathbf{k}} = \begin{pmatrix} C & \alpha_{\mathbf{k}} & 0 & \beta_{\mathbf{k}} \\ \alpha_{\mathbf{k}}^* & C & \beta_{-\mathbf{k}} & 0 \\ 0 & -\beta_{-\mathbf{k}}^* & -C & -\alpha_{\mathbf{k}} \\ -\beta_{\mathbf{k}}^* & 0 & -\alpha_{\mathbf{k}}^* & -C \end{pmatrix} .
$$

(3.34)

3.3. Spin wave's spectrum

The characteristic polynomial of $\hat{\Omega}_{\mathbf{k}}$ gives us a bi-quadratic equation that can be solved exactly. After substitution of definitions of α and β, we obtain

$$
\omega_\pm^2(\mathbf{k}) = \frac{\omega_0^2}{9}(f(\mathbf{k}) \pm \sqrt{g(\mathbf{k})}),
$$

(3.35)

with $\omega_0 = 3J + K$ fixing the frequency scale. Here we have defined functions $f(\mathbf{k}) = f_0(\mathbf{k}) + f_\rho(\mathbf{k}) + f_{\mathcal{K}}(\mathbf{k})$ and $g(\mathbf{k}) = g_0(\mathbf{k}) + g_{\mathcal{A}}(\mathbf{k}) + g_{\mathcal{K}}(\mathbf{k})$, in such a way functions $f_{\mathcal{A},\mathcal{K}}(\mathbf{k})$ and $g_{\mathcal{A},\mathcal{K}}(\mathbf{k})$ were zero when $\mathcal{A}, \mathcal{K} = 0$, respectively.

$$
f_0(\mathbf{k}) = 2\left(2\cos\left(\frac{\sqrt{3}k_x a_0}{2}\right)\cos\left(\frac{k_y a_0}{2}\right) + \cos(k_y a_0) + 6\right),
$$

(3.36)

$$
f_{\mathcal{A}}(\mathbf{k}) = 9\mathcal{A}(2 + \mathcal{A}),
$$

(3.37)

$$
f_{\mathcal{K}}(\mathbf{k}) = \mathcal{K}^2\left(2\cos\left(\frac{\sqrt{3}k_x a_0}{2}\right)\cos\left(\frac{k_y a_0}{2}\right) + \cos(k_y a_0) - 3\right),
$$

(3.38)

and

$$
g_0(\mathbf{k}) = 36\left(4\cos\left(\frac{\sqrt{3}k_x a_0}{2}\right)\cos\left(\frac{k_y a_0}{2}\right) + 2\cos(k_y a_0) + 3\right),
$$

(3.39)

$$
g_{\mathcal{A}}(\mathbf{k}) = 36\mathcal{A}(\mathcal{A} + 2)\left(4\cos\left(\frac{\sqrt{3}k_x a_0}{2}\right)\cos\left(\frac{k_y a_0}{2}\right) + 2\cos(k_y a_0) + 3\right),
$$

(3.40)

$$
\begin{aligned}
g_{\mathcal{K}}(\mathbf{k}) = \frac{3}{2}\mathcal{K}^2 \Bigg(& 2\cos\left(\sqrt{3}k_x a_0\right)\left(-\left(\mathcal{K}^2 - 4\right)\cos(k_y a_0) + \mathcal{K}^2 + 2\right) \\
& - 2\left(\mathcal{K}^2 + 2\right)\left(8\cos\left(\frac{\sqrt{3}k_x a_0}{2}\right)\sin^2\left(\frac{k_y a_0}{2}\right)\cos\left(\frac{k_y a_0}{2}\right) + \cos(k_y a_0)\right) \\
& + \left(\mathcal{K}^2 - 4\right)\left(-\cos(2k_y a_0)\right) + 3\left(\mathcal{K}^2 - 4\right)\Bigg).
\end{aligned}
$$

(3.41)

Here, $\mathcal{K}$ is an adimensional parameter defined by

$$\mathcal{K} = \frac{K}{3J + K} \ , \tag{3.42}$$

which is bounded between $0 < \mathcal{A} < 1$, when $J, K > 0$. In this sense, $\mathcal{K}$ represents the relative strength of the Kitaev constant. Similarly, $\mathcal{A}$ is defined as:

$$\mathcal{A} = \frac{2A}{3J + K} \ , \tag{3.43}$$

It represents the relative magnitude of the anisotropy constant. The spectrum is shown in fig 3.2. The blue line is the spectrum with $\mathcal{K} = 0$, and the red line corresponds to $\mathcal{K} = 2/5$. Note the gap at $\boldsymbol{\Gamma}$ point with magnitude $\Delta_{\boldsymbol{\Gamma}}$, which is the same for two different values of $\mathcal{K}$, so it seems to be independent of Kitaev's interaction. Also, we have a gap at $\boldsymbol{K}$ point of magnitude $\Delta_{\boldsymbol{K}}$, which appears when the Kitaev's interaction is turned on. Now we are going to analyze the spectrum in the vicinity of these special symmetry points in order to give an exact expression for the gaps and other important quantities.
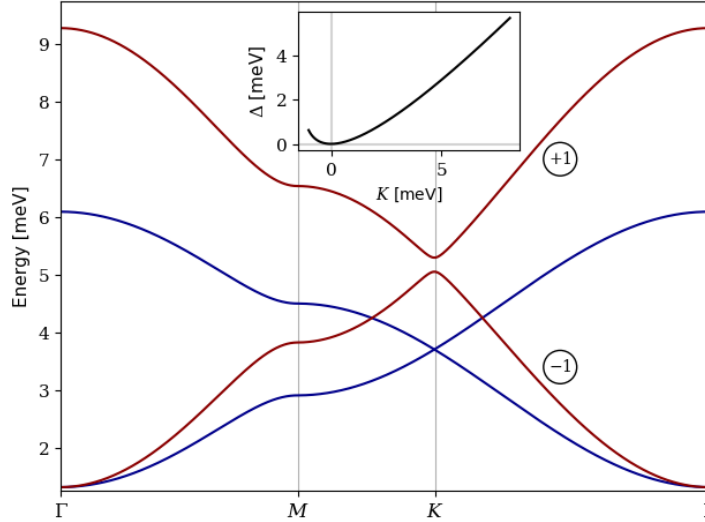
Figure 3.2: Energy spectrum of magnons within the first Brillouin zone. The blue line corresponds to the case $J = 0.53$, $A = 0.44$ and $K = 0$. It can be see that there is no gap at the $\boldsymbol{K}$-point. There is a gap at the Γ point that arises from the anisotropy contribution[49]. On the other hand, the inclusion of the Kitaev interaction, $K = 2J$ displayed in the red line, displays a gap opening at the $\boldsymbol{K}$-point revealing a non-trivial topology. The circles next to each bands correspond to the associated Chern numbers. These are calculated according to [80]. The $\boldsymbol{K}$-point gap is calculated as a function of the Kitaev interaction strength in the inset. This plot was made by Esteban Aguilera in [1].

3.3.1. Long wavelength limit

If we focus on waves near of $\mathbf{\Gamma}$ point, in the limit $\mathbf{k} \to 0$, we can expand functions $f(\mathbf{k})$ and $g(\mathbf{k})$ in powers of k_x, k_y up to quadratic order:

$$f(\mathbf{k}) \approx 18 + 9\mathcal{A}(2 + \mathcal{A}) - \frac{3}{2}(2 + \mathcal{K}^2)a_0^2 a_0^2 |\mathbf{k}|^2 \ , \tag{3.44}$$

$$g(\mathbf{k}) \approx 27 \left(12(\mathcal{A} + 1)^2 - |\mathbf{k}|^2 \left(2(\mathcal{A} + 1)^2 + \mathcal{K}^2 \right) \right) \ . \tag{3.45}$$

Then we replace on (3.35) and expand the square root. Positives frequencies are expressed as follows:

$$\omega_+(\mathbf{k}) = 2\omega_0 + A - \omega_0 a_0^2 \left(\frac{1 + 2\mathcal{A} + \mathcal{K}^2}{24(1 + \mathcal{A})} \right) |\mathbf{k}|^2 \ ,$$

$$\omega_-(\mathbf{k}) = A + \omega_0 a_0^2 \left(\frac{1 + 2\mathcal{A} - \mathcal{K}^2}{24(1 + \mathcal{A})} \right) |\mathbf{k}|^2 \ . \tag{3.46}$$

In the lower band we identify the usual structure $\omega = \Delta_{\mathbf{\Gamma}} + \rho_{\mathbf{\Gamma}} k^2$, where $\Delta_{\mathbf{\Gamma}} = 2AS$ and $\rho_{\mathbf{\Gamma}} = \epsilon_0 a_0^2 \left(\frac{2 + 2\mathcal{A} - \mathcal{K}^2}{24(1 + \mathcal{A})} \right)$. $\Delta_{\mathbf{\Gamma}}$ correspond to the minimal energy necessary to create a magnon. It turns out to be a fundamental quantity and can be accessed experimentally. It lies between 1 and 9 meV [43] while ab-initio calculations locate it in the range of 1 meV [17]. $\rho_{\mathbf{\Gamma}}$ is the effective low energy spin stiffness. It is an estimate of how hard it is to introduce a smooth texture in the magnetization field.

The behavior of the top band at $\mathbf{\Gamma}$ point has the form:

$$\epsilon_+(\mathbf{k}) = 2\epsilon_0 + \Delta_{\mathbf{\Gamma}} - \rho'_{\mathbf{\Gamma}} |\mathbf{k}|^2 \ . \tag{3.47}$$

As can be observed that the bandwidth, defined as the energy difference $\epsilon_+ - \epsilon_-$ at $\mathbf{\Gamma}$ point, is given by $2\epsilon_0 = 2S(3J + K)$.

3.3.2. Vicinity of K and K'

Next to $\boldsymbol{K}$ and $\boldsymbol{K'}$ points, we can obtain the following effective Hamiltonians

$$\mathbf{H}_{\mathbf{K}^{(\prime)}}(\mathbf{q}) = \begin{pmatrix} \mathbf{T_q} & \mathbf{U}^{(\prime)} \\ \mathbf{U}^{(\prime)\dagger} & \mathbf{T_q} \end{pmatrix} \ , \tag{3.48}$$

where matrices $\mathbf{T_q}$, $\mathbf{U}$ and $\mathbf{U}'$ are defined as:

$$T_{\mathbf{q}} = \epsilon_0 \begin{pmatrix} 1 + \mathcal{A} & i\kappa \\ -i\kappa & 1 + \mathcal{A} \end{pmatrix} \ ,$$

$$\mathbf{U} = \begin{pmatrix} 0 & 0 \\ K & 0 \end{pmatrix}$$

and $\mathbf{U}' = \mathbf{U}^\dagger$. Here we have defined $\mathbf{q} = \mathbf{k} - \mathbf{K}^{(\prime)}$ and $\kappa = a_0(q_x + iq_y)/(2\sqrt{3})$, with a_0 being the lattice constant. In the definition of $\mathbf{U}$ we have dropped linear terms in $\mathbf{q}$ under the

assumtion of small Kitaev parameter. Energies around $\mathbf{K}$ and $\mathbf{K}'$ take the form:

$$\epsilon^{\pm}(\mathbf{q}) = E_{\mathbf{K}} \pm \frac{\Delta_{\mathbf{K}}}{2} \pm \rho_{\mathbf{K}}^{\pm}|\mathbf{q}|^2 \; ,$$

with $E_{\mathbf{K}} = \frac{\epsilon_0}{2}(1 + \mathcal{A} + \sqrt{(1 + \mathcal{A})^2 - \mathcal{K}^2})$ and $\Delta_{\mathbf{K}} = \epsilon_0(1 + \mathcal{A} - \sqrt{(1 + \mathcal{A})^2 - \mathcal{K}^2})$. All those features are in agreement with [17] which can be used to adjust our parameters. We find: $J \sim 0.53$meV, $K \sim 4.07$meV and $A \sim 0.44$meV, in same range as [52].

3.4. Topological magnons in the Heisenberg-Kitaev Model.

In a quantum mechanical perspective, a particle-like excitation of the magnetization field around the ground state is called a magnon. To obtain a magnonic Hamiltonian for the Heisenberg-Kitaev model introduced in (3.1), we have to perform a Holstein-Primakoff's transformation [38]:

$$\begin{aligned}
S_{i\mu}^{(x)} &= \sqrt{\frac{S}{2}}\left(\psi_{i\mu}^{\dagger} + \psi_{i\mu}\right) \; , \\
S_{i\mu}^{(y)} &= i\sqrt{\frac{S}{2}}\left(\psi_{i\mu}^{\dagger} - \psi_{i\mu}\right) \; , \\
S_{i\mu}^{(z)} &= S - \psi_{i\mu}^{\dagger}\psi_{i\mu} \; ,
\end{aligned} \tag{3.49}$$

where $\mu \in \{A, B\}$ indexes the two lattices conforming the bipartite honeycomb array of Cr atoms. $\psi_{i\mu}$ and $\psi_{i\mu}^{\dagger}$ are the ladder spin operators at the unit cell i, in the sublattice μ. When replaced in the Hamiltonian and reduced to quadratic terms, we obtain a Hamiltonian in terms of $\mathbf{\Psi}_{\boldsymbol{k}} = (\psi_{A\mathbf{k}}, \psi_{B\mathbf{k}}, \psi_{A-\mathbf{k}}^{\dagger}, \psi_{B-\mathbf{k}}^{\dagger})^t$, in the form $\mathcal{H} = \frac{1}{2}\sum_{\mathbf{k}} \mathbf{\Psi}_{\boldsymbol{k}}^{\dagger} \mathbf{H}_k \mathbf{\Psi}_{\boldsymbol{k}}$. Each block $H_{\mathbf{k}}$ is:

$$H_{\mathbf{k}} = \begin{pmatrix} C & \alpha_{\mathbf{k}} & 0 & \beta_{\mathbf{k}} \\ \alpha_{\mathbf{k}}^* & C & \beta_{-\mathbf{k}} & 0 \\ 0 & \beta_{-\mathbf{k}}^* & C & \alpha_{\mathbf{k}} \\ \beta_{\mathbf{k}}^* & 0 & \alpha_{\mathbf{k}}^* & C \end{pmatrix} \; . \tag{3.50}$$

Note the similitude between (3.50) and the frequency matrix obtained previously (3.34). They are related by $\Omega_{\mathbf{k}} = \sigma_3 H_{\mathbf{k}}$, where σ_3 is the paraidentity matrix defined by:

$$\sigma_3 = \begin{pmatrix} 1 & 0 & 0 & 0 \\ 0 & 1 & 0 & 0 \\ 0 & 0 & -1 & 0 \\ 0 & 0 & 0 & -1 \end{pmatrix} \; . \tag{3.51}$$

The origin of this similitud is that operators $\psi_{i\mu}$ and $\psi_{i\mu}^{\dagger}$ satisfies the bosonic commutation relation, and to obtain the spectrum of a bosonic quadratic Hamiltonian of the form $\hat{H} = \frac{1}{2}\sum_{\mathbf{k}} \mathbf{\Psi}_{\boldsymbol{k}}^{\dagger} H_{\mathbf{k}} \mathbf{\Psi}_{\boldsymbol{k}}$ we should para-diagonalize each block $H_{\mathbf{k}}$ by means of a Bogoulivov's transformation, wich for multiple dimensions turns out to be the Colpa's algorithm [16]. To obtain the eigenvalues we have to diagonalize the matrix $\sigma_3 H_{\mathbf{k}}$, and conserve the positive energies. Then the eigenvalues of (3.50) coincide with those obtained in the classical formulation (3.35), and all analytical results of the last section remain valid in this formalism.

3.4.1. Berry's Curvature and Chern's number

The band structure found by these methods reveals a non-trivial topological structure, which is present both in the full model (3.1) and even in the minimal model of equation (3.48). The above is in agreement with the results of [44] for similar geometrical construction. Chern's numbers of each band, calculated according to [80], are displayed next to each band in figure 3.2. The Chern number of the jth energy band is given by:

$$C_j = i \frac{\epsilon_{\mu\nu}}{2\pi} \int_{BZ} \mathrm{d}^2k \ Tr\left((1 - P_j) \left(\partial_{k_\mu} P_j \right) \left(\partial_{k_\nu} P_j \right) \right) \ . \tag{3.52}$$

The integrand of the Chern number is called the Berry curvature, $\mathbf{\Omega}_{\mathbf{k}}^j$, and P_j are the projection operators, which are defined as: $P_j = T_{\mathbf{k}} \Gamma_j \sigma_3 T_{\mathbf{k}}^\dagger \sigma_3$. Where we have that $T_{\mathbf{k}}$ is the transformation matrix obtained by Bogoliubov's algorithm[16], σ_3 is the paraunitary matrix and Γ_j is a $(2N, 2N)$ matrix where every element is 0 except for the j-th diagonal component, where it has a value of 1.

We are going to focus on the minimal model (3.48), which is a good approximation for the Hamiltonian at $\mathbf{K}$ and $\mathbf{K'}$ points when the Kitaev's parameter K is small. Our motivation to focus on this limit is to show how the inclusion of a non zero Kitaev's parameter, is enough to generate a non-trivial topological structure.

Berry's curvature turns out to be nonzero only in the vicinity of $\mathbf{K}$ and $\mathbf{K'}$ points, and it takes the same values on both of them. This happens because Berry's curvature is the remainder of the singularity in the parameter space that occurs at $K = 0$, when the gap is closed. Defining $\mathbf{q} = \mathbf{k} - \mathbf{K}^{(\prime)}$, we found that Berry's curvature has no angular dependence(with respect to $\mathbf{K}^{(\prime)}$), and it takes the form:

$$\mathbf{\Omega}^\pm(\mathbf{q}) = \pm\Omega_0(q) \ . \tag{3.53}$$

With $q = |\mathbf{q}|$ and the $\pm$ label indicating the upper and lower band, respectively. $\Omega_0(q)$ is shown on 3.3. Since we are focusing on an effective model around $\mathbf{K}^{(\prime)}$, the integral of the Chern's number has to be performed summing the integrands of both points and then integrating to infinity. We found:

$$C^\pm = \pm\frac{1}{2\pi} \int_0^{2\pi} \int_0^\infty 2\Omega_0(q) q dq d\phi = \pm 2 \int_0^\infty \Omega_0(q) q dq = \pm 1 \ . \tag{3.54}$$

It is also important to note that the value of the Chern's numbers does not revert its sign when K passes from a positive value to a negative one. Therefore an interface between samples with different signs of K would not host topological states as there is no change in the Chern number between the regions. This is because a chirality is already fixed when we chose the $\mathbf{z}$ as the quantization axis. To change the sign of the Chern's number, we must change and revert the quantization axis. From this fact, we expect magnetic domain walls on CrI$_3$ to act effectively as topologically protected waveguides.

The starting Hamiltonian (3.50) displays complete time-reversal symmetry. It is only

after its spontaneous breaking that we can expect a non-time-reversal symmetric (TRS) Hamiltonian for the spin-wave branch of excitations. It can be shown that performing TRS is equivalent to change the quantization axis from z to $-z$. Performing Holstein-Primakoff's transformation around the reversed axis leads to the complex conjugation of the coefficients of equation 3.50, followed by a $\mathbf{k} \to -\mathbf{k}$ transformation. The Hamiltonian (3.50) will be invariant under TRS if the coefficient β_a is real. When Kitaev's parameter K is turned on, we obtain $\mathcal{J}_a^{xy} \neq 0$. The above makes β_a complex, so TRS is broken in our Hamiltonian. It is important to emphasize that the TRS breaking takes place through an anomalous $A - B$ nearest-neighbor coupling in contrast to the normal $A - A$ next-nearest-neighbors proposed by [74, 14, 47].
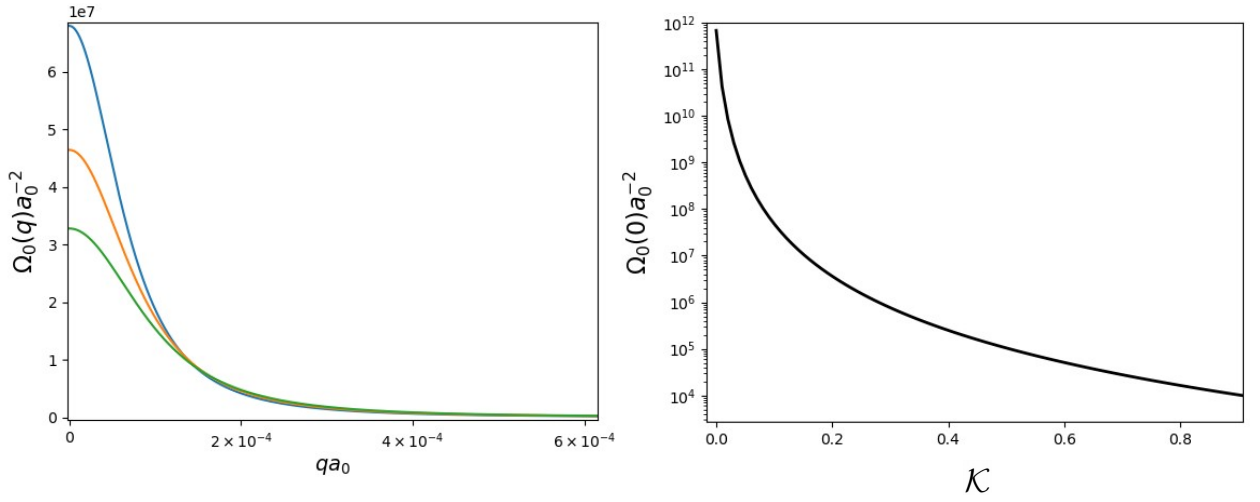

Figure 3.3: Left panel: Berry curvature in the vicinity of $\boldsymbol{K}$ point. Blue, orange and green lines correspond to $\mathcal{K} = 0.1$, $\mathcal{K} = 0.11$ and $\mathcal{K} = 0.12$ respectively. Right panel: Peak in the Berry's curvature $\Omega_0(q = 0)$ for different values of $\mathcal{K}$. Both plots were calculated with $\mathcal{A} = 0$.

Part II

Micromagnetic Simulations in 2D surfaces with DMI

Chapter 4

Stability of atomic-sized skyrmions in antiferromagnetic bilayers.

This chapter is a literal transcription of the published article [41]. This work was done by the author of this thesis, together with Álvaro S. Nuñez.

4.1. Abstract

We perform a stability analysis of an isolated atomic-sized antiferromagnetic skyrmion (AFM-Sk), formed on the superior layer of a magnetic bilayer. The coupling between both square lattices acts as an effective staggered magnetic field that stabilizes the AFM-Sk and reduces its radius. A suitable anisotropy constant of the bottom layer material keeps it close to the homogeneous AFM state. We compare the energy of the AFM-Sk with the energy of the AFM ground state. In addition, an estimation of the energy barrier that protects the skyrmion from being destabilized is provided and its value determined to be in the order of ~ 300K. The remarkable reduction in the skyrmion radius towards atomic size and avoiding an external magnetic field are key points in order to increase our ability to manipulate AFM-Sk on skyrmionic devices. Our calculations provide an insight into novel ways to create and manipulate AFM-Sk at the atomic scale.

4.2. Introduction

Antiferromagnetic (AFM) spintronics has turned into a major theme in the recent spintronic developments.[4] Due to natural advantages over other systems and configurations, AFM spintronics systems stand as natural environments for both, novel physical phenomena and technological applications[28]. Just as their ferromagnetic counterparts, antiferromagnetic order parameter get coupled with spin-polarized currents[89, 90, 34]. This opens the possibility for displaying a great number of different spintronic effects in the context of AFM materials. Several of these effects are already implemented [29, 30, 32]. Among the advantages that AFM systems presents over ferromagnetic ones, to play a role as landscapes for spintronics, we can mention the following: their stray field are radically smaller, their time scale is within the terahertz range [91] and it offers natural integration pathways with standard ferromagnets[60, 21]. In addition to these advantages, it is worth to mention that AFM

properties are spread over several materials, even in semiconductors at room temperature [59]. This opens the possibility of hybrid systems that could display both spintronics and electronic features.

The above interest leads to the natural query whether it is possible for antiferromagnetic systems to display skyrmion-like textures in their order parameter. This feature would provide a further analogy with ferromagnetic systems while endowing AFM materials with a very promising metastructure that can be driven and controlled in order to perform information processing and storage. Magnetic skyrmions have been at the spotlight of research in magnetism for already a decade. The major point of attraction is based upon the fact that they are regarded as candidates to play a starring role in the future of data storage. They are expected to lead to novel spintronic devices like skyrmion racetrack memories [24], skyrmion-based logic gates [97], synaptic devices[40], among others. Magnetic skyrmions are spin textures with pseudo-particle properties [68], they can be defined as a solution of the Dzyaloshinskii theory which is localized, axisymmetric, and has fixed rotation sense [78]. Therefore magnetic skyrmions are specially suited for the role of information holders. Their properties seem tailor-made for such a role:(i) They are localized and nanometrically sized. (ii) They are robust to perturbations, (iii) They display current-driven motion at ultra-low current densities. skyrmions also exhibit a variety of topological phenomena associated with their swirling spin texture. An iconic example is the topological Hall effect induced by the emergent magnetic field of skyrmions on conduction electrons[95]. skyrmions can appear in two dimensional systems with very simple requirements such as exchange interaction. The stability of their features, such as the skyrmion radius, however, depends on a much subtler energy balance that involves an interplay between the exchange and other interactions such as Dzyalonshinskii-Moriya[23, 66] or four-spin interaction[35]. The Dzyaloshinskyy-Moriya interaction (DMI), present in non-centrosymmetric magnets with a high spin-orbit coupling, has been largely studied in this regard. The competition between Heisenberg exchange and DMI leads to the stabilization of ferromagnetic skyrmions at a fixed radius. It has been studied that an external applied magnetic field normal to the surface can reduce the skyrmion radius [88, 12]. This has important advantages in the design of skyrmionic devices, since it increases the memory density. However it would be convenient to avoid the need of an external magnetic field for two reasons: (i) The experimental difficulty of producing a nanometric-localized magnetic field of the desired magnitude. (ii) An external magnetic field could undesirably affect other parts of the device.

Antiferromagnetic skyrmions have been predicted, and their properties studied theoretically, in a series of papers [9, 27, 96, 6, 77]. The important features of AFM-Sky are [42]: (i) AFM-Sk current-driven motion is at least two orders of magnitude faster than the ferromagnetic case. (ii) AFM-Sk doesn't exhibit the Magnus force, which implies that AFM skyrmions move following directly along the line of the current. These characteristics make AFM skyrmions better candidates for using them on the magnetic transmission of information.

The aim of this article is to expand the range of existing theoretical possibilities to stabilize antiferromagnetic skyrmions with radius at the atomic limit. We will see that this can be achieved without relying on the application of an external magnetic field. When properly controlled by electric currents, these atomic-sized skyrmions could be used as a system of information storage.

4.3. Theoretical model

The system at the core of the following developments is an antiferromagnetic lattice grown on top of a heavy metal. It is well known that this set-up gives rise to a magnetic system whose degrees of freedom are affected by an interfacial Dzyalonshinskii-Moriya interaction. This kind of arrangement has been predicted to stabilize skyrmions in the antiferromagnetic layer. For reasons that will become clear later we will work with a bilayer system [27]. Being deposited on a metallic surface the bilayer will be described by different parameters characterizing the couplings within each layer and, importantly, by an interlayer exchange coupling. This coupling influences the stability of the magnetic textures and affects their main properties. Our starting point is a magnetic bilayer model formed by two square lattices, say *top* and *bot*. Each layer represents an AFM system, with an exchange, anisotropy, and DM interactions. In this way, each one of them can display a skyrmionic texture with dimensions determined as functions of the ratios of the energy contributions.

Let $\mathbf{s_A^a}$ be the unitary dimensionless magnetic moment on the site A (with respect to the plane), and the layer a.
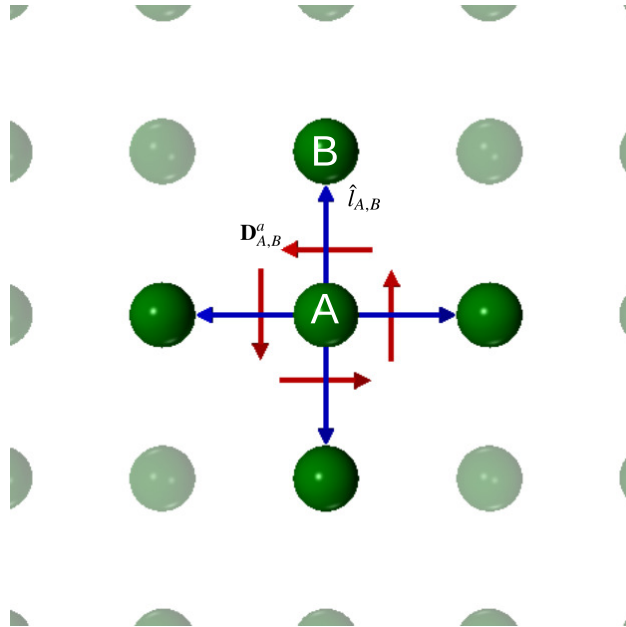

Figure 4.1: A display of the square lattice, with the sites being represented by the green spheres. The central site A and his first neighbors are highlighted with the link vectors on blue. Over each link, the interfacial DMI vector is showed on red color. Here the anisotropy axis is pointing out of the page.

The energy that describes the dynamics of the classical spins in the bilayer system is:

$$H = H_{top} + H_{bot} + \sum_A J_{inter} \mathbf{s}_A^{top} \cdot \mathbf{s}_A^{bot} \tag{4.1}$$

The sum is over first neighbors of different layers. The exchange constant between layers is J_{inter}. H_{bot} and H_{top} are the Hamiltonians of the spins on each layer independently, and have the form:

$$H_a = J_a \sum_{\langle A,B \rangle} \mathbf{s}_A^a \cdot \mathbf{s}_B^a + \sum_{\langle A,B \rangle} \mathbf{D}_{A,B}^a \cdot (\mathbf{s}_A^a \times \mathbf{s}_B^a) - \kappa_a \sum_A (\mathbf{s}_\mathbf{A}^\mathbf{a} \cdot \hat{z})^2 \qquad (4.2)$$

Here $\hat{z}$ is the unitary vector that is normal to the superior layer, pointing out. The first term is the Heisenberg exchange, with the same exchange constant $J = J_{top} = J_{bot}$ on both layers. The sign is chosen in order to keep J being positive for antiferromagnetic coupling. The second term is the interfacial Dzyaloshinskii Moriya interaction, the vector $\mathbf{D}_{A,B}^a = D_a \hat{z} \times \hat{l}_{A,B}$, is on the layer plane, with $\hat{l}_{A,B}$ being the unitary link vector between the sites A and B (see fig. 4.1).

We also introduce a term of easy axis anisotropy, proportional to κ_a, on the respective layer.

The temporal evolution of each spin is given by the Landau-Lifshitz-Gilbert equation [54]:

$$\frac{d\mathbf{s}_\mathbf{A}}{dt} = -\gamma \mathbf{s}_\mathbf{A} \times \mathbf{h}_\mathbf{A}^\mathbf{eff} + \alpha \mathbf{s}_\mathbf{A} \times \frac{d\mathbf{s}_\mathbf{A}}{dt} \qquad (4.3)$$

The parameters of the Hamiltonian, appear on the effective field $\mathbf{h}_\mathbf{A}^\mathbf{eff} = \frac{\delta H}{\delta \mathbf{s}_\mathbf{A}}$. The gyromagnetic ratio is $\gamma = \frac{g_e \mu_B}{\hbar}$, while the dimensionless Gilbert damping coefficient is denoted by α. We use a homemade simulation programmed on Python 3.5 to solve numerically the LLG equation (using $\alpha = 0.01$) by an implicit method that conserves the spin norm. The system is temporarily evolved until the maximum spin-torque $\frac{d\mathbf{s}_A^a}{dt}$ decreases below a fixed bound at $10^{-6}\omega_0$, with $\omega_0 = \frac{\gamma J}{\mu_B}$ being the antiferromagnetic resonance frequency, on the THz range. This value typically coincides with energy variations of the order of $10^{-8} J\omega_0$ per site. In this article, the values of all the parameters of the Hamiltonian are expressed in terms of the exchange constant $J = 3$ meV, and the skyrmion radius is expressed in units of the lattice constant $a = 0.5$ nm. As a first approach, the anisotropy constants are fixed to be $\kappa_{top} = \kappa_{bot} = 0.2$, then we study the effects of varying the bottom one. A large anisotropy constant κ_{bot} keeps the bottom layer near of the homogeneous Neel-like state, while the superior layer feels an alternated effective magnetic field, due to the antiferromagnetic coupling between layers. Replacing every other spin by its negative we reach an equivalent description based on a ferromagnetic layer with the opposite DM coupling. Under this duality, the effects of exchange with the bottom layer take the form of an external magnetic field that can aid the stabilization of a skyrmion and affects its radius [88, 12]. We expect that an AFM skyrmion could be stabilized on the superior layer. The role of the coupling between layers is the same than that of the staggered magnetic field pointing out-of-plane[27], and due to the previous analogy, it is the same than a homogeneous field pointing upward on a ferromagnetic skyrmion [94, 33]. Altough it has been demostrated [7] that it is possible to stabilize isolated ferromagnetic skyrmions in absense of an external magnetic field, the effective field here introduced by the interlayer coupling is desirable, as we will show later, in order to reduce the skyrmion radius and expand the range of parameters in which isolated skyrmions are stable. Keeping κ_{bot}, κ_{top}, and J fixed, we vary the antiferromagnetic coupling between layers J_{inter}, and the DMI constant $D = D_{top}$ in two scenarios: (i) $D_{bot} = D_{top}$.; (ii) $D_{bot} = 2D_{top}$. The second one has the intention of giving a more realistic approach, in which the bilayer system is placed over a heavy metallic layer with high spin orbit coupling. In this case the Dzyaloshinskii-Moriya energy of the bottom layer should be larger than the top one. Situation (ii) mimics the gradual decrease of the chiral energy density, as described phenomenologically by Bogdanov in a multilayered system [8].

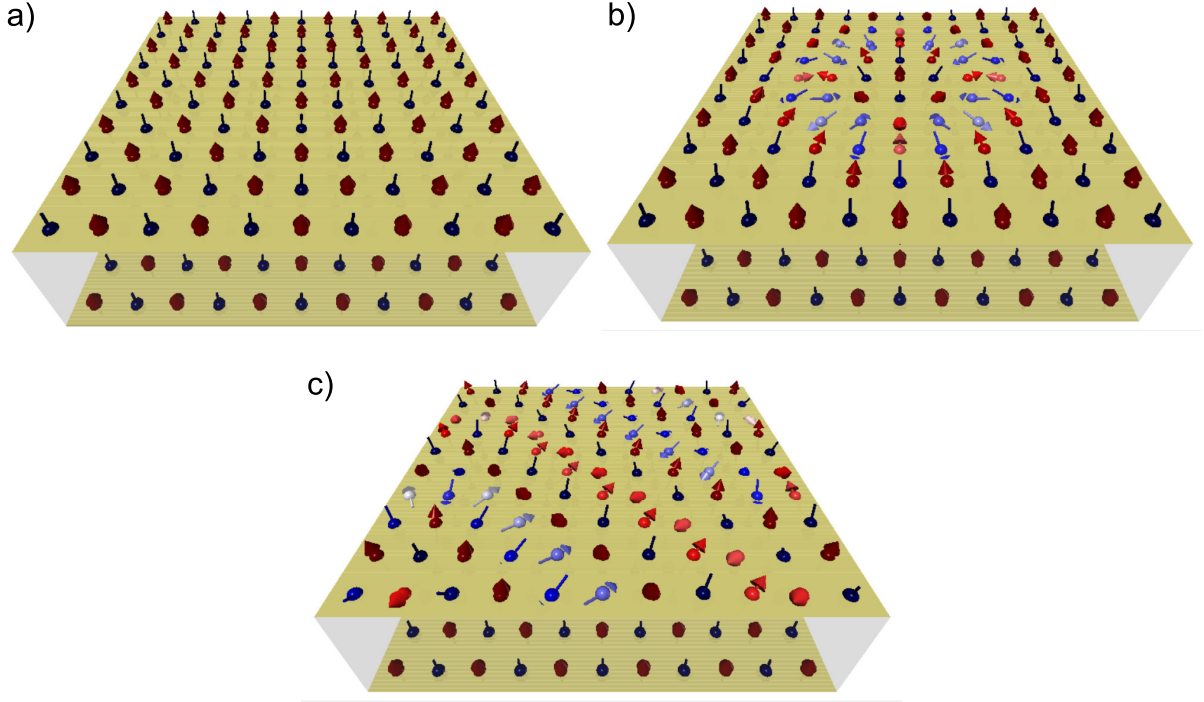## 4.4.   Stability and main features of the isolated skyrmion

Figure 4.2: While the inferior layer keeps near the homogeneous Neel state, the superior layer exhibits different equilibrium spin textures: a) AFM state. b) Isolated antiferromagnetic Neel-like skyrmion of radius $R_{Sk} = 3a$. c) AFM Helicoidal order. (See the animations on supplementary material).

We study the time evolution of our system starting from an initial configuration of an isolated Neel-like AFM skyrmion on the superior layer and a homogeneous Neel-like state in the bottom layer. The initial skyrmion has axial symmetry while its radial profile is determined by minimizing the energy of the spin texture. We evolve the magnetic system by solving the LLG equation. The system has 50×50 sites and periodical edge conditions. Three equilibriums can be reached from this initial configuration, as indicated the figure 4.2-a: (i) Antiferromagnetic ground state (AFM); (ii) Isolated AFM skyrmion (Sk); (iii) AFM helicoidal order (H). All these three configurations were observed in the top layer, while the bottom one remained only slightly disturbed from the Neel AFM ground state. In some cases, the inferior AFM state was destabilized as a result of the coupling with the superior layer, and in these cases we say that the bottom layer is unstable (U).

By varying the exchange coupling between layers J_{inter}, and the DM interaction $D = D_{top}$. We construct a stability diagram for the isolated AFM-skyrmion, in the cases $D_{bot} = D_{top}$ and $D_{bot} = 2D_{top}$. We calculated the energy difference between the AFM-Sk and the Neel state on the stability zone (see fig 4.3-a and fig 4.4-a). On the green-colored zone called AFM, the initial skyrmion is annihilated to a Neel-like state (fig 4.2-a). The coupling between layers, acting as a magnetic field, favours the AFM enviroment that surrounds the AFM-sk, and contributes to reducing the radius of the skyrmion until it collapses. This process is analogous

to the high field skyrmion instability, which has been described in the ferromagnetic context [7, 53].

On the central zone *Sk*, the isolated skyrmion is stabilized with a fixed radius (see fig 4.2-b). The color map shows the energy difference between the skyrmion and the AFM states. The white dotted line represents the parameters for which the AFM-Sk has the same energy than the AFM state. Below the white doted line, the ground state of the whole system is an homogeneous Neel-like texture on both layers. It can be seen that in a large fraction of the stability zone, the skyrmion has more energy than the AFM ground state. This means that the isolated AFM-skyrmion on the top layer is a meta-stable equilibrium and there should be an energy barrier that protects the skyrmion from its demise. Above the white doted line, but still inside the stability zone, the skymion has less energy that its surroundings and it should be expected of the skyrmion crystal on the top layer to be the ground state. However if the skyrmions don't nucleate easily, which occurs for example in materials with enhanced coercivity [53], the skyrmion is still isolated as a meta-stable equilibrium. As we approach to the frontier of the stability zone, by increasing D or decreasing J_{inter}, another instability appears. On the blue-colored zone labeled by *H*, the skyrmion is ellipitically deformed until an AFM-helicoidal state is obtained (see fig 4.2-c). The mechanism of this elliptical instability is analogous to the instability of isolated ferromagnetic skyrmions at low magnetic fields[7, 53]. Inside the blue-colored zone, the ground state on the top layer, could be the AFM-helicoidal state or the AFM-sk crystal, depending on the value of D and J_{inter}. A complete characterization of these ground states is beyond the scope of this article, and we settle by studying the isolated AFM skyrmion as a meta-stable equilibrium. We suggest the reader review the supplementary material and see the animations of the three scenarios previously described. Finally, on the orange-colored zone *U*, because of the coupling between layers J_{inter}, the bottom one is unable to stay on the AFM state. This breaks down the staggered magnetic field that feels the top layer.

The fact that the bottom layer is able to support the skyrmion on the top layer, is mainly because of the high anisotropy constant κ_{bot}. It is natural to ask how much this anisotropy could be reduced so that the bottom layer stays, stably, close to a Neel-like state. The winding number of the Neel vector has to be zero on the bottom layer in order to obtain an staggered magnetic field on the top layer, and it is in this sense that we characterize the stability of the bottom later. We fix $D = D_{top} = 0.5$ (red dotted line on figs 4.3-a and 4.4-a), and by varying k_{bot} and J_{inter} we construct the stability diagrams on figures 4.3-b and 4.4-b. For high k_{bot} the frontiers of the stability zone converge with those determined by the limit in which the bottom layer is fixed to the AFM ground state. As κ_{bot} is reduced the range of stability expands. This implies that the deformation of the spin texture on the inferior layer favors the skyrmion stability. However, if k_{bot} continues to be reduced, the bottom layer is destabilized and no skyrmion texture is formed on the top layer.

To evaluate the energy barrier that protects the AFM-Sk from its annihilation can be a rather intricate problem and we are better served by an heuristic approach used in the assessment quantum nucleation of the ferromagnetic skyrmion[18]. Within this approach we use an analytic interpolation between the isolated AFM-skyrmion and the AFM ground-state, which was proposed by [18] for a ferromagnetic system:

$$w_{\mathbf{r}} = \frac{\lambda v_{\mathbf{r}}^{Sk}}{1 + \lambda u_{\mathbf{r}}^{Sk}} \qquad \bar{w}_{\mathbf{r}} = \frac{\bar{\lambda} \bar{v}_{\mathbf{r}}^{Sk}}{1 + \bar{\lambda} \bar{u}_{\mathbf{r}}^{Sk}} \qquad (4.4)$$
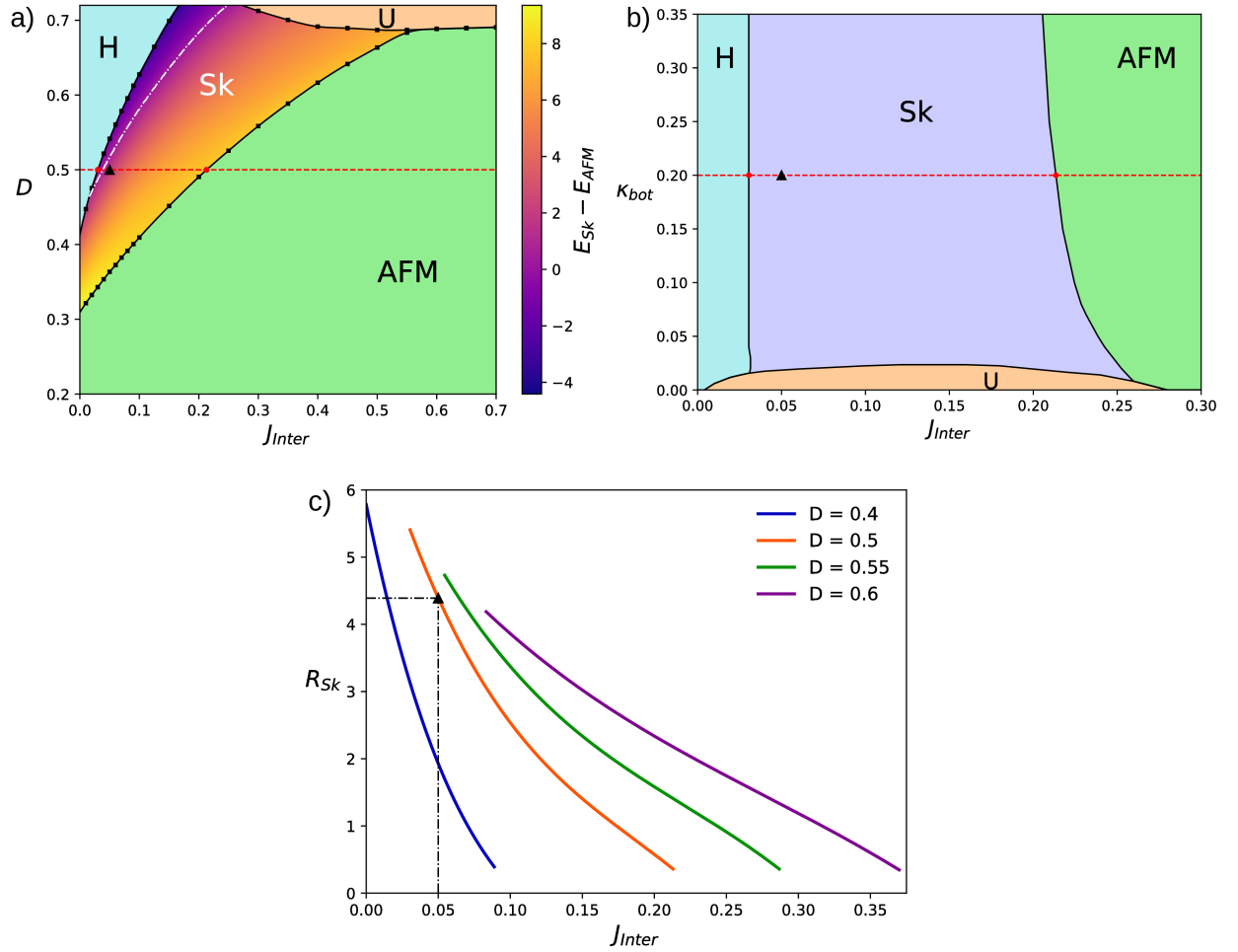
Figure 4.3: Case $D_{bottom} = D_{top}$: **a)** Stability diagram for an isolated AFM skyrmion on the superior layer $D = D_{top}$ and J_{inter} have units of J. $\kappa_{bot} = \kappa_{top}$. **b)** Stability diagram for an isolated AFM skyrmion on the superior layer, κ_{bot} and J_{inter} have units of J, $\kappa_{top} = 0.2J$ is fixed and marked on the dotted red horizontal line, $D = 0.5J$ is marked on the dotted red horizontal line on (b). **c)** skyrmion radius R_{Sk} in units of the lattice constant a, as a function of J_{inter} in units of J. Different curves correspond to different values of fixed D. A black triangle on a), b) and c) is highlighting the point $D = 0.5J$ and $J_{inter} = 0.05J$.

Here $v_{\mathbf{r}}^{Sk}$ and $u_{\mathbf{r}}^{Sk}$ are the spinor coordinates on the site $\mathbf{r}$ of the antiferromagnetic skyrmion. These coordinates are the outcome of our LLG evolution. $w_{\mathbf{r}} = v_{\mathbf{r}}/u_{\mathbf{r}}$ is the well known stereographic projection. When the parameter λ tends to ∞, $w_{\mathbf{r}}$ represents an isolated skyrmion. When λ is reduced from infinity to zero, the spin texture changes, first reducing the skyrmion radius and then annihilating the skyrmion into the ferromagnetic homogeneous state. The analogy previously mentioned between FM spin texture and the staggered AFM spin texture ensures that this reasoning for the FM skyrmion is connected with the AFM skyrmion that we are stabilizing. By taking the energy difference between the AFM-Sk and the maximum energy on the interpolation, we estimated the activation energy required to disarm an AFM-skyrmion into the AFM ground state (see fig. 4.5). For the values depicted,
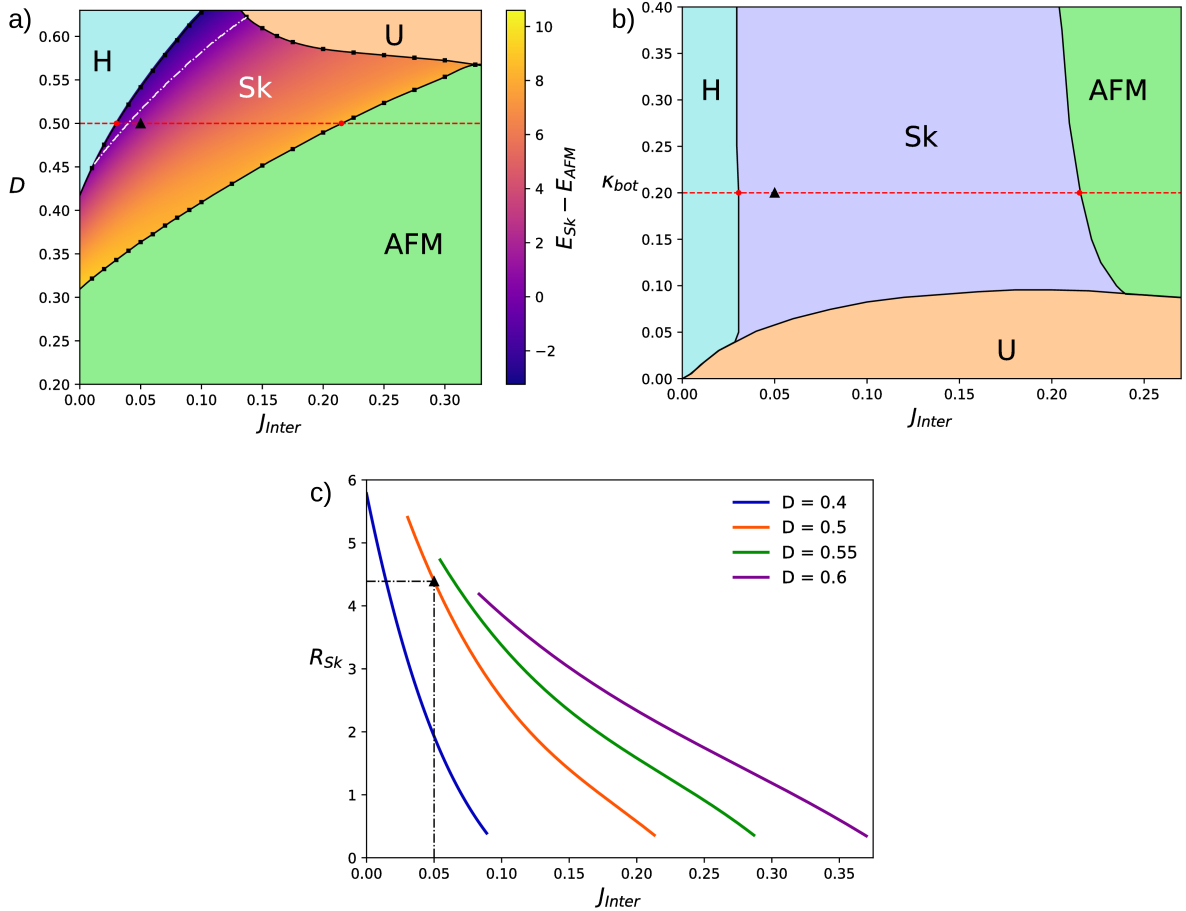
Figure 4.4: Case $D_{bottom} = 2D_{top}$: **a)** Stability diagram for an isolated AFM skyrmion on the superior layer $D = D_{top}$ and J_{inter} have units of J. $\kappa_{bot} = \kappa_{top}$. **b)** Stability diagram for an isolated AFM skyrmion on the superior layer, κ_{bot} and J_{inter} have units of J, $\kappa_{top} = 0.2J$ is fixed and marked on the dotted red horizontal line, $D = 0.5J$ is marked on the dotted red horizontal line on (b). **c)** skyrmion radius R_{Sk} in units of the lattice constant a, as a function of J_{inter} in units of J. Different curves correspond to different values of fixed D. The black triangle on a), b) and c) is highlighting the point $D = 0.5J$ and $J_{inter} = 0.05J$.

the energy barrier may be in the order of 300 K.

The analytic interpolation [18] was used because it qualitatively captured the destabilizing mechanism of the AFM-Sk. It begins to reduce its radius and finally twists the central spin, changing the winding number of the Neel vector.

It is observed that as we approach the border of the stability zone, the potential barrier drops towards zero. On the other hand, the skyrmion radius (see figs 4.1-c and 4.4-c), defined by the circle with $\mathbf{s}_z = 0$, decreases until a terminal size, smaller than the lattice constant a. This suggests that there is a minimum radius for the AFM skyrmion, like the one already suggested [81] for ferromagnetic skyrmions. Under a certain radius, the skyrmion inevitably relaxes to the AFM state, because there is no energy barrier to protects it.

Finally, comparing the behavior of the system in cases (i) $D_{bot} = D_{top}$ and (ii) $D_{bot} = 2D_{top}$

(fig 4.3 and fig 4.4 respectively), it is noted that both are qualitatively equivalent. Both cases show the same phases and annihilation mechanisms. The main difference is that in the most realistic case (ii), the bottom layer is more prone to destabilization (U).
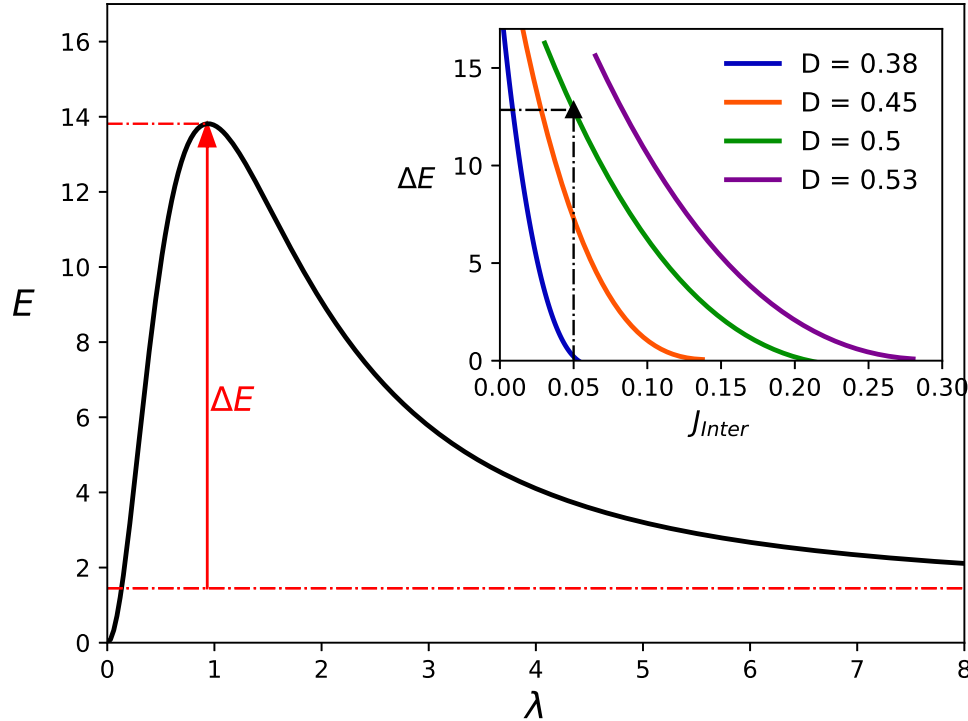

Figure 4.5: Energy of the spin texture that the analytical interpolation forms, as a function of the parameter λ. $\lambda = 0$ represents the AFM ground state, while $\lambda = \infty$ corresponds to an isolated antiferromagnetic skyrmion stabilized with $D_{top} = 0.5J$ and $J_{inter} = 0.05J$ (Case (ii) $D_{bot} = 2D_{top}$). On the upper right subplot, the energy barrier ΔE is plotted for different values of D, as a function of the interlayer coupling J_{inter}.

4.5. Final remarks

We study the stability of isolated atomic sized skyrmions formed in antiferromagnetic bilayers. When one of the layers is held fixed by, say, a slightly higher anisotropy field, it aides the stability of the skyrmion in the other layer. The antiferromagnetic exchange coupling between layers acts as an effective-staggered magnetic field on the superior one[27]. This effective field allows the stabilization of atomic-sized antiferromagnetic skyrmions. This is analogous to when a homogeneous magnetic field is added to a skyrmion and causes a reduction in its size.

We start from an initial condition with an AFM-Sk on the top layer, and we evolve the system to find an equilibrium. Repeating this process, varying Dzyaloshinsky-Moriya inter-

action and the coupling between layers, we construct a stability diagram in which the energy difference between AFM-ground state and AFM skyrmion was computed. We observed that on a great region of this stability diagram, the AFM ground state is less energetic than the AFM-Sk. This implies that there is an energy barrier that protects the AFM-skyrmion, making it robust to perturbations. We estimated this activation energy needed to destabilize an AFM-Sk, and it turned out to be in the order of 300 K. As expected, the energy barrier drops to zero near of the frontier of the stability zone. This result means that some of the skyrmions studied could be stable even at room temperature. The small size of the stabilized AFM-Sk, like those found by [69], would allow improving the information density on skyrmion-based memory devices. Also, there is no need to apply an external magnetic field to stabilize atomic-sized-AFM-Sk. The idea of avoiding the application of an external magnetic field, and still being able to reduce the AFM-Sk radius is important due to two reasons. (i) The effective magnetic field induced by exchange coupling reaches values that are two orders over those external magnetic fields obtained experimentally. Also, it would be extremely difficult module the field to be staggered, in order to stabilize an AFM-Sk. (ii) An external magnetic field could have negative consequences on other components of a magnetic device. Proper control of skyrmion-like textures has been at the spotlight of the research in magnetism (both theoretically and experimentally) during the past decade, leading up to several proposals that implement memory storage and logic manipulation. Among those, antiferromagnetic implementations stand out as promising candidates, and the achievement of atomic-sized skyrmions would provide a significant progress in the field.

Acknowledgements

Chapter 5

Ultrafast domain wall propagation due to the interfacial Dzyaloshinskii-Moriya interaction

This chaptewr is a literal transcription of the published article [61]. This work was done by Daniela Mancilla, Álvaro S. Núñez, Sebastian Allende, and the author of this thesis. The main contribution of the author on this work was the realization of a micro-magnetic simulation that provided the proper ansatz for the analytical calculations shown here.

5.1.   Abstract

It is shown that the interplay between curvature and interfacial Dzyalonshinsky- Moriya interaction (DMI) is a pathway to ultrafast domain wall dynamics. In this work, we theoretically study the effect that interfacial DMI has on the average velocity of the domain wall in thin ferromagnetic nanotubes grew around a core composed of heavy atoms. Our main result shows that the domain wall average velocity is greater than usual by delaying the Walker breakdown instability. This velocity is similar to the average velocities obtained in ferrimagnetic systems, i.e., we find average velocities of the order of 103 m/s. The remarkable velocities achieved through this configuration could prove greatly convenient for developing spintronic devices.

5.2.   Introduction.

The exploration of the dynamical properties of curved ferromagnetic systems has become a fertile ground for potential applications in spintronic devices such as memory devices and microwave technologies, among others. [79, 84, 37]. The reason to focus on these structures is that the curvature induces anisotropies and chiral effects that arise from the lack of collinearity of the spin moments. Effects such as the effective anisotropy and antisymmetric exchange, i.e., Dzyaloshinskii-Moriya-like interaction emerge in a phenomenological sense regardless of the details of the underlying crystal structure[79, 84, 26]. In this sense, the curvature becomes a new element in the toolkit of magnetization control and related phenomena. It has been shown, that curvature effects can affect the magnetic properties of the structures, and

69

alter dramatically the basic picture of texture dynamics, such as spin waves [73], domain walls motion[93, 36], and skyrmions related phenomena[13, 48].

Among the several ferromagnetic curved nanostructures, nanotubes stand out over the other nanostructures due of the ultrafast domain wall motion against the usual domain wall motion given in magnetic strip[50, 36]. Also, nanotubes present a chiral symmetry breaking in the domain wall motion [72]. These properties allow nanotubes to be an excellent candidate for use in various magnetic devices.[36].

Ferromagnetic nanotubes present a Dzyaloshinskii-Moriya-like interaction that arises from their curvature this induces a chiral symmetry breaking in the domain wall dynamics. An interesting competition is expected if the system is engineered to display an actual DMI as well. This type of exchange has been included in systems ultrathin magnetic films for the study of the domain wall motion[86]. By example, Thiaville et al. observed domain wall motion with large velocities under large fields at stationary conditions[86]. In nanotubes, Goussev et al. studied bulk Dzyaloshinskii-Moriya domain walls in magnetic nanotubes with non-radial component in the magnetization[31]. They observed a dependence of the domain wall velocity with the chirality and the DMI. In this context, to fabricate ferromagnetic nanotubes with DMI could be possible by using Atomic Layer Deposition (ALD)[3, 15]. Therefore, a theoretical study of domain wall motion in ferromagnetic nanotubes with interfacial DMI must be necessary if we want to understand the physics of these systems.

In this work, we studied the effect that DMI has on the average velocity of the domain wall in thin ferromagnetic nanotubes. To obtain the average velocity, first, we obtained an energy expression for the continuous interfacial Dzyaloshinskii-Moriya interaction. Second, we required to obtain the static and dynamics phase diagrams for the domain wall shape if we want to calculate the domain wall average velocity. Our main result shows that the domain wall average velocity is similar to the average velocities obtained in ferrimagnetic systems, i.e., we find average velocities of the order of 10^3 m/s.

5.3.   Ferromagnetic nanutube

The system under consideration can be modeled as a ferromagnetic nanotube with an outer radius R and an inner radius βR, where $0 < \beta < 1$. The length L of the nanotube is much longer than the radius. We consider that the ferromagnetic (FM) nanotube surrounds a heavy metal (HM) material core, which leads to an interfacial Dzyaloshinskii-Moriya interaction is present at the interface between these two materials. The magnetization of the FM nanotube can be written as $\mathbf{M} = M_s\mathbf{\Omega}$, where M_s is the saturation magnetization and $\mathbf{\Omega}$ is an unit vector. Then, the magnetic energy functional, $\mathcal{E}$, of this system is given by

$$\mathcal{E}[\mathbf{\Omega}] = \int dV [A(\mathbf{\nabla\Omega})^2 - K(\hat{\mathbf{z}} \cdot \mathbf{\Omega})^2 + \frac{\mu_0 M_s^2}{2}(\hat{\boldsymbol{\rho}} \cdot \mathbf{\Omega})^2]$$

$$+ \int dV D\hat{\boldsymbol{\rho}} \cdot [\mathbf{\Omega}(\mathbf{\nabla} \cdot \mathbf{\Omega}) - (\mathbf{\Omega} \cdot \mathbf{\nabla})\mathbf{\Omega}], \tag{5.1}$$

where the right terms are the exchange, the anisotropy, the demagnetizing, and the Dzyaloshinskii-Moriya energies, respectively. A is the stiffness constant, K is the anisotropy constant, μ_0 is the vacuum permeability, and D is the interfacial Dzyaloshinskii-Moriya parameter. . In particular, $D = 2d/a2$, where d is related to the Dzyaloshinskii-Moriya vector and a is the lattice constant. We remark that the functional form of the Dzyalonshinskii-Moriya interaction

differs from the one expected in a plane geometry. This difference arises from the curvature of the system as can be appreciated in the supplementary material. The unit vector $\boldsymbol{\Omega}$, in cylindrical coordinates, can be written as

$$
\begin{aligned}
\Omega_\rho &= \sin\Theta(\rho,\phi,z)\cos\Psi(\rho,\phi,z),\\
\Omega_\phi &= \sin\Theta(\rho,\phi,z)\sin\Psi(\rho,\phi,z),\\
\Omega_z &= \cos\Theta(\rho,\phi,z).
\end{aligned}
\tag{5.2}
$$

If we consider that the tube thickness is small ($\beta \sim 1$), the magnetization is like a vortex domain wall (DW) independent of the radial coordinate [51], that is,

$$
\begin{aligned}
\Theta(\rho,\phi,z) &= \Theta(z),\\
\Psi(\rho,\phi,z) &= \pi/2 + p,
\end{aligned}
\tag{5.3}
$$

where p measures the radial component of the magnetization. Additionally, this parameter can describe the two magnetization chiralities, i.e., when $p = 0$ or $p = \pi$, there is a counter-clockwise or clockwise vortex DW, respectively. After replacing Eqs. (5.3) in Eqs. (5.2) and (5.1), the magnetic energy is

$$
\mathcal{E} = sA\int dz\left[(\partial_z\Theta)^2 + \frac{\sin^2(\Theta)}{\lambda_p^2} - \frac{1}{W^2} + \frac{(\partial_z\Theta)}{d}\sin(p)\right],
\tag{5.4}
$$

where $s = \pi R^2(1-\beta^2)$ is the cross section area, $d = A/(2D)$, $W^2 = A/K$, and

$$
\lambda_p = \left[\frac{2\log(1/\beta)}{R^2(1-\beta^2)} + \frac{\sin^2(p)}{\ell^2} + \frac{1}{dR(1+\beta)} + \frac{1}{W^2}\right]^{-1/2},
\tag{5.5}
$$

with $\ell = \sqrt{2A/\mu_0 M_s^2}$ the exchange length, and λ_p is related to the domain wall length.

In our calculations, we consider a ferromagnetic material of cobalt with $\beta = 0.95$, $A = 1.3\times10^{-11}$ J/m, $K = 410$ J/m^3, $M_s = 1400\times10^3$ A/m, and $\ell = 3.25$ nm.

5.3.1. Static vortex domain wall.

In this section, we study the magnetization equilibrium in the ferromagnetic nanotube. The equilibrium magnetic state satisfies $\partial_z\Theta = -\chi\sin\Theta/\lambda_p$, with χ taking values ±1. The solution is

$$
\cos\Theta(z) = \tanh\left(\chi\frac{z-z_0}{\lambda_p}\right),
\tag{5.6}
$$

where z_0 is the position of the domain wall center. We have that $\chi = +1$ means tail-to-tail magnetizations and $\chi = -1$ means head-to-head magnetizations, see Fig. 5.1.

The total energy of the domain wall is, up to an overall constant

$$
\mathcal{E} = sA\left[\frac{4}{\lambda_p} - \chi\frac{\pi\sin(p)}{d}\right].
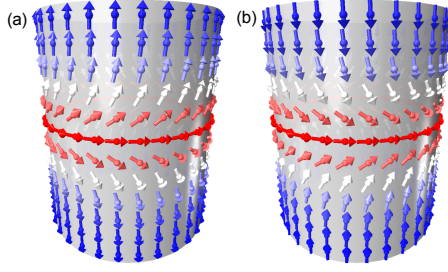\tag{5.7}
$$

Figure 5.1: Magnetization for (a) $\chi = +1$ and (b) $\chi = -1$ considering $p = 0$ and neglecting Dzyaloshinskii-Moriya interaction.

Its optimal values for p are $p_1 = \pi/2$, $p_2 = -\pi/2$,

$$p_3 = \chi \arcsin \left(\frac{\ell}{\lambda_0} \sqrt{\frac{1}{(16d^2/(\pi^2\ell^2) - 1)}} \right), \tag{5.8}$$

or

$$p_4 = \chi \left[\pi - \arcsin \left(\frac{\ell}{\lambda_0} \sqrt{\frac{1}{(16d^2/(\pi^2\ell^2) - 1)}} \right) \right]. \tag{5.9}$$

We calculate the derivative of the energy with respect p to find its optimal values. Therefore, we find the roots of the equation $\frac{\partial \epsilon}{\partial p} = 0$ for p. We have that $\frac{\partial \lambda_p}{\partial p} = -\sin p \cos p \lambda_p$, then we have to solve $\frac{\partial \epsilon}{\partial p} = sA[\frac{4\sin p \cos p \lambda_p}{l^2} + \chi \frac{\pi}{d} \cos p] = 0$. The solutions are $\cos p = 0$, i.e. $p_1 = \pi/2$ and $p_2 = -\pi/2$, and $(\frac{4\sin p \lambda_p}{l^2} + \chi \frac{\pi}{d}) = 0$, i.e.

$$p_3 = \chi \arcsin \frac{l}{\lambda_0} \sqrt{\frac{1}{(16d^2/(\pi^2l^2) - 1)}} \tag{5.10}$$

and

$$p_4 = \chi[\pi - \arcsin \frac{l}{\lambda_0} \sqrt{\frac{1}{(16d^2/(\pi^2l^2) - 1)}}] \tag{5.11}$$

where $\lambda_0 = \lambda_{p=0}$. The value of p that minimizes Eq. (5.7) depends on the value of χ and the interfacial Dzyaloshinskii-Moriya parameter.

Figure 5.2 illustrates the total energy Eq 5.7, normalized by $\mu_0 M_s^2 sl$, at zero applied field as a function of the angle p. In absence of DMI, the profile of the energy is symmetric whit respect $p = 0$. We observe that for lower values of D there are two minimum and two maximum values of the energy, while for bigger values of D there are two minimum and one maximum values of the energy. Figure 5.3 illustrates the schematic static vortex domain wall solution when the interfacial Dzyaloshinskii-Moriya interaction is present, and Fig. 5.4 shows the values of p that minimizes the energy as a function of D with $R = 5\ell = 16.25$ nm at different χ [Fig. 5.4(a) for $\chi = +1$ and Fig. 5.4(b) for $\chi = -1$]. We observe that for lower D there are two static solutions related to different chiralities. For $\chi = +1$ the magnetization,
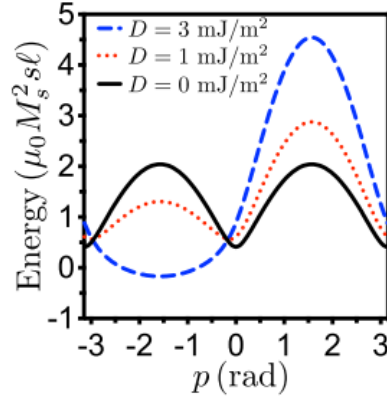
Figure 5.2: Total energy, normalized by $\mu_0 M_s^2 sl$ at zero applied field for a vortex domain wall with $\chi = -1$, as a function of the angle p for $R = 5l$.
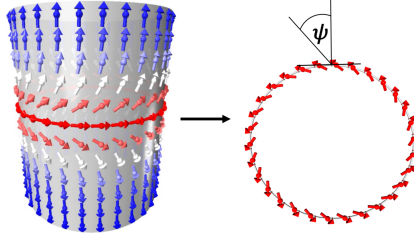

Figure 5.3: Magnetization for $\chi = +1$ and a top view of the magnetization at the domain wall center, when Dzyaloshinskii-Moriya interaction is included. $\psi = \frac{\pi}{2} + p$ is the angle between magnetization and the radial direction.

in the domain wall, has a component that points to the internal radial direction, while for $\chi = -1$ the magnetization has a component that points to the external radial direction. An example of the first case ($\chi = +1$) it is shown in Fig. 5.3. When D increases there is only one static solution for each χ. Then p takes $p = \pi/2$ for $\chi = +1$ (the magnetization is pointing to the internal radial direction $-\hat{\rho}$), and $p = -\pi/2$ for $\chi = -1$ (the magnetization is pointing to the external radial direction $\hat{\rho}$).

To understand the solutions of p, we need to analyze Eqs. (5.8) and (5.9). We observe two conditions from these equations. First, if $\lambda_0 < \ell\sqrt{\frac{1}{(16d^2/(\pi^2\ell^2)-1)}}$, the solutions p_3 and p_4 in Eqs. (5.8) and (5.9) does not exist. Then p takes $p = \pi/2$ for $\chi = +1$, and $p = -\pi/2$ for $\chi = -1$. Therefore, for a fixed β, there is a critical external radius of the tube where there is a transition from one to two solutions of p for a specific D. The second condition is $(16d^2/(\pi^2\ell^2) - 1) > 0$ or $d > \pi\ell/4$ which is equivalent to $D < 2A/(\pi\ell) = 2.55$ mJ/m^2. Therefore, this condition gives an upper bound for D, i.e., if $D > 2A/(\pi\ell)$, there is only one solution for p. This two conditions can be represented in Fig. 5.5. This figure illustrates the critical radius as a function of D. If $R < R_c$, the solution is $p = \pi/2$ ($\chi = +1$) or $p = -\pi/2$ ($\chi = -1$). If $R > R_c$, there are two solutions of p, p_3 and p_4, for every χ. For $D > 2.55$ mJ/m^2, we observe that there is one solution for p. It is because the critical radius goes to infinity at $D = 2.55$ mJ/m^2 (see the vertical line in Fig. 5.5).
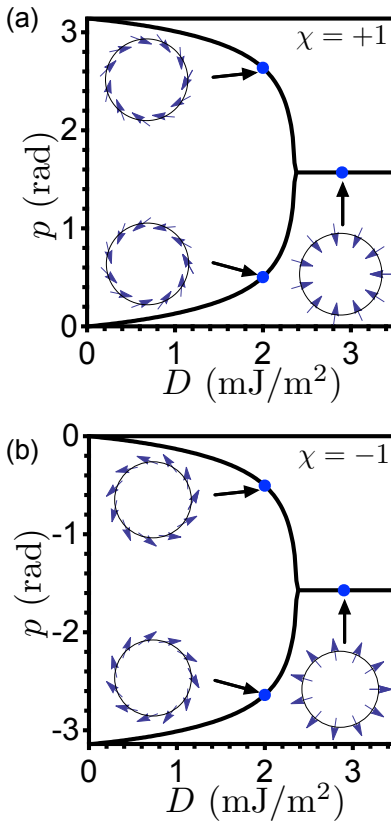
73

Figure 5.4: Value of p for the static solution, for $R = 5\ell$, as a function of D for (a) $\chi = +1$ and (b) $\chi = -1$.
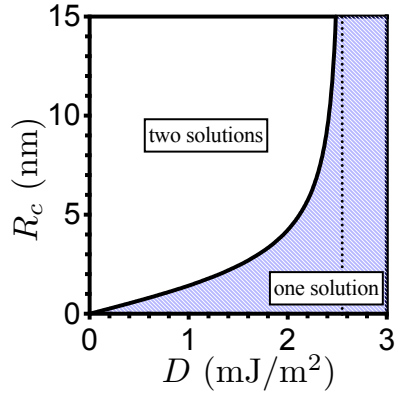

Figure 5.5: Static phase diagram that shows the critical radius as a function of D. For $R < R_c$ there is one static solution, while if $R > R_c$ there are two static solutions.

5.3.2.   Domain wall motion.

In this section, we study the dynamics of the vortex domain wall in these systems. In this case, we consider an external magnetic field applied in the axis of the ferromagnetic nanotube, $\mathbf{H} = H\hat{\mathbf{z}}$, with a Dzyaloshinskii-Moriya parameter different to zero. If we use the same procedure used to obtain the equations of motion for nanotubes without Dzyaloshinskii-Moriya interaction[50, 20, 19], the dynamics equations for our systems are:

$$\alpha\frac{\dot{z}_0}{\lambda_p} + \dot{p} = -\chi\frac{2h}{\tau}, \tag{5.12}$$

$$\frac{\dot{z}_0}{\lambda_p} - \alpha\dot{p} = \frac{\sin(2p)}{\tau} - \chi\frac{\pi\ell^2}{2d\tau}\frac{\cos(p)}{\lambda_p}, \tag{5.13}$$

where $h = H/M_s$, $\tau = 2/(\gamma_0 M_s)$, γ_0 is the gyromagnetic ratio, and α is the damping parameter. It is convenient to write these equation as

$$\frac{\dot{z}_0}{\lambda_p} = -\frac{2\chi\alpha}{\tau(1+\alpha^2)(h - \frac{h^*(p)}{\alpha})}, \tag{5.14}$$

$$\dot{p} = -\frac{2\chi}{\tau(1+\alpha^2)(h - \alpha h^*(p))}, \tag{5.15}$$

where $h^*(p) = \frac{\chi\sin 2p}{2} - \frac{\pi l}{4d}\frac{\cos p}{\lambda_p}$ is an effective field which is proportional to the derivative of the energy $\mathcal{E}$ whit respect p. Figure 5.6 illustrates the average velocity of the domain wall, $v = <\dot{z}_0>$, as a function of the normalized applied field for different values of the Dzyaloshinskii-Moriya parameter, specifically, in Fig. 5.6(a) $D = 0$ mJ/m^2, in Fig. 5.6(b) $D = 0.5$ mJ/m^2, in Fig. 5.6(c) $D = 1$ mJ/m^2, and in Fig. 5.6(d) $D = 3$ mJ/m^2. In these figures we consider $\chi = -1$ and $R = 5\ell$. If $\chi = +1$, we obtain the same magnitudes for the velocity, but the velocity is negative. In the case for $\chi = +1$ the propagation of the domain wall is in the direction $-\hat{z}$ (opposite to the applied field) while for $\chi = -1$ the propagation of the domain wall is in the direction $\hat{z}$ (in the same direction of the applied field).

First, by increasing D, we observe an enhancement of the maximum domain wall average velocity. Also, for $D = 0$, we observe the same curve proposed by Landeros and Núñez for the two initial conditions of p [50]. However, for $D = 0.5$ mJ/m^2 and $D = 1$ mJ/m^2 [see Figs. 5.6(b) and 5.6(c), respectively], we observe two different curves depending on the initial condition of p. For $p = p_3$, we have the same behavior of $D = 0$. But for $p = p_4$, there is a drop of the average velocity at h_{W1}, see Fig. 5.6(b). Similar behavior was observed in the article of Landeros and Núñez when the total energy of the system has the exact demagnetization energy. Finally, when we increase the Dzyaloshinskii-Moriya parameter, see Fig. 5.6(d), there is only one static solution that evolves in the same way than when $D = 0$. In the supplementary material, there are three animations of the domain wall dynamics corresponding to Fig. 5.6(b) for $h = 0.0035$, 0.005, and 0.008.

5.3.3.   Walker critical field and maximum velocity.

To understand well the Fig. 5.6, it is necessary to calculate the Walker fields, h_{W1} and h_{W2}, and the critical domain wall average velocity. The Walker fields, h_{W1} and h_{W2}, are
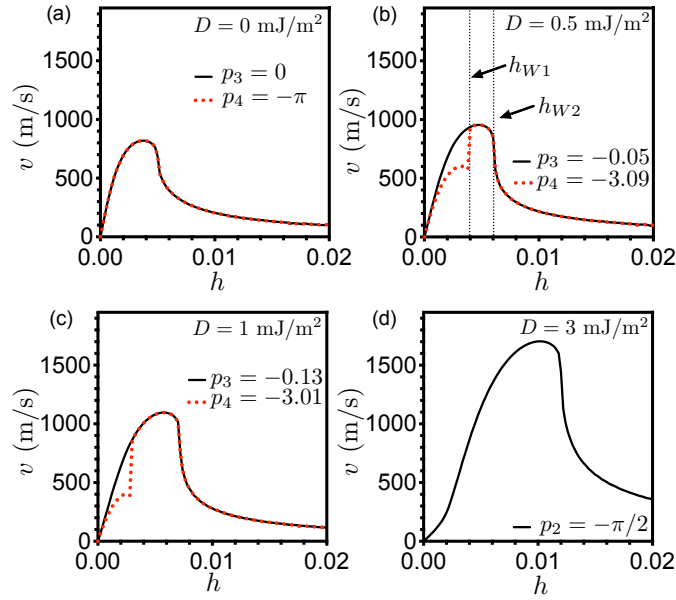
Figure 5.6: Velocity for $\chi = -1$ and $R = 5\ell$ as a function of the applied field for (a) $D = 0$ mJ/m², (b) $D = 0.5$ mJ/m², (c) $D = 1$ mJ/m², and (d) $D = 3$ mJ/m².

obtained through the condition $\dot{p} = 0$ in Eqs. (5.13), i.e.,

$$h = -\alpha h^*(p) = \frac{\alpha}{2}\left[\frac{\pi\ell^2}{2d\lambda_p} - 2\chi\sin(p)\right]\cos(p). \qquad (5.16)$$

Then, we need to obtain the values of p that satisfies this equation for the maximum values of h, i.e., $dh(p)/dp = 0$, and the energy must be minimum for the solutions of p. Figure 5.7 shows the effective field $h^*(p)$ as a function of the angle p for $\chi = -1$. We observe that for $D < 2.55$ mJ/m² there are two maximum (h_{W1} and h_{W2}, with $h_{W1} < h_{W2}$), while for $D > 2.55$ mJ/m² there is one maximum (h_{W2}). For a positive external applied field we observe different behaviors. There are three external applied field regions for $D < 2.55$ mJ/m²: (i) $0 < h < h_{W1}$, (ii) $h_{W1} < h < h_{W2}$, and (iii) $h > h_{W2}$. In the firs region, (i), there are four root of Eq. 5.16 where two of them have the lowest energies and represent the new values of p for each initial condition. These initial conditions are related with two chiralities (counterclock-wise(CCW)) and (clockwise (CW)). The applied field does not deliver enough energy to the system to exceed the energy barriers observerd in Fig. 5.2. Then, the two initial chiralities are preserved and the domain wall motion evolve to a constant velocity and a new equilibrium angle, which are different for each chirality. In the second region, (ii), they are two solution of p, where only one solution has the minimum energy and gives the value of p that evolve from the two initial conditions. Then for $h = h_{W1}$, we observe a drop in the velocity. It is because one of the initial conditions evolve to the another because the applied field delivers enough energy to the system to exceed one of the energy barriers observed in Fig 5.2. Then the system increase its velocity for this chirality with the purpose to minimize its energy. In the last region, (iii), they are not solution for p and we observe an oscillatory solution for this variable. We can conclude that the term associated to the DMI introduces a

chiral asymmetry in the vortex domain wall propagation. Therefore, the domain wall velocity depends on the initial chirality of the system.
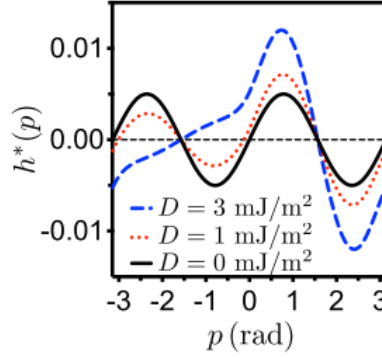

Figure 5.7: Effective field $h^*(p)$ for a vortex domain wall, whit $\chi = -1$, as a function of the angle p for $R = 5l$.
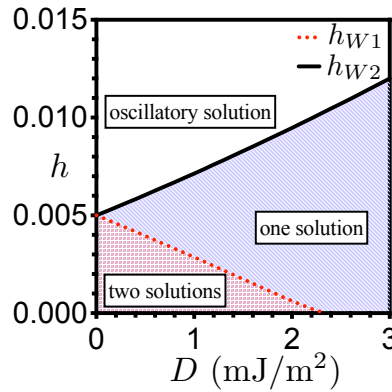

Figure 5.8: Dynamic phase diagram that shows the Walker fields, for $R = 5\ell$, as a function of D. There are different dynamic solutions.

Figure 5.8 illustrates the magnitude of the Walker fields, h_{W1} and h_{W2}, as a function of D for $R = 5\ell$ at fixed β. This figure shows the dynamics phase diagram of the solutions of p. From this figure, we observe that there are three possibilities for the solutions of p if $D < 2A/(\pi\ell) = 2.55$ mJ/m^2 (one dynamics solution, two dynamics solutions , and oscillatory solutions of p) and two possibilities for the solution of p if $D > 2A/(\pi\ell) = 2.55$ mJ/m^2 (one dynamics solution and oscillatory solutions of p). In addition, we observe that both Walker fields have approximately linear behavior at low values of D, where h_{W1} decreases and h_{W2} increases as D increases.

From Fig. 5.6, we observe an enhancement of the critical average velocity and the maximum average velocity of the domain wall when we change the Dzyaloshinskii-Moriya parameter. The critical velocity of the domain wall, v_c, is obtained at the Walker field h_{W2}, i.e.,

$v_c = v(h_{W2})$. From Eq. (5.12), v_c is given by

$$v_c = 2\frac{h_{W2}}{\alpha}\frac{\lambda_{p'}}{\tau}, \tag{5.17}$$

where p' is the dynamics solution of p at $h = h_{W2}$. Additionally, the maximum average velocity of the domain wall, $v_{\max}$, is obtained through the condition $dv/dh = 0$. Figure
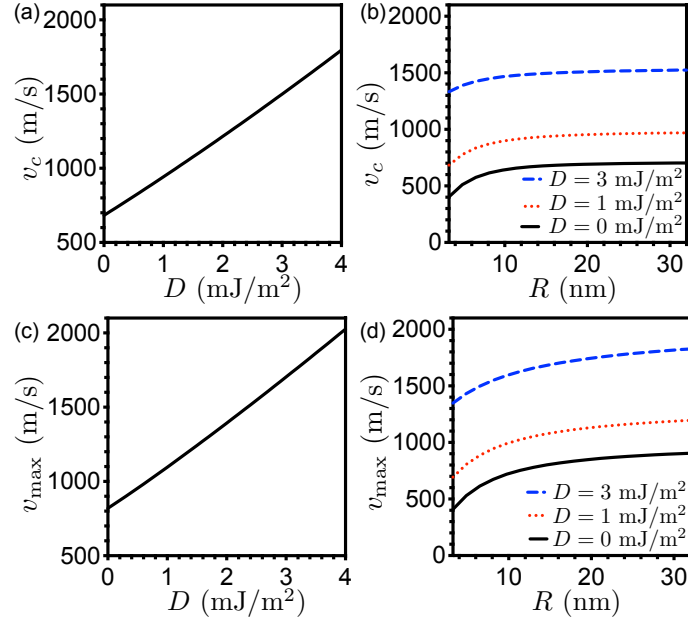

Figure 5.9: (a) Critical velocity as a function of D for $R = 5\ell$ and $\chi = -1$, and (b) critical velocity as a function of R for different values of D.

5.9 illustrates the critical average velocity and the maximum average velocity of the domain wall as a function of D and R. From these figures, we observe that the average velocities increases when we increase D and R. In our system, the maximum average velocity takes the same order observed in ferrimagnetic materials[46], i.e, 10^3 m/s. Due to the fact that DMI introduces a chiral asymmetry in the vortex domain wall propagation, as we can observe in Fig. 5.7, a larger external field is necessary (if we compare with $D = 0$) to reach the Walker breakdown instability. This delay is reflected in an increase of the speed. In other words, our system gives a fast domain wall motion for ferromagnetic materials when the interfacial Dzyaloshinskii-Moriya interaction is present.

5.4. Conclusions.

We studied the domain walls dynamics in thin ferromagnetic nanotubes when the interfacial Dzyaloshinskii-Moriya interaction is present. We observe an ultrafast domain wall average velocity of the order of 10^3 m/s that is similar to the domain wall average velocity for ferrimagnetic nanosystems. Also, we have obtained static and dynamics phase diagrams

for the shape of the domain wall, p value, depending on the Dzyaloshinskii-Moriya parameters. The static phase diagram shows that if $D \geq 2A/(\pi\ell)$, the magnetization of the domain wall points completely along the radial direction. In the other case, if $D < 2A/(\pi\ell)$, the domain wall has two possible chiralities. In the dynamics phase diagram, we observe two Walker fields, h_{W1} and h_{W2}, where the first one corresponds when the average velocity is independent of the chirality in the stationary domain wall motion, and the second one when the domain wall start to have oscillatory motion. The remarkable velocities achieved through this configuration could prove greatly convenient for developing spintronic devices.

Acknowledgements

Chapter 6

Conclusions

Through this thesis, we studied several topics related to bidimensional magnets. The author aimed to connect the spin degrees of freedom of a 2D magnet, with his origin in the electronic picture. Throughout chapters 1, 2, and 3, we take advantage of CrI_3, one of the last discovered bidimensional ferromagnets, and use it as a platform to develop a detailed study of this connection between electrons and magnons.

We started by studying its band structure, in a very simplistic model, which was obtained by professor Eric Suarez, employing ab initio techniques. On this initial model, we neglected any local electronic repulsion, and also the presence of spin-orbit coupling. We observed that with these assumptions, the material behaves as a non-magnetic metal. However, when we included the local electronic repulsion by a multi-orbital Hubbard model, we observed a phase transition to a ferromagnetic semiconductor. The later certainly was a more appropriate model for describing CrI_3, in comparison with that one in which the local electronic repulsion was neglected.

In chapter 2, we used a Green's function method to calculate the functional derivative of the ground state energy with respect to the magnetization field. These functional derivatives were calculated perturbatively, up to second order in the spin-orbit coupling. From this formalism, we obtained the spectrum of the collective low energy excitations. Furthermore, we were able to calculate the energy change, not only in the ground state but in the state having the magnetization polarized in an arbitrary direction. The later allowed us to obtain a full spin Hamiltonian, which describes the low energy regime in CrI_3. We find that between nearest neighbors, the spin-exchange can be approximated by the Heisenberg-Kitaev-Γ model. We also find a non-negligible isotropic exchange between next-nearest neighbors. Finally, we find a contribution of a magneto-crystalline anisotropy, on each Cr site.

In chapter 3, we took a simplified version of the spin model obtained in chapter 2, and we calculated the spectrum analytically. We observed a non-trivial topological structure on the magnonic bands, which could be used to create a topologically protected spin wave's guide in a domain wall.

In part I, we focused on the microscopical description of ferromagnetism in the single-layer CrI_3. In chapters 4 and 5, we studied, another two bidimensional systems, utilizing micro-magnetic simulations. In chapter four, we explored an antiferromagnetic bilayer, with

both layers coupled antiferromagnetically. This AFM coupling between layers allowed us to stabilize an AFM skyrmion on the top layer. We explored this stability for several parameters of the energy functional.

Bidimensional magnets are not only related to plane surfaces, such as layers. That is why in chapter 5, we studied the magnetization at the surface of a nanotube. We focus on the understanding of the equilibrium and dynamics of a domain wall. Moreover, we observed that by including DMI in the energy functional, the domain wall reaches higher velocities, when a magnetic field is applied on the nanotube's axis. Since domain walls are very promising information carriers, this finding has great potential to be used in the design of spintronic devices.

Having all the cards on the table, we hope that this thesis serves as an inspiration for future research. Several questions remain unanswered yet. For example, it would be interesting to study the effect on the spin Hamiltonian of CrI_3, when we apply an electric field perpendicular to the crystal plane. This electric field would break the inversion symmetry on the crystal, and a Dzyaloshinskii–Moriya interaction could emerge from it. Furthermore, if DMI is present in the spin Hamiltonian, it will be possible to stabilize ferromagnetic skyrmions with a fixed radius. Studying the role of Kitaev's coupling in the equilibrium of a skyrmion or any other magnetic textures is also an exciting topic of research. In general, the application of the green's functions formalism, to characterize the anisotropies in the exchange, it is a powerful technique to understand the microscopical origin of anisotropic magnetism in new materials and hetero-structures.

Bibliography

[1] Esteban Aguilera, Rodrigo Jaeschke-Ubiergo, Nicolas Vidal-Silva, Luis Foa, and Alvaro Núñez. Topological magnonics in the two-dimensional van der waals magnet cri3. *arXiv preprint arXiv:2002.05266*, 2020.

[2] Pulickel Ajayan, Philip Kim, and Kaustav Banerjee. van der waals materials. *Physics Today*, 69:9–38, 2016.

[3] Changdeuck Bae, Hyunjung Shin, and Kornelius Nielsch. Surface modification and fabrication of 3d nanostructures by atomic layer deposition. *MRS Bulletin*, 36(11): 887–897, 2011. doi: 10.1557/mrs.2011.264.

[4] V Baltz, A Manchon, M Tsoi, T Moriyama, T Ono, and Y Tserkovnyak. Antiferromagnetic spintronics. *Reviews of Modern Physics*, 90(1):015005, 2018.

[5] A Banerjee, CA Bridges, J-Q Yan, AA Aczel, L Li, MB Stone, GE Granroth, MD Lumsden, Y Yiu, Johannes Knolle, et al. Proximate kitaev quantum spin liquid behaviour in a honeycomb magnet. *Nature materials*, 15(7):733–740, 2016.

[6] Joseph Barker and Oleg A Tretiakov. Static and dynamical properties of antiferromagnetic skyrmions in the presence of applied current and temperature. *Physical review letters*, 116(14):147203, 2016.

[7] A Bocdanov and A Hubert. The properties of isolated magnetic vortices. *physica status solidi (b)*, 186(2):527–543, 1994.

[8] AN Bogdanov and UK Rößler. Chiral symmetry breaking in magnetic thin films and multilayers. *Physical review letters*, 87(3):037203, 2001.

[9] AN Bogdanov, UK Rößler, M Wolf, and K-H Müller. Magnetic structures and reorientation transitions in noncentrosymmetric uniaxial antiferromagnets. *Physical Review B*, 66(21):214410, 2002.

[10] Jörg Bünemann and Florian Gebhard. Coulomb matrix elements in multi-orbital hubbard models. *Journal of Physics: Condensed Matter*, 29(16):165601, 2017.

[11] Krzysztof Byczuk, Martin Ulmke, and Dieter Vollhardt. Ferromagnetism and metal-insulator transition in the disordered hubbard model. *Physical review letters*, 90(19): 196403, 2003.

[12] F Büttner and Lemesh. Theory of isolated magnetic skyrmions: From fundamentals to room temperature applications. *Scientific Reports*, 8(4464), 2018. URL https://doi.org/10.1038/s41598-018-22242-8.

[13] V.L. Carvalho-Santos, R.G. Elias, D. Altbir, and J.M. Fonseca. Stability of skyrmions

on curved surfaces in the presence of a magnetic field. *Journal of Magnetism and Magnetic Materials*, 391:179 – 183, 2015. ISSN 0304-8853. doi: https://doi.org/10.1016/j.jmmm.2015.04.078. URL http://www.sciencedirect.com/science/article/pii/S0304885315300792.

[14] Lebing Chen, Jae-Ho Chung, Bin Gao, Tong Chen, Matthew B Stone, Alexander I Kolesnikov, Qingzhen Huang, and Pengcheng Dai. Topological spin excitations in honeycomb ferromagnet cri 3. *Physical Review X*, 8(4):041028, 2018.

[15] Yuen Tung Chong, Detlef Görlitz, Stephan Martens, Man Yan Eric Yau, Sebastian Allende, Julien Bachmann, and Kornelius Nielsch. Multilayered core/shell nanowires displaying two distinct magnetic switching events. *Advanced Materials*, 22(22):2435–2439, 2010. doi: 10.1002/adma.200904321. URL https://onlinelibrary.wiley.com/doi/abs/10.1002/adma.200904321.

[16] JHP Colpa. Diagonalization of the quadratic boson hamiltonian. *Physica A: Statistical Mechanics and its Applications*, 93(3-4):327–353, 1978.

[17] AT Costa, DLR Santos, NMR Peres, and J Fernández-Rossier. Topological magnons in cri _3 monolayers: an itinerant fermion description. *arXiv preprint arXiv:2002.00077*, 2020.

[18] Sebastian A Diaz and Daniel P Arovas. Quantum nucleation of skyrmions in magnetic films by inhomogeneous fields. *arXiv preprint arXiv:1604.04010*, 2016.

[19] R. A. Duine and H. T. C. Stoof. Stochastic dynamics of a trapped bose-einstein condensate. *Phys. Rev. A*, 65:013603, Dec 2001. doi: 10.1103/PhysRevA.65.013603. URL https://link.aps.org/doi/10.1103/PhysRevA.65.013603.

[20] R. A. Duine, A. S. Núñez, and A. H. MacDonald. Thermally assisted current-driven domain-wall motion. *Phys. Rev. Lett.*, 98:056605, Feb 2007. doi: 10.1103/PhysRevLett.98.056605. URL https://link.aps.org/doi/10.1103/PhysRevLett.98.056605.

[21] Rembert Duine. Spintronics: An alternating alternative. *Nature materials*, 10(5):344, 2011.

[22] Dinh Loc Duong, Seok Joon Yun, and Young Hee Lee. van der waals layered materials: opportunities and challenges. *ACS nano*, 11(12):11803–11830, 2017.

[23] IE Dzialoshinskii. Thermodynamic theory of weak ferromagnetism in antiferromagnetic substances. *SOVIET PHYSICS JETP-USSR*, 5(6):1259–1272, 1957.

[24] Albert Fert, Vincent Cros, and Joao Sampaio. Skyrmions on the track. *Nature nanotechnology*, 8(3):152, 2013.

[25] Raymond Frésard and Gabriel Kotliar. Interplay of mott transition and ferromagnetism in the orbitally degenerate hubbard model. *Physical Review B*, 56(20):12909, 1997.

[26] Yuri Gaididei, Volodymyr P. Kravchuk, and Denis D. Sheka. Curvature effects in thin magnetic shells. *Phys. Rev. Lett.*, 112:257203, Jun 2014. doi: 10.1103/PhysRevLett.112.257203. URL https://link.aps.org/doi/10.1103/PhysRevLett.112.257203.

[27] Börge Göbel, Alexander Mook, Jürgen Henk, and Ingrid Mertig. Antiferromagnetic skyrmion crystals: Generation, topological hall, and topological spin hall effect. *Physical Review B*, 96(6):060406, 2017.

[28] EV Gomonay and VM Loktev. Spintronics of antiferromagnetic systems. *Low Temperature Physics*, 40(1):17–35, 2014.

[29] Helen V Gomonay and Vadim M Loktev. Spin transfer and current-induced switching in antiferromagnets. *Physical Review B*, 81(14):144427, 2010.

[30] Helen V Gomonay, Roman V Kunitsyn, and Vadim M Loktev. Symmetry and the macroscopic dynamics of antiferromagnetic materials in the presence of spin-polarized current. *Physical Review B*, 85(13):134446, 2012.

[31] Arseni Goussev, J. M. Robbins, Valeriy Slastikov, and Oleg A. Tretiakov. Dzyaloshinskii-moriya domain walls in magnetic nanotubes. *Phys. Rev. B*, 93:054418, Feb 2016. doi: 10.1103/PhysRevB.93.054418. URL https://link.aps.org/doi/10.1103/PhysRevB.93.054418.

[32] Kjetil MD Hals, Yaroslav Tserkovnyak, and Arne Brataas. Phenomenology of current-induced dynamics in antiferromagnets. *Physical review letters*, 106(10):107206, 2011.

[33] Jung Hoon Han, Jiadong Zang, Zhihua Yang, Jin-Hong Park, and Naoto Nagaosa. Skyrmion lattice in a two-dimensional chiral magnet. *Physical Review B*, 82(9):094429, 2010.

[34] Paul M Haney and AH MacDonald. Current-induced torques due to compensated antiferromagnets. *Physical review letters*, 100(19):196801, 2008.

[35] Stefan Heinze, Kirsten Von Bergmann, Matthias Menzel, Jens Brede, André Kubetzka, Roland Wiesendanger, Gustav Bihlmayer, and Stefan Blügel. Spontaneous atomic-scale magnetic skyrmion lattice in two dimensions. *Nature Physics*, 7(9):713, 2011.

[36] R Hertel. Ultrafast domain wall dynamics in magnetic nanotubes and nanowires. *Journal of Physics: Condensed Matter*, 28(48):483002, oct 2016. doi: 10.1088/0953-8984/28/48/483002. URL https://doi.org/10.1088%2F0953-8984%2F28%2F48%2F483002.

[37] Riccardo Hertel. Curvature-induced magnetochirality. *SPIN*, 03(03):1340009, 2013. doi: 10.1142/S2010324713400092. URL https://doi.org/10.1142/S2010324713400092.

[38] T Holstein and Hl Primakoff. Field dependence of the intrinsic domain magnetization of a ferromagnet. *Physical Review*, 58(12):1098, 1940.

[39] Bevin Huang, Genevieve Clark, Efrén Navarro-Moratalla, Dahlia R Klein, Ran Cheng, Kyle L Seyler, Ding Zhong, Emma Schmidgall, Michael A McGuire, David H Cobden, et al. Layer-dependent ferromagnetism in a van der waals crystal down to the monolayer limit. *Nature*, 546(7657):270, 2017.

[40] Yangqi Huang, Wang Kang, Xichao Zhang, Yan Zhou, and Weisheng Zhao. Magnetic skyrmion-based synaptic devices. *Nanotechnology*, 28(8):08LT02, 2017.

[41] Rodrigo Jaeschke-Ubiergo and Alvaro S Nunez. Stability of atomic-sized skyrmions in antiferromagnetic bilayers. *Annals of Physics*, 405:29–37, 2019.

[42] Chendong Jin, Chengkun Song, Jianbo Wang, and Qingfang Liu. Dynamics of antiferromagnetic skyrmion driven by the spin hall effect. *Applied Physics Letters*, 109(18):182404, 2016.

[43] Wencan Jin, Hyun Ho Kim, Zhipeng Ye, Siwen Li, Pouyan Rezaie, Fabian Diaz, Saad

Siddiq, Eric Wauer, Bowen Yang, Chenghe Li, et al. Raman fingerprint of two tera-hertz spin wave branches in a two-dimensional honeycomb ising ferromagnet. *Nature communications*, 9(1):1–7, 2018.

[44] Darshan G Joshi. Topological excitations in the ferromagnetic kitaev-heisenberg model. *Physical Review B*, 98(6):060405, 2018.

[45] IV Kashin, VV Mazurenko, MI Katsnelson, and AN Rudenko. Orbitally-resolved ferro-magnetism of monolayer cri3. *2D Materials*, 7(2):025036, 2020.

[46] Kab-Jin Kim, Se Kwon Kim, Yuushou Hirata, Se-Hyeok Oh, Takayuki Tono, Duck-Ho Kim, Takaya Okuno, Woo Seung Ham, Sanghoon Kim, Gyoungchoon Go, Yaroslav Tserkovnyak, Arata Tsukamoto, Takahiro Moriyama, Kyung-Jin Lee, and Teruo Ono. Fast domain wall motion in the vicinity of the angular momentum compensation tem-perature of ferrimagnets. *Nature Materials*, 16:1187 EP –, 09 2017. URL https://doi.org/10.1038/nmat4990.

[47] Se Kwon Kim, Héctor Ochoa, Ricardo Zarzuela, and Yaroslav Tserkovnyak. Realization of the haldane-kane-mele model in a system of localized spins. *Physical review letters*, 117(22):227201, 2016.

[48] Volodymyr P. Kravchuk, Denis D. Sheka, Attila Kákay, Oleksii M. Volkov, Ulrich K. Rößler, Jeroen van den Brink, Denys Makarov, and Yuri Gaididei. Multiplet of skyrmion states on a curvilinear defect: Reconfigurable skyrmion lattices. *Phys. Rev. Lett.*, 120:067201, Feb 2018. doi: 10.1103/PhysRevLett.120.067201. URL https://link.aps.org/doi/10.1103/PhysRevLett.120.067201.

[49] Jose L Lado and Joaquín Fernández-Rossier. On the origin of magnetic anisotropy in two dimensional cri3. *2D Materials*, 4(3):035002, 2017.

[50] P. Landeros and Álvaro S. Núñez. Domain wall motion on magnetic nanotubes. *Journal of Applied Physics*, 108(3):033917, 2010. doi: 10.1063/1.3466747. URL https://doi.org/10.1063/1.3466747.

[51] P. Landeros, S. Allende, J. Escrig, E. Salcedo, D. Altbir, and E. E. Vogel. Reversal modes in magnetic nanotubes. *Applied Physics Letters*, 90(10):102501, 2007. doi: 10.1063/1.2437655. URL https://doi.org/10.1063/1.2437655.

[52] Inhee Lee, Franz G Utermohlen, Daniel Weber, Kyusung Hwang, Chi Zhang, Johan van Tol, Joshua E Goldberger, Nandini Trivedi, and P Chris Hammel. Fundamental spin interactions underlying the magnetic anisotropy in the kitaev ferromagnet cri 3. *Physical Review Letters*, 124(1):017201, 2020.

[53] AO Leonov, TL Monchesky, N Romming, A Kubetzka, AN Bogdanov, and R Wiesen-danger. The properties of isolated chiral skyrmions in thin magnetic films. *New Journal of Physics*, 18(6):065003, 2016.

[54] E. M. Lifshitz and L. P. Pitaevskii. *Statistical Physics*. Pergamon, Oxford, 1980.

[55] Jie Liu, Mengchao Shi, Jiwu Lu, and MP Anantram. Analysis of electrical-field-dependent dzyaloshinskii-moriya interaction and magnetocrystalline anisotropy in a two-dimensional ferromagnetic monolayer. *Physical Review B*, 97(5):054416, 2018.

[56] Jie Liu, Mengchao Shi, Pinghui Mo, and Jiwu Lu. Electrical-field-induced magnetic

skyrmion ground state in a two-dimensional chromium tri-iodide ferromagnetic mono-layer. *AIP Advances*, 8(5):055316, 2018.

[57] Per-Olov Löwdin. On the non-orthogonality problem connected with the use of atomic wave functions in the theory of molecules and crystals. *The Journal of Chemical Physics*, 18(3):365–375, 1950.

[58] Qinlong Luo. Numerical study of hubbard model for iron-based superconductors. 2013.

[59] F Máca, J Mašek, O Stelmakhovych, X Martí, H Reichlová, K Uhlířová, P Beran, P Wadley, V Novák, and T Jungwirth. Room-temperature antiferromagnetism in cumnas. *Journal of Magnetism and Magnetic Materials*, 324(8):1606–1612, 2012.

[60] AH MacDonald and M Tsoi. Antiferromagnetic metal spintronics. *Philosophical Transactions of the Royal Society of London A: Mathematical, Physical and Engineering Sciences*, 369(1948):3098–3114, 2011.

[61] D Mancilla-Almonacid, Rodrigo Jaeschke-Ubiergo, Alvaro S Núñez, and Sebastian Allende. Ultrafast domain wall propagation due to the interfacial dzyaloshinskii–moriya interaction. *Nanotechnology*, 31(12):125707, 2020.

[62] VV Mazurenko and VI Anisimov. Weak ferromagnetism in antiferromagnets: α- fe 2 o 3 and la 2 cu o 4. *Physical Review B*, 71(18):184434, 2005.

[63] Michael A McGuire, Hemant Dixit, Valentino R Cooper, and Brian C Sales. Coupling of crystal structure and magnetism in the layered, ferromagnetic insulator cri3. *Chemistry of Materials*, 27(2):612–620, 2015.

[64] Alan D McNaught, Andrew Wilkinson, et al. *Compendium of chemical terminology*, volume 1669. Blackwell Science Oxford, 1997.

[65] N David Mermin and Herbert Wagner. Absence of ferromagnetism or antiferromagnetism in one-or two-dimensional isotropic heisenberg models. *Physical Review Letters*, 17(22):1133, 1966.

[66] Tôru Moriya. Anisotropic superexchange interaction and weak ferromagnetism. *Physical Review*, 120(1):91, 1960.

[67] Arash A Mostofi, Jonathan R Yates, Giovanni Pizzi, Young-Su Lee, Ivo Souza, David Vanderbilt, and Nicola Marzari. An updated version of wannier90: A tool for obtaining maximally-localised wannier functions. *Computer Physics Communications*, 185(8): 2309–2310, 2014.

[68] Naoto Nagaosa and Yoshinori Tokura. Topological properties and dynamics of magnetic skyrmions. *Nature nanotechnology*, 8(12):899, 2013.

[69] Ashis Kumar Nandy, Nikolai S Kiselev, and Stefan Blügel. Interlayer exchange coupling: a general scheme turning chiral magnets into magnetic multilayers carrying atomic-scale skyrmions. *Physical review letters*, 116(17):177202, 2016.

[70] Kostya S Novoselov, Andre K Geim, Sergei V Morozov, DA Jiang, Y_ Zhang, Sergey V Dubonos, Irina V Grigorieva, and Alexandr A Firsov. Electric field effect in atomically thin carbon films. *science*, 306(5696):666–669, 2004.

[71] KS Novoselov, A Mishchenko, A Carvalho, and AH Castro Neto. 2d materials and van

der waals heterostructures. *Science*, 353(6298):aac9439, 2016.

[72] J.A. Otálora, J.A. López-López, P. Landeros, P. Vargas, and A.S. Nunez. Breaking of chiral symmetry in vortex domain wall propagation in ferromagnetic nanotubes. *Journal of Magnetism and Magnetic Materials*, 341:86 – 92, 2013. ISSN 0304-8853. doi: https://doi.org/10.1016/j.jmmm.2013.04.014. URL http://www.sciencedirect.com/science/article/pii/S0304885313002333.

[73] Jorge A. Otálora, Ming Yan, Helmut Schultheiss, Riccardo Hertel, and Attila Kákay. Curvature-induced asymmetric spin-wave dispersion. *Phys. Rev. Lett.*, 117:227203, Nov 2016. doi: 10.1103/PhysRevLett.117.227203. URL https://link.aps.org/doi/10.1103/PhysRevLett.117.227203.

[74] SA Owerre. A first theoretical realization of honeycomb topological magnon insulator. *Journal of Physics: Condensed Matter*, 28(38):386001, 2016.

[75] Je-Geun Park. Opportunities and challenges of two-dimensional magnetic van der waals materials: magnetic graphene? *arXiv preprint arXiv:1604.08833*, 2016.

[76] Pablo Pizarro. Template informe en LaTeX, 2016-2020. URL https://latex.ppizarror.com/informe.

[77] I Raičević, Dragana Popović, C Panagopoulos, L Benfatto, MB Silva Neto, ES Choi, and T Sasagawa. Skyrmions in a doped antiferromagnet. *Physical review letters*, 106 (22):227206, 2011.

[78] Ulrich K Rößler, Andrei A Leonov, and Alexei N Bogdanov. Chiral skyrmionic matter in non-centrosymmetric magnets. In *Journal of Physics: Conference Series*, volume 303, page 012105. IOP Publishing, 2011.

[79] Denis D Sheka, Volodymyr P Kravchuk, and Yuri Gaididei. Curvature effects in statics and dynamics of low dimensional magnets. *Journal of Physics A: Mathematical and Theoretical*, 48(12):125202, mar 2015. doi: 10.1088/1751-8113/48/12/125202. URL https://doi.org/10.1088%2F1751-8113%2F48%2F12%2F125202.

[80] Ryuichi Shindou, Ryo Matsumoto, Shuichi Murakami, and Jun-ichiro Ohe. Topological chiral magnonic edge mode in a magnonic crystal. *Physical Review B*, 87(17):174427, 2013.

[81] A Siemens, Y Zhang, J Hagemeister, E Y Vedmedenko, and R Wiesendanger. Minimal radius of magnetic skyrmions: statics and dynamics. *New Journal of Physics*, 18(4):045021, 2016. URL http://stacks.iop.org/1367-2630/18/i=4/a=045021.

[82] Michael Springford. *Electrons at the Fermi surface*. Cambridge University Press, 2011.

[83] Joachim Stöhr and Hans Christoph Siegmann. *Magnetism: from fundamentals to nanoscale dynamics*, volume 152. Springer Science & Business Media, 2007.

[84] Robert Streubel, Peter Fischer, Florian Kronast, Volodymyr P Kravchuk, Denis D Sheka, Yuri Gaididei, Oliver G Schmidt, and Denys Makarov. Magnetism in curved geometries. *Journal of Physics D: Applied Physics*, 49(36):363001, aug 2016. doi: 10.1088/0022-3727/49/36/363001. URL https://doi.org/10.1088%2F0022-3727%2F49%2F36%2F363001.

[85] Hidenori Takagi, Tomohiro Takayama, George Jackeli, Giniyat Khaliullin, and

Stephen E Nagler. Kitaev quantum spin liquid-concept and materialization. *arXiv preprint arXiv:1903.08081*, 2019.

[86] André Thiaville, Stanislas Rohart, Émilie Jué, Vincent Cros, and Albert Fert. Dynamics of dzyaloshinskii domain walls in ultrathin magnetic films. *EPL (Europhysics Letters)*, 100(5):57002, dec 2012. doi: 10.1209/0295-5075/100/57002. URL https://doi.org/10.1209%2F0295-5075%2F100%2F57002.

[87] Y Tokura, Y Taguchi, Y Okada, Y Fujishima, T Arima, K Kumagai, and Y Iye. Filling dependence of electronic properties on the verge of metal–mott-insulator transition in sr 1- x la x tio 3. *Physical review letters*, 70(14):2126, 1993.

[88] R. Tomasello, K.Y. Guslienko, M. Ricci, A. Giordano, J. Barker, M. Carpentieri, O. Chubykalo-Fesenko, and G. Finocchio. Origin of temperature and field dependence of magnetic skyrmion size in ultrathin nanodots. *PRB*, 97(6), 2018. doi: 10.1103/PhysRevB.97.060402. URL https://doi.org/10.1038/s41598-018-22242-8.

[89] Sergei Urazhdin and Nicholas Anthony. Effect of polarized current on the magnetic state of an antiferromagnet. *Physical review letters*, 99(4):046602, 2007.

[90] Z Wei, A Sharma, AS Nunez, PM Haney, RA Duine, J Bass, AH MacDonald, and M Tsoi. Changing exchange bias in spin valves with an electric current. *Physical review letters*, 98(11):116603, 2007.

[91] Sönke Wienholdt, Denise Hinzke, and Ulrich Nowak. Thz switching of antiferromagnets and ferrimagnets. *Physical review letters*, 108(24):247207, 2012.

[92] Changsong Xu, Junsheng Feng, Hongjun Xiang, and Laurent Bellaiche. Interplay between kitaev interaction and single ion anisotropy in ferromagnetic cri 3 and crgete 3 monolayers. *npj Computational Materials*, 4(1):1–6, 2018.

[93] Ming Yan, Attila Kákay, Sebastian Gliga, and Riccardo Hertel. Beating the walker limit with massless domain walls in cylindrical nanowires. *Phys. Rev. Lett.*, 104:057201, Feb 2010. doi: 10.1103/PhysRevLett.104.057201. URL https://link.aps.org/doi/10.1103/PhysRevLett.104.057201.

[94] XZ Yu, Yoshinori Onose, Naoya Kanazawa, JH Park, JH Han, Yoshio Matsui, Naoto Nagaosa, and Yoshinori Tokura. Real-space observation of a two-dimensional skyrmion crystal. *Nature*, 465(7300):901, 2010.

[95] Jiadong Zang, Maxim Mostovoy, Jung Hoon Han, and Naoto Nagaosa. Dynamics of skyrmion crystals in metallic thin films. *Physical review letters*, 107(13):136804, 2011.

[96] X. Zhang, Y. Zhou, and M. Ezawa. Antiferromagnetic Skyrmion: Stability, Creation and Manipulation. *Scientific Reports*, 6:24795, April 2016. doi: 10.1038/srep24795.

[97] Xichao Zhang, Motohiko Ezawa, and Yan Zhou. Magnetic skyrmion logic gates: conversion, duplication and merging of skyrmions. *Scientific reports*, 5:9400, 2015.